12-10-2021

Kinematics of Inter-Ply Interfaces In Composite Manufacturing

Sandeep Chava
Embry-Riddle Aeronautical University, sandeepchava@gmail.com

KINEMATICS OF INTER-PLY INTERFACES IN COMPOSITE MANUFACTURING

By

Sandeep Chava

A Dissertation Submitted to the Faculty of Embry-Riddle Aeronautical University

In Partial Fulfillment of the Requirements for the Degree of

Doctor of Philosophy in Aerospace Engineering

December 2021

Embry-Riddle Aeronautical University

Daytona Beach, Florida

KINEMATICS OF INTER-PLY INTERFACES IN COMPOSITE MANUFACTURING

By

Sandeep Chava

This Dissertation was prepared under the direction of the candidate's Dissertation Committee Chair, Dr. Sirish Namilae, Department of Aerospace Engineering, and has been approved by the members of the Dissertation Committee. It was submitted to the Office of the Senior Vice President for Academic Affairs and Provost, and was accepted in the partial fulfillment of the requirements for the Degree of Philosophy in Aerospace Engineering.

DISSERTATION COMMITTEE

Sirish Namilae — Digitally signed by Sirish Namilae Date: 2021.12.09 08:55:36 -05'00'

Chairman, Dr. Sirish Namilae

Marwan Al-Haik — Digitally signed by Marwan Al-Haik Date: 2021.12.09 12:57:07 -05'00'

Member, Dr. Marwan Al-Haik

Daewon Kim — Digitally signed by Daewon Kim Date: 2021.12.09 09:42:01 -05'00'

Member, Dr. Daewon Kim

Alberto W Mello — Digitally signed by Alberto W Mello Date: 2021.12.09 10:36:21 -05'00'

Member, Dr. Alberto Mello

Eduardo A. Rojas — Digitally signed by Eduardo A. Rojas Date: 2021.12.10 10:09:26 -05'00'

Member, Dr. Eduardo Rojas

Sirish Namilae — Digitally signed by Sirish Namilae Date: 2021.12.10 10:11:56 -05'00'

Graduate Program Coordinator,
Dr. Sirish Namilae

Date

James W. Gregory — Digitally signed by James W. Gregory Date: 2021.12.10 14:35:08 -05'00'

Dean of the College of Engineering,
Dr. James Gregory

Date

Senior Vice President for Academic Affairs and Provost,
Dr. Lon Moeller

12-10-21

Date

DEDICATION

This dissertation is dedicated to my father,

Venkatrao Chava

May his memory forever be a
comfort and a blessing
He was the best father
a kid could have

ACKNOWLEDGMENTS

It gives me immense pleasure to acknowledge all the people that supported me and stood beside me in this amazing journey. First and foremost, I am extremely grateful to my committee chair, Dr. Sirish Namilae for his invaluable advice, continuous support, and patience during my Ph.D. study. His immense knowledge and plentiful experience have encouraged me in all the time of my academic research and daily life. He consistently allowed this research to be my work but steered me and motivated me in the right direction. His insightful feedback pushed me to sharpen my thinking and brought my work to a higher level. I could not have imagined having a better advisor and mentor for my Ph.D. study and I am extremely grateful that he took me on as a student and continued to have faith in me over the years.

I would like to thank my committee members Dr. Marwan Al-Haik, Dr. Daewon Kim, Dr. Alberto Mello, and Dr. Eduardo Rojas for their insightful comments and encouragement, but also for the hard question which incented me to widen my research from various perspectives.

I would like to thank Dr. Habib Eslami and Dr. David J Sypeck for sharing their knowledge and mentorship. I would like to thank my friends, lab mates, colleagues, and research team Samarth, Yuxuan, Audrey, Rossana, Suma, Rishi, Boutros, Stanislav, Sai, Amrutha, and Bhanu for a cherished time spent together in the lab, and in social settings. My appreciation also goes out to my family for their encouragement and support in seeing me through the toughest time of my life. I love them so much, and I would not have made it this far without them. Finally, I would like to thank the Aerospace Engineering department for continuous support throughout all these years.

ABSTRACT

The ubiquitous usage of polymer matrix composites in many applications demands a comprehensive understanding of composite interfaces and processing induced residual stresses, which critically affect both the manufacturing processes and the deformation mechanisms. Processing induced residual stresses are often responsible for causing warping, delamination, and dimensional instability in composite structures. This research includes new in-situ experimental approaches, cure cycle design, interface modification, and thermomechanical modeling for developing a fundamental understanding of the cure kinetics during composite manufacturing. Strains, ply-movement, and formation of defects are observed in-situ using digital image correlation (DIC) during the autoclave cure cycle for the first time. The processing-induced defects in the composite are further characterized by X-ray micro-computed tomography (micro-CT). A non-destructive method is developed to calculate residual stresses using DIC Strains in combination with temperature-dependent moduli obtained from Dynamic Mechanical Analysis (DMA) and Classical Laminate Theory (CLT). Cure cycle design with interrupted cure and interface modification with ZnO nanorods experiments are developed to reduce these processing-induced residual stresses and thereby increase laminate strength. The experimental results are validated through thermomechanical modeling of the composite cure process.

TABLE OF CONTENTS

LIST OF FIGURES

Figure Page

Figure Page

Figure Page

LIST OF TABLES

NOMENCLATURE

CPC	Composite Processing Control
NDT	Non-Destructive Testing
Micro-CT	Micro Computed Tomography
CRM	Cure Referencing Method
PIV	Particle Image Velocimetry
DIC	Digital Image Correlation
CTE	Coefficient of Thermal Expansion
CLT	Classical Lamination Theory
PBF	Powder Bed Fusion
SLM	Selective Laser Melting
XRD	X-Ray Diffraction
FEA	Finite Element Analysis
DMA	Dynamic Mechanical Analysis
TMA	Thermomechanical Analysis
BMI	Bismaleimide
DCB	Double Cantilever Beam
DSC	Differential Scanning Calorimetry
DOC	Degree of Cure
MRCC	Manufacturer Recommended Cure Cycle
FBG	Fiber Bragg Grating
FE	Finite Element
IBVP	Initial Boundary Value Problem

CNFs	Carbon Nanofibers
HTC	Heat Transfer Coefficient
CFD	Computational Fluid Dynamics
BCs	Boundary Conditions
ACP	Ansys Composite PrePost
ASTM	American Society for Testing and Materials
APDL	Ansys Parametric Design Language
ACCS	Ansys Composite Cure Simulations
LHS	Latin Hypercube Sampling
ZnO	Zinc Oxide
FA	Fracture Analysis
DI	Deionized
JMA	Johnson-Mehl-Avrami
SB	Sestak-Berggren
IC	Interrupted Cure

1. Introduction

In this first chapter, the main components of this dissertation including aerospace composites, interfaces, and processing defects are introduced. The motivation for this work is discussed. The objectives of this research and the various steps taken to achieve these objectives are introduced.

1.1. Motivation

Composite materials have been widely used for structural applications in aerospace (Irving & Soutis, 2019), automobiles (Fuchs et al., 2008), and other applications (Gay, 2014). Light weight, high specific strength, resistance to corrosion and flexibility in design, etc. are some of the properties displayed by these materials that have benefited many industries, more specifically aerospace. For example, commercial aircraft such as Boeing 787 and Airbus 380 are two of the first commercial aircraft to feature composites in the fuselage and other primary structures. The pervasive usage of these polymer matrix composites necessitates a comprehensive understanding of composite interfaces which critically affect both the manufacturing processes and the deformation mechanisms in composites.

Interfaces are two-dimensional transition regions in materials and are typically associated with higher entropy (Sutton, 1995). Because of this higher energy state, interfaces not only exhibit increased chemical activity (Sanchez, 2013; Sutton, 1995) but also play a key role in the limiting deformation processes (e.g., fracture) (Greszczuk, 1969; Hsueh, 1990; Plueddemann, 2016). This is especially true in composites where two dissimilar materials interact, for example, load transfer to fibers and hence the mechanical behavior of composites is essentially defined by the well-studied fiber-matrix

interface (Chandra et al., 2002; Greszczuk, 1969; Hsueh, 1990; Plueddemann, 2016). A relatively less studied aspect of the composite interfacial behavior is that of the evolution and kinematics of the inter-ply interfaces during the manufacturing of aerospace composites. Effective chemical bonding at these interfaces during fabrication would result in a defect-free structure and the directional properties of these ply interfaces during processing leads to the development of residual stresses.

Residual stresses which arise during composite manufacturing are self-balanced stresses that exist in the absence of external loads. They typically reduce the mechanical properties of the composite and lead to defects like warpage. Processing induced residual stresses are caused because of the directional properties of plies (Cheng & Finnie, 2007), polymerization shrinkage of the matrix during curing, and due to the dissimilar thermomechanical response of matrix and fibers during thermal cycling (Witik et al., 2011). The magnitude of residual stresses is an important consideration in designing load-bearing structures as they can cause processing defects such as warping (Nanni, 1993), undesired distortion (Sutton, 1995), and dimensional instability (Sanchez, 2013). They can prestress the structure and affect the overall strength by causing microcracks in the matrix (Plueddemann, 2016), which can lead to further environmental degradation.

In this context, it is essential to understand the evolution and kinematics of the interfaces between plies and necessary to factor in the residual stresses in the processing of composite structures, both of which are primary drivers for creating processing defects. Consider a common processing defect, wrinkles as an example; wrinkles are studied in various fields such as skin wrinkles (Tallinen et al., 2010), thin films (Prodromou & Chen, 1997), sheet metal forming (B. Zhu et al., 2007), and fabrics

(Pandey & Sun, 1999), consequently theoretical developments such as scaling behavior (Fish et al., 1999), kinematic and geometric modeling (Dodwell et al., 2014), shear locking behavior (Erland et al., 2014), etc. can be applied to composite wrinkles. Inter-ply shear deformation and restricted motion of plies during processing are responsible for composite wrinkles, while inter-ply interface displacement in the normal direction causes delamination. The formation of both defects, as well as other processing-induced defects, are primarily defined by the residual stresses developed and the inter-ply slip behavior in response to the processing conditions. Therefore, it is necessary to evaluate the residual stresses and the ply slippage in processing conditions.

1.2. Objectives of This Dissertation

The current state-of-the-art on composites processing is reviewed in the next chapter with a focus on ply movement and residual stresses developed during the processing. While this area is well researched, many questions on the fundamental aspects of the evolution of residual stresses from the stress-free point till the end of the cure remain unanswered. Particularly, the correlation between the processing induced residual stresses and defects at every stage during the cure, along with the potential methods to effectively reduce the residual stresses, need to be explored further. This research attempts to fill the gaps in the current understanding in these areas.

The primary objectives of this dissertation are to:

1. **Develop experimental and analytical methods for continuous in-situ evaluation of processing induced residual stresses.** We develop a novel in-situ experimental approach in Chapter 3 to measure the dimensional changes in the laminates during cure and combined with temperature-dependent moduli obtained

from Dynamic Mechanical Analysis (DMA) to calculate the continuous evolution of residual stresses during composite processing. Five symmetric and asymmetric layup configurations are analyzed to investigate the effect of ply orientation on the residual stress evolution.

2. **Develop approaches for residual stress reduction during manufacturing through cure modification.** The novel in-situ experimental approach using digital image correlation (DIC) developed in Chapter 3 is utilized in Chapter 4 to analyze the effect of the cure cycle modification on residual stress evolution during processing. It was found that the modified cure cycle comprising abrupt cooling after gelation reduces the residual stresses. Two symmetric and three asymmetric layup configurations are investigated to examine the effect of fiber orientation. Another approach for residual stress reduction based on **interface modification** using ZnO nanorods is briefly explored.
3. **Study the kinematics of ply interfaces during composite manufacturing.** In Chapter 5, Carbon fiber prepreg laminates are cured with plies laid up on a mold with a cylindrical tooling setup to maximize the ply movement. Four-ply layup orientations of $[90/90]_s$, $[90/0]_s$, $[90/45]_s$ and $[90/-45]_s$ and three mold configurations with cylindrical tools of diameter 9.5 mm (3/8 inch), 12.7 mm (1/2 inch) and 15.9 mm (5/8 inch) are used for the parametric study. The processing induced defects in the composite are further characterized by X-ray micro-computed tomography (micro-CT). It is observed that the mold with a larger radius of curvature (15.9 mm cylinder) leads to higher strains in both in-plane directions and higher displacement in out-of-plane directions.

4. **Computational modeling for the fundamental understanding of the curing process.** In Chapter 6, to better understand the effect of cure parameters on the cure-induced stresses and defects, the experimental results are correlated with the cure simulations. Ansys Composite Cure Simulations (ACCS) tool in ANSYS was used to perform the cure simulation tasks, supported by thermal analysis using Differential Scanning Calorimeter (DSC).

2. Scientific Background and Relevant Literature

In this chapter, the current literature on aspects of composite materials related to this research is surveyed. Topics including different composite manufacturing processes, residual stress development during cure, and manufacturing defects are reviewed. Various methods used to measure residual stresses and methods adopted to reduce processing induced residual stresses are discussed in detail.

2.1. Aerospace Composites

The constant drive in the aerospace industry to reduce weight and improve the performance of an aircraft has propelled the development of innovative high-performance structural materials. Composite materials are one such class of materials that play a vital role in aerospace structures. Composite materials are particularly attractive to the aerospace industry due to their several advantages over metals such as exceptional strength and stiffness-to-density ratios, durability, corrosion resistance, lightweight, and fatigue resistance (Irving & Soutis, 2019).

Two of the most recognized composites in aerospace are carbon fiber reinforced plastic (CFRP) and glass fiber reinforced plastic (GFRP) are used in many structural components in aircraft wings, fuselage, and empennage. Composites like carbon-carbon are used in manufacturing re-entry nose tips and heat shields of a space vehicle (Windhorst & Blount, 1997). The ability to tailor the laminate pattern to give the required mechanical properties in various directions in a structure is one of the key advantages of composites (Ballinger, 1990). This also decreases the part count in a structure there by reducing the production costs. It is also easier to produce complex double-curvature parts with a smooth surface finish that reduces drag using composites.

While many advantages are apparent in the use of composites in aerospace applications, there are a few disadvantages that should be considered. The initial cost of production which often involves developing new processing methods is higher for composites than metals (Chung, 2012). The damage tolerance of composites is lower than the metals as they are more brittle than wrought metals and repairing damage requires special techniques and tooling. Another disadvantage is that, unlike metals, the long-term fatigue characteristics of composites are unknown as the relative age of composites is much lower than metals (Reifsnider et al., 1983). Despite these disadvantages, the use of composites is steadily increasing as several innovative methods in manufacturing composites are being developed to lower the production costs, and the development of new fibers (e.g. hybrid fibers) and matrix materials is increasing the damage tolerance of the composites.

2.2. Manufacturing of Aerospace Composites

Composite structures are fabricated using several molding methods in the industry which are divided into three basic categories depending on the material, design, and the application of the part. They are open molding (Nunez et al., 1999), closed molding (Chan et al., 2002), and cast polymer molding (Blagojevic et al., 2020). Out of these three molding methods, vacuum bagging, which is one of the closed molding methods, is the primary method used in the industry to manufacture composite structures (Abdurohman et al., 2018).

In the vacuum bagging method of processing, a vacuum bag is placed over a wet hand layup of the composite laminate, sealed with sealant tape, and the vacuum is drawn. The components inside the vacuum bag are; a release film over the laminate, a bleeder ply to

absorb the excel resin forced out by the vacuum, a breather ply over the bleeder, and plastic film encasing the entire laminate area acting as a vacuum bag. The vacuum applied in this method forces out entrapped air and excess resin, compacting the laminate thus providing better interply adhesion without voids (Boey & Lye, 1992). The vacuum-bagged composite structure is typically cured in an autoclave under the action of high temperature and pressure.

2.2.1. Autoclave Processing of Composite Materials

Figure 2.1 Autoclave equipped with composite processing control (CPC) (ASC Process Systems).

The autoclave and vacuum bagging process are commonly used to produce high-performance structural laminates (Hubert et al., 2012). In this process, the layers of prepreg are cut and stacked to form the desired structure by vacuum bagging on a tooling surface. The bagged structure is then placed in an autoclave, which is a large vessel with the ability to precisely control the temperature and pressure inside it. The autoclave is also equipped with a vacuum system for vacuum bagging. For the structure to be cured,

predefined temperature and pressure are applied to it in the form of a cure cycle. Autoclaves are available in a wide range of sizes based on the usage starting from a working diameter X working length of 0.305 m X 0.609 m up to 5.486 m X 18.288 m. Figure 2.1 shows an autoclave procured from ASC with computer processing control to control the cure parameters of the cure cycle.

Composite processing in autoclaves happens through a combination of pressure, vacuum, and temperature variation with respect to time (J. S. Kim & Lee, 1997). The temperature cycle is required to trigger the crosslinking of the resin and is divided into three phases. The initial ramp-up phase is when the temperature is increased from room temperature to cure temperature. This is followed by the hold-phase in which the cure temperature is maintained for the cure time recommended by the manufacturer. After the cure is complete, the final phase is the cool-down phase where the composite structure is cooled from cure temperature to room temperature. This completes the temperature cycle.

During cure, pressure and vacuum are continuously applied to the structure (Boey & Lye, 1990). The pressure helps to conform the prepreg to the mold surface and to compact the laminate at the desired fiber volume fraction and remove any voids that may develop during cure. The vacuum helps in removing any entrapped air and excess resin from the layup. The vacuum-bagged pressure is always less than the autoclave pressure for the compaction of the composite structure. Finally, after the cure cycle is complete, the structure is debagged and ready for the further finishing process.

Epoxy is the common resin used in aerospace composites. The B-stage epoxy resin present in the prepreg is partially cured to hold the fibers together (Roller, 1975). As the layup is heated during cure, the resin starts flowing through the interfaces of the plies for

compaction. In general, epoxies are a mixture of two parts: resin and hardener. The epoxy resin molecules are characterized by the presence of one or more epoxy groups per molecule containing one oxygen atom and two hydrogen atoms (Pham & Marks, 2000). This three-membered ring makes epoxy resins highly reactive, and the polymerization happens with the help of a cross-linking/curing agent reacting with the epoxide groups. After polymerization, the viscous resin becomes rigid polymer by this process of curing. The percentage of polymerization varies with various factors like the ratio of resin and curing agent, the temperature of cure (Peyser & Bascom, 1977).

2.3. Processing Induced Defects in Composites

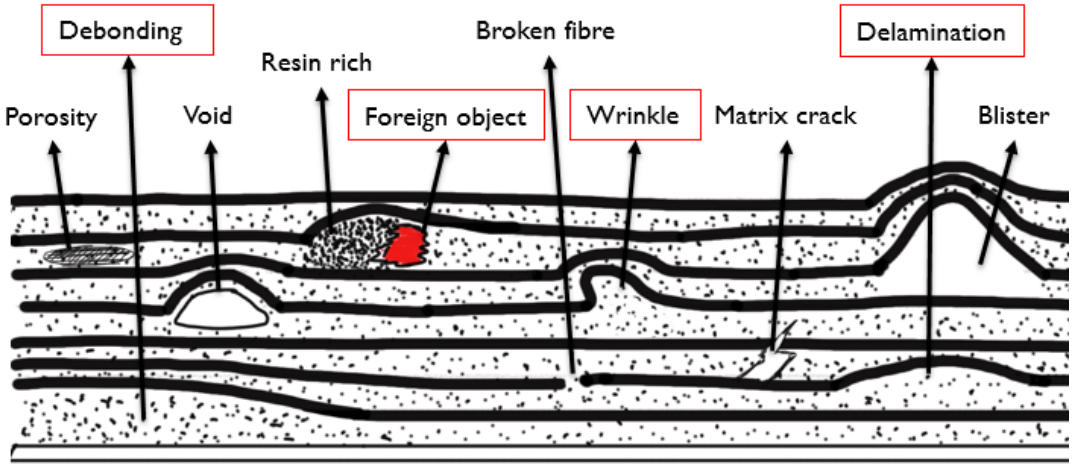

Figure 2.2 Schematic showing several defects in composites.

Prepreg composites are being increasingly used not only for aerospace, civil (Pendhari et al., 2008), and automobile applications (Rezaei et al., 2008) but also in everyday consumer products (Gay, 2014). Prepregs reduce the risk of poor impregnation in manufacturing and are often cured under high temperature and pressure conditions in an autoclave (Toldy et al., 2011). Processing induced defects such as porosity, debonding, voids, broken fibers, wrinkling, and delamination are created during the

manufacturing of prepreg composite structures (R. Smith, 2009). Among these defects, wrinkling and delamination, which are associated with the interfacial inter-ply movement are frequently encountered in large composite structures and parts with curvature (Park et al., 2014; J. Zhu et al., 2016). Processing-induced delamination and wrinkling are closely related. Inter-ply shear deformation and restricted motion are responsible for wrinkles, while inter-ply interface displacement in the normal direction causes delamination. The formation of both defects, as well as other processing-induced defects often depend on the inter-ply adhesion and slip behavior in response to the processing conditions.

Wrinkles and delamination are of particular importance due to their impact on the strength and the stiffness of the composite structures (Takeda, 2018). Ipek et al. (2018) investigated the effect of delamination size and location on composite mechanical properties. They found that delamination in the interior of an eight-ply woven glass fiber composite plate decreases the critical buckling load by up to 48%. Elhajjar and Shams (2014) observed a 30% reduction in compressive strength due to wrinkles with angles between 20^{o} to 30^{o}. Recently, Zhu et al. (2018) provided an analytical model to evaluate the reduction in stiffness of composite laminates with wrinkles using classical laminate theory. On the other hand, manufacturing companies like Boeing and Airbus have suffered substantial economic impacts due to these processing-induced defects in the manufacturing of airplane parts in the past (Heslehurst, 2014; Petrescu et al., 2017). These defects are not limited only to these companies but many other manufacturing companies. Due to their negative impact, identifying and reducing the occurrence of these defects is crucial.

2.3.1. Monitoring of Processing Induced Defects

Several researchers focused on methods to predict and analyze the formation of processing-induced defects. Nondestructive testing (NDT) methods like eddy current testing were used by Mizukami et al. (2016) in detecting in-plane and out-of-plane fiber waviness in unidirectional composites. Their approach can detect fiber waviness with an amplitude of 1.1 mm and a length of 15.9 mm. X-ray computed tomography (CT) was used by Sutcliffe et al. to measure fiber waviness (Sutcliffe et al., 2012). Smith et al. used ultrasonic techniques to track out-of-plane ply angles and ply drops in composite laminates (R. A. Smith et al., 2016). Nikishkov et al. (2013) developed a method for generating finite element meshes for unidirectional composites with waviness defects using images from X-ray Micro-CT. They interpolated the fiber slope data from volume slice images using radial basis functions to create mesh nodes. Freemantle et al. used ultrasonic NDT data to develop finite element models of flat panel composites containing impact-induced delaminations (Freemantle et al., 2014). Most of these studies are not associated with autoclave processing and are applied to the composite structure post-manufacturing and during testing.

The formation of processing induced defects is often associated with the movement of plies during cure. The inter-ply behavior during cure depends on: firstly, the evolution of chemical crosslinking between partially cured polymer layers at the ply interface and secondly, the interfacial response to the thermomechanical loads during processing at high temperatures and pressures. Researchers in the past used various contactless optical techniques to capture strains and deformations associated with composite curing and thermomechanical loads. Speriatu et al. (2005) used Moiré photography in conjunction with the Cure Referencing Method (CRM) to measure surface strains in the composites.

Their method uses high-frequency diffraction gratings attached to the laminated composite during the cure. The Particle Image Velocimetry (PIV) technique was recently used to measure strains in composite geogrids made of polypropylene (Gallage & Jayalath, 2019). Goda et al. (2019) used Photogrammetry to measure the deformation of a composite tank. This technique allows an accurate reconstruction of the 3D shape using digital pictures taken from different angles and positions. Kravchenko et al. (2015) used Digital Image Correlation (DIC) to measure the chemical and thermal shrinkage of resin. They used DIC as an in-situ technique to measure the cure-induced strain.

Monitoring strains and ply-movement during processing is essential to understand the interfacial ply behavior which can help devise methods that reduce the manufacturing defects during composite processing. Most of the studies that tried to understand the ply-movement/defects through experiments and modeling from literature are limited to out-of-autoclave or post-manufacturing examinations. In-autoclave and in-situ studies from literature are limited due to the experimental requirements of incorporating a monitoring setup inside an autoclave.

2.4. Processing Induced Residual Stresses in Composites

Residual stresses play a vital role in the manufacturing of composite structures. These stresses can be defined as self-balanced stresses that exist in the absence of any external loads which typically arise due to the differences between the mechanical properties of fibers and matrix during processing (Cheng & Finnie, 2007). They can also be observed when the cured structures are cooled from processing temperature to ambient temperature due to the different thermal expansion coefficients (CTEs) of the fiber and the matrix (Klingbeil et al., 2002). Other mechanisms that cause residual stresses include cure

shrinkage (Motagi et al., 2019), differences in material properties at the microscopic scale (Pawlak et al., 2001), and non-uniform degree of cure.

Residual stresses in composite laminates can be identified as intralaminar stresses (between fiber and matrix), interlaminar stresses (between plies), and laminate stresses (structural). Intralaminar stresses are created due to the mismatch of the physical and mechanical properties of fiber and matrix during cure, whereas the interlaminar stresses are due to the lamina anisotropy having different CTEs for individual plies in different orientations. Residual stresses exist in many structural components and often, the magnitude of these stresses is significant in designing structures with load-bearing conditions (Schajer, 2016). Neglecting these residual stresses can be detrimental in most cases as they cause warping (Klingbeil et al., 2002), undesired distortion (Wisnom et al., 2006), and dimensional instability (Chiang et al., 1994) in composite structures. Residual stresses in composite laminates will prestress the lamina and affect the overall strength by causing microcracks in the matrix material. These microcracks are a source of failure initiation by exposing the fibers to environmental degradation. Experimental observations from literature show that matrix cracking can be a source of delamination in laminated composites, which is catastrophic (Nairn, 2000; Tan & Nuismer, 1989).

2.4.1. Methods to Evaluate Residual Stresses

Researchers focused on a wide range of methods to measure the residual stresses in materials through experiments (destructive and non-destructive) and modeling (analytical and numerical). Chapman et al. (1990) used the layer removal method by placing separation films within a laminate during cure. The internal stresses that were originally present in the layer are eliminated by the layer removal method causing curvature. The

stress profile of the original laminate is derived using the measured curvature. Pagliaro and Zuccarello (2007) used the through-hole drilling method for studying the residual stresses in orthotropic materials. They obtained residual stresses using a theoretical study of the stress field present on orthotropic plates with a circular hole. The optical methods such as moiré interferometry (G. Melin & E. Asp, 1999) and fiber-optic Bragg gratings (Hannusch et al., 2016) have been used for measuring residual stresses in a composite laminate by using a modified hole drilling method. Wisnom et al. (2006) used the compliance method (Incremental slitting method) to measure through-the-thickness residual stresses in layered composite plates. In this method, the stress component can be measured by slitting specimens and calculating the compliance functions required for measuring the residual stress state in the laminate. Transverse residual stresses in cross-ply laminates are estimated using the first ply failure method (Kam & Sher, 1995). In this method, transverse residual stresses are measured as a difference between the transverse tensile strength of unidirectional material and the stress required to initiate transverse cracking when the same material is embedded in a cross-ply laminate.

Most of these are destructive methods, whereas non-destructive methods like x-ray diffraction (Benedikt et al., 2002), neutron diffraction (Pintschovius, 1989; Stacey et al., 1985), photoelasticity (Pawlak et al., 2001), acoustic waves (Nikbakht et al., 2017) and Raman spectroscopy (Jannotti et al., 2017) are also used for measuring the residual stresses. However, requirements like crystallinity make x-ray diffraction and neutron diffraction methods inapplicable for carbon fiber composites, micro-Raman spectroscopy is used to study the deformation micromechanics of carbon-fiber-reinforced composites through the stress-induced change in frequency (Jannotti et al., 2017). Nairn et al. (1985)

used photoelasticity to measure the magnitude of the residual stresses in unidirectional graphite composites. They transmitted light through the thickness of the laminate to measure the in-plane stresses. Duquennoy et al. (1999) used ultrasonic Rayleigh waves to evaluate residual stresses in orthotropic materials using the changes in wave velocity. Temperature-related change in curvature is used to measure residual stresses in unsymmetrical laminates (Schajer, 2016). This technique of measuring stresses relies on finding the 'stress-free' temperature and using classical lamination theory (CLT) to find the mesoscale stresses at other temperatures. The cure referencing method is used to measure the residual stresses using moiré diffraction grating on the surface of the laminate before the gelation of the resin (P. G. Ifju et al., 2000). The longitudinal residual stresses are calculated using the strains measured by the moiré interferometry after a cure.

The 3D-DIC for in-situ real-time evaluation of APS coating curvature and residual stresses was used by Croom et al. (2016). Results of residual stresses model derived using Euler-Bernoulli beam theory and liner-elastic materials models were compared to the experimental curvature measurements obtained by DIC. They observed that the model matched within 5% of the experimental results. Bartlett and Li (2019) provided an overview of residual stresses in metal powder bed fusion (PBF). The complex residual stress distribution is developed in parts prepared using PBF processing as multiple layers are not instantaneously and uniformly heated or melted. Layers are heated following the 'scan/raster strategy', allowing sections to heat and cool independently resulting in a complex heat transfer problem. Several in-situ techniques are implemented to measure or infer the residual stresses and distortion during production. Integrating strain gauges into the base plate to measure strain changes with the addition of new layers is one of them.

A non-destructive framework for residual stress measurement in Selective laser melting (SLM) parts using 3D-DIC to capture in-situ surface distortion was developed by Bartlett et al (2018). They also developed a 2D analytical model to convert DIC measurements to in-plane residual stresses and used XRD to validate the 3D residual stress measurements. They observed that residual stresses emerged from sequential re-heating and cooling of the new surface and changed dynamically between layers. Péron et al (2017) proposed a thermomechanical model based on modified laminate theory to predict the strains and residual stresses at the ply scale of a thermoplastic composite laminate during the cooling. The curvature measurements are performed using DIC and are compared with the model predictions. The temperature and crystallization gradients through the thickness of the part are computed according to a coupled model and compared with experimentally determined values. They compared the curvature and stresses between their model and Classical Lamination Theory (CLT) and stated the need to account for the actual evolution of the thermomechanical properties during cooling in measuring them.

In addition to the above-mentioned experimental methods, there have been several modeling methods developed to measure and predict the formation of residual stresses in composite materials. Liu and Shi (2018) proposed an improved analytical solution to consider thermo-viscoelastic effects on residual stresses and deformations of flat composite laminates during curing. They developed an analytical solution for incremental differential equation derived to describe the viscoelastic behavior by assuming the solution at the current time is a linear combination of the corresponding Laplace equation solutions of all time. The validated the analytical solution by comparing the results to

results of both experimental and viscoelastic FEA. They found out that the effects of cure shrinkage of the polymer matrix on the residual stresses and deformation for unsymmetrical composite laminates depend on the degree of cure and cure cycles.

For calculating the residual stresses, Parlevliet et al. (2006) identified the necessary parameters as the shrinkage of the matrix and fiber (α), the temperature difference between stress-free temperature and service temperature (ΔT) and the elastic moduli of fiber (E_f) and matrix. All these values can be substituted into the following formula to find the residual stresses in the longitudinal direction at a certain temperature.

$$\sigma_f = E_f(\alpha_f - \alpha_m)\Delta T \tag{2.1}$$

A non-destructive Cure Referencing Method (CRM) is developed by Ifju et al. (2000) to measure residual stresses in laminated composites by incorporating the use of moiré interferometry and replication of diffraction gratings on the surface of the laminates in the autoclave during curing. The CRM was evaluated by calculating the residual stresses using laminate theory. The residual stresses are calculated for each ply using the orientation of the ply and the material properties using the following equation where [T_k] is the transformation matrix associated with the ply orientation, [Q] is the laminate stiffness matrix, {$\boldsymbol{\varepsilon}_{diff}$} is the strain difference between unidirectional and multidirectional laminates.

$$\{\sigma_{res}\}_k = [T_k]^{-1}.[Q].[T_k].\{\varepsilon_{diff}\}_k \tag{2.2}$$

A method to characterize multidimensional laminate behavior eliminating testing of each desired layup was described by Schulz et al (2005) by modifying Classical Laminate Theory (CLT). This method predicts the behavior of multidirectional laminate based solely on the behavior of a unidirectional sample of the same material system. Their

measurement of the strain as a function of temperature using the Cure Referencing Method (CRM) also allowed the residual stresses within the composite panels to be quantified. Including chemical shrinkage of the material as well as its expansion properties as a function of temperature in CLT significantly decreased the need for time to test all the sample configurations.

Kim and Lee (1997) used intermittent curing of an unsymmetrical laminate to monitor residual stresses. They measured the warpage to assess the extent of residual stresses during cure. While doing that they observed that transverse modulus increases sharply and then levels off after the gel point while the transverse tensile strength starts to build up only after the gel point and according to them, the gel point is one of the key parameters controlling the residual stresses and mechanical properties. Ding et al. (2016) proposed the formulation of a thermo-viscoelastic law that considers the thermal dependence on residual stresses during curing. Their formulation takes account of thermal expansion, chemical shrinkage, and stresses relaxation. This formulation is later incorporated into ABAQUS, and they evaluated the effects of thermal dependence on the residual stresses and distortions in the composite structures. The temperature-dependent residual stress ($\sigma(t)$) is derived with 'τ_r' as relaxation time at the reference temperature, '*C'=1/*$k(T_0)$as the stress at time t = 0 is equal to the spring stiffness ($k(T_0)$) and 'ξ' is the current reduced time.

$$\sigma(t) = C\ exp(\ lnk(T)).exp(\frac{\xi}{\tau_r}) \tag{2.3}$$

Residual stresses and CTE over a broad range of temperature in composite laminates were calculated by Schulz et al. (2005) using a combination of strain gauges and the Cure Reference Method (CRM). They developed an experimental approach using

shear specimens to test the material properties (E_2 and G_{12}) as a function of temperature. These properties are used in their Classical Laminate Theory (CLT) model to determine the residual stresses as a function of temperature. Puhringer et al. compared the mechanical properties of a polypropylene homopolymer at elevated temperatures through tensile tests and DMA measurements. They performed the tensile tests at different temperatures and determined the Young's Modulus through the stress-strain curves at the respected temperatures. They later determined the storage modulus through dynamic mechanical testing at 1Hz using a three-point bending setup. They observed that the curve of the flexural storage modulus showed a good correlation to the Young's Modulus and the tensile strength taken from elongation tests at elevated temperatures.

Temperature-dependent elastic moduli of two cured epoxy systems were measured by Deng et al. (2007) using Dynamic Mechanical Analysis (DMA) with different loading fixtures and compared them with mechanical testing results under various temperatures. They observed that there is a good agreement between both DMA results and normal mechanical tests results. They also found that a three-point bending mode was found to be most suitable for measuring temperature-dependent moduli by DMA as it can eliminate clamping effects. Tavakol et al. (2013) proposed a 3D coupled thermomechanical FEA to predict the process-induced residual stresses by incorporating cure kinetics, cure shrinkage, thermal strains, tool-part interface, and development of mechanical properties during cure into the modeling. The cure shrinkage for a particular direction was estimated using Equation 2.4.

$$\varepsilon_i^s = C_i(\sqrt[3]{1 + V_r^s} - 1) \tag{2.4}$$

Where, ε_i^s is cure shrinkage in the direction i, V_r^s is volume cure shrinkage and C_i is the coefficient of directional cure shrinkage determined from DMA and thermomechanical Analysis (TMA).

Residual stresses in a laminate are estimated by Cowley and Beaumont (1997) as the difference between the in-situ tensile strength of a cross-ply laminate and the tensile strength of a unidirectional specimen as there are no residual macro-stresses in a unidirectional specimen. They compared their experimental results with a theoretical model of residual stresses based on classical lamination theory. They found that 'stress-free' temperature coincided with the T_g of the matrix, at which point matrix softening occurs and stresses are no longer sustained. White and Hahn (1993) used classical laminate theory to assess the mechanical property and residual stress development during the cure of a Gr/BMI composite. They measured the warpage of a $[0_4/90_4]_T$ cross-ply specimen to monitor the residual stress build-up. They observed that the longitudinal and transverse properties are cure-dependent with longitudinal modulus increased by 50% during cure and the longitudinal strength increased by 70-80%. They also observed that thermal strains during cool-down are dominant in residual stress development and chemical shrinkage strains are found to be negligible in residual stresses development as chemical shrinkage occurs at high temperature when the modulus is low and stress relaxation can take place without residual stresses. An experimental study of the effect of processing conditions on toll-part interaction induced warpage was presented by Twigg et al. (2004b, 2004a). They observed that maximum warpage is affected by the length (L), thickness (t) of the part, and the processing pressure (P). They empirically determined proportionality to predict the maximum part warpage (w). They also proposed an

analytical model based on the assumption that slip occurs between the 1st and 2nd plies of the laminate as well as tool part interface that agreed well with the experimental results.

$$w_{\max} \propto \frac{P^{0.2} \cdot L^3}{t^2} \tag{2.5}$$

Embedded strain gauges were used by Crasto and Kim (1993) to follow the buildup of residual strains in carbon fiber reinforced laminates during cure. They used three different cure cycles during cure and observed that stress relaxation occurs by providing adequate time to balance matrix cure shrinkage and thermal expansion. This relaxation successfully reduced cure shrinkage stresses in AS4/3501-6 composites used in this research. Sunderland et al. (2001) developed a numerical model to predict internal and residual stresses during the processing of thermoplastic matrix composites based on finite element formulation. They observed that for cross-ply laminates, the interlaminar residual stresses have more impact on the warpage than the through-the-thickness residual stresses caused by the cooling profile.

The development of residual stresses in [0/90] unsymmetric flat laminates was analyzed in a recent study by stopping the cure cycle at pre-determined points and evaluating the related deformation (Wisnom et al., 2006). The stress-free temperature of the laminates was measured by eliminating the curvature by re-heating the samples. Umarfarooq et al. (2019) studied the influence of residual stresses on the interlaminar fracture toughness of carbon/epoxy laminates. They used the slitting method to determine the residual stress distribution in post cured laminates and double cantilever beam (DCB) test for interlaminar fracture toughness. They observed that as the post-curing temperature increased, the residual stresses gradually increased and with the increase in compressive residual stresses, the fracture toughness increased.

Monitoring the evolution of residual stresses throughout the cure is essential to understand the change in the mechanical behavior of composites. This understanding can help devise methods that reduce the residual stresses thus reducing defects during composite processing. Most of the studies that measured the residual stresses from the literature are limited to after-cure. The continuous evolution of residual stresses throughout the cure is limited due to the experimental requirements of incorporating a monitoring setup inside an autoclave.

2.4.2. Methods to Reduce Residual Stresses

Researchers developed various methods to reduce residual stresses in composites. Kim et al. (2006) proposed a smart cure cycle to reduce fabrication thermal residual stresses in co-cure bonded steel/carbon epoxy composite by adding abrupt cooling and reheating to the manufacturer-recommended cure cycle. They used DSC (to obtain the degree of cure) and rheometer (to measure viscosity) to obtain the optimal time to apply the cooling operation. Their first observation was when the degree of cure (DOC) is above 0.5 the bonding temperature increases and when it is below 0.5, there is incomplete bonding. Viscosity also abruptly increased after DOC 0.5. Their second observation is while reheating the bonding temperature increased for the sample cooled at DOC 0.2 and there is a slight change in bonding temperature when the sample is cooled after DOC 0.2. From these two observations, they concluded that the abrupt cooling point should be between DOC 0.2 and 0.5. The interfacial strength for the lap joint sample decreased when the sample is cooled after DOC 0.6. For the sample cured at DOC 0.5, the strength is 13% higher than the sample cured with manufacturer-recommended cure cycle (MRCC) suggesting that an abrupt cooling process is essential to reduce thermal stresses.

They also observed that the tensile strength of the specimen cured with abrupt cooling and reheating was 43% higher than MRCC in the fiber direction. So, with their smart cure cycle, they were able to decrease thermal stresses, improve both interfacial strength and the material strength of the composite.

Another cure cycle modification was developed by Soohyun et al. (2015) to reduce the thermal residual stress of the co-cured E-glass carbon epoxy structure with the degree of cure and post-cure process. Their three-step process for optimizing the cure cycle consists of cure-triggering, cooling, and post-cure process. Cure-triggering consists of T_{max} (maximum temperature during cure) and t_{const} (duration of T_{max}). The degree of cure is measured by DSC to determine the cooling point in the cure. The residual stresses were calculated from the radii of curvature.

The duration of the post-cure process is calculated from the partially cured resin dissolution experiment. Their smart cure cycle consists of cure-triggering at T_{max} = 105^{o}C, a cooling point at DOC 0.4, and a post-cure process time of 6 hrs. Prussak et al. (2019) also developed a smart cure cycle to reduce process-related thermal residual stresses in co-cured bonded fiber metal laminates using fiber Bragg grating (FBG) sensors. They reduced the stress by up to 23% by making modifications to the temperature cycle, cooling, and heating rates. They found that cooling before the gelation point at which the DOC is 0.45 could lower the bonding temperatures thereby decreasing the thermal elongation resulting in less residual stresses.

The optimal cure cycle parameters for minimizing residual stresses in asymmetric cross-ply laminates were developed by Shah et al. (2018) using a genetic algorithm and Latin hypercube sampling method. They found that for a cross-ply laminate with the ratio

span/thickness of 12.5, one optimal cycle reduces residual stresses by 47% and the total cure time from the MRCC time of 5 h to 4 h and another optimal cycle reduces the total cure time to 2 h and residual stresses by 8%. They numerically analyzed the curing of thermoset-matrix composites with functionalities built in the commercial software COMPRO for modeling the curing process, the finite element (FE) software ABAQUS for obtaining numerical solutions of the corresponding Initial-Boundary Value Problems (IBVPs), and MATLAB for the genetic algorithm.

An improved analytical solution to consider thermo-viscoelastic effects on residual stresses and deformations of flat composite laminates during curing was proposed by Liu et al. (1999; 2012). They derived an incremental differential equation to describe the viscoelastic behavior of composite materials during curing and developed an analytical solution to solve the equation by assuming the solution as a linear combination of the corresponding Laplace equation solutions of all time. They also observed that the effects of cure shrinkage of the polymer matrix on the residual stresses and deformation for unsymmetrical composite laminates depend on the degree of cure and cure cycles. Chemical shrinkage of the resin during the recommended cure cycle contributes to the residual stresses and curvature by about 17%.

Stepped cool-down mode with subsequent fanning to control stress relaxation and thermal residual stress during the cure of random fibre mat-reinforced polyester composites is another method used by Agbo et al. (2017). They adopted ten cure cycle modes to cool down the composites to ambient temperature which are cured at 85^{o}C for 3 hours after wet layup. Among the ten cure cycles, they found that the cool-down path from 85^{o}C to 60^{o}C to 30^{o}C ambient plus fanning relaxed out the developed residual

stresses immediately upon cooling. They also observed a 37% difference in strength comparing the composite cured at 85^{o}C with quench cooled and cooled in steps plus fanning.

A cure monitoring system using dielectrometry and a fiber Bragg grating (FBG) sensor was devised by Kim et al. (2006) to reduce thermal residual stress in carbon/epoxy composites. They obtained three rapid cooling points at 33.5, 35.5, and 37.5 min where the derivative of the dissipation factor was a maximum. These three points are used to control the bonding temperature of the interface between the fiber and resin by optimizing the cure cycle. The thermal residual strain of the specimen fabricated by rapidly cooling at 35.5 min decreased by 48.6% compared to the specimen with the ordinary cure cycle. The flexural strength of the specimen fabricated by rapidly cooling at 35.5min also improved by 20.6% compared to the ordinary cure cycle.

Strain evolution and curing reaction of composite laminates to reduce the thermal residual stress in a composite laminate with a stacking sequence of $[0_5/90_5]_s$ using dielectrometry and a fiber Bragg sensor was developed by Kim et al. (2006; 2006). They observed a 50% reduction in thermal residual stress during fabrication by adjusting the cure cycle along with improving 16% of static strength. They believe that this reduction in residual stress is because of a decrease in the bonding temperatures between adjacent plies as the gelated epoxy resin during the abrupt-cooling operation could well dissipate the thermal strain due to the resin's highly visco-elastic property.

Another method for reducing residual stresses is by modifying the ply interfaces. Niu et al. (2019) used Raman spectra of the inner SiC fibers and surface C-rich layers of SiC fibers, composite precursors, and SiC_f/Ni-Cr-Al composites measured using Raman

spectroscopy to calculate the residual stresses of the inner SiC fibers. They analyzed the effect of the $Al+Al_2O_3$ diffusion barrier layer on the interfacial residual stresses in the composites and observed that the existence of this barrier improves the compatibility of the SiC_f/Ni-Cr-Al interface and relives the residual stresses inside the SiC fibers and at the interface of the composite material. Ghasemi et al. (2015) studied the effects of carbon nanofibers (CNFs) on thermos-elastic properties of carbon fiber composite for the reduction of thermal residual stresses using the micromechanical model. They used this model to calculate the CTE and Young's modulus of their CNF carbon fiber specimen to compare with experimental results. They also employed CLT to determine the residual stresses for different layups. They found that adding 1% CNF reduced the residual stresses in the unsymmetric cross-ply laminate by up to 27%.

2.5. Process Modeling of Composites

Aerospace composites are cured in an autoclave under high temperature and pressure conditions. This process involves the transfer of heat and thermal mass through chemical reactions and a fixed airflow pattern inside the autoclave. This is a multiphase system with time-dependent material properties and boundary conditions which can lead to an inhomogeneous temperature distribution inside the composite part, causing defects or unwanted dimensional changes. Therefore, understanding and improving the efficiency of this process is essential to reduce the production cost and improve the part quality. Several researchers in the past developed the processing science of epoxy resin composites using fundamental principles through modeling and experiments. Two of the most common methods from the literature are heat transfer models and cure simulations.

2.5.1. Autoclave Heat Transfer Modeling

Autoclaves are widely used for the manufacture of composite parts for high-performance components of aircraft and other industrial applications. Typical autoclave processing steps employ high temperatures and high internal pressures to enable curing as well as consolidation of the composite material. Often multiple parts and mold assemblies are processed together in the autoclave, which disturbs the convective heat transfer within the autoclave and results in local conditions on the part surface which are different from ideal temperature, pressure, and heat transfer coefficient (HTC). For example, the relative placement of the mold and tooling within the autoclave could lead to shadowing effects (both inter-part shadowing and intra-part shadowing) which in turn influence the pressure and temperature conditions at the surface of the part, affect the thermal gradients setup in the part and lead to defects in the form of voids, porosity, resin redistribution, and poor fiber consolidation. The quality of the autoclaved parts as well as necessary curing time is strongly linked to the thermal behavior of the mold. To increase the composite part quality, reduce manufacturing costs and increase autoclave capacity, there is a need to thermally optimize the autoclave processing.

Bohne et al. (2018) investigated the heat transfer inside an autoclave using lumped mass calorimeter measurements of HTC and a fluid dynamics model. They observed that the process pressure and position inside an autoclave have a significant influence on the heat transfer while temperature and heating rates did not influence the HTC. They developed a computational fluid dynamics model and comparing the results of the model with the experimental data, they observed a nearly stationary HTC throughout the curing process. They also observed that parts placed in the regions of low flow velocity inside an autoclave like in the rear region need more time to cure compared to the parts placed near

the inlet. When multiple parts of different thermal masses are cured at the same time, they recommend placing the smaller parts at the rear and larger parts at the inlet to achieve uniform curing. From their analysis, they recommend using higher pressure and inlet velocity to raise the heat transfer inside the autoclave which reduces the total cure cycle time.

The heat transfer is the key factor for curing composite parts inside an autoclave. Three different forms of heat transfer can be observed inside an autoclave such as the heat produced by the chemical reaction of the resin through the thickness of the part, the conduction between each ply in the layup, and the forced convection between the solid and the moving fluid (Johnston et al., 1998). Computational fluid dynamics (CFD) simulations are performed by Kluge et al. (2016) to predict the temperature distribution of a part inside an autoclave using the experimental data as an input for the simulations. They performed the CFD simulations with and without the effect of radiation and compared the results to the experiments. They concluded that CFD can be used as an effective tool to predict the heat transfer inside an autoclave and the thermal radiation should be considered when modeling the simulations.

Hybrid models that utilize CFD coupled with heat transfer have been developed but need experimental validation for each configuration of autoclave run. More recently, to quantify the variation in heat transfer characteristics within an autoclave, Weber et. al. (2017) developed a “shift-factor” approach. The shift-factor approach tries to incorporate flow effects by simply shifting a measured reference curve to a higher or lower HTC based on the orientation of the part surface with respect to convective flow within the autoclave. Shift factors are generated as a function of different mold surfaces, different

positions, and a variety of flow conditions within an autoclave. Using a catalog of such shift factors, the boundary conditions on every single mold surface could be obtained by comparing its angle towards the flow, as well as its position in the autoclave and current loading conditions, referenced to a base case scenario. The approach allows for a fast BCs estimation and set-up for manufacturing process simulation

2.5.2. Composite Cure Simulations

Traditional autoclave processing relied on conservative approaches or tooling designs based on past experiences, which allowed for optimization only after the mold was manufactured and tested. The need for tool optimization at the design phase has led to manufacturing process simulation (Abdelal et al., 2013) and tools like COMPRO and ANSYS, which provide a virtual framework for process optimization (Bedayat et al., 2018).

ANSYS is one of the widely used tools for composite simulations. Meng et al. (2019) used the ANSYS ACP module to study the performance of a composite wing with a large aspect ratio by performing the stress analysis and observed that adding an external device to the wing with its center of gravity at 15% before the gravity line resulted in the smallest deformation of the wing tip. They also observed that adding a 300mm winglet at the tip of the wing reduced the maximum deformation of the wing by 47% compared to the base model. By adding composites to the wing, they observed that reduced the weight of the wing by 42% with smaller deformations compared to a metal wing.

The fiber orientation on multilayer composite structures composed of different materials is analyzed by Venkatesan et al. (2020) by testing various fabrics such as glass, carbon, and Kevlar with an epoxy matrix. They used ANSYS ACP for the finite element

modeling of the tensile test based on the ASTM D3039 standard. Among all the materials tested, they concluded that prepreg-carbon-woven material is more suitable for components that are used in tensile conditions. Das et al. (2013) performed static analysis using ANSYS Mechanical APDL for initial delamination of symmetric composite laminates with and without wrap-around which is an edge delamination suppression technique. To further understand the delamination parameter, they extended their analysis in terms of strain energy release rate utilizing the modified crack closure integral technique. Through their analysis, they found that the stress around the edge delamination/crack tip significantly decreased using the wrap-around technique from 1.9x108 Pa to 0.13309 Pa for a wrapped laminate (+22/-22/90). Ozyildiz et al. (2018) used ANSYS APDL scripting language to implement Puck failure criteria and degradation rules for the failure analysis of a wind turbine blade. They found that the root and trailing edge of the blade have the highest risk of failure initiation and need to be redesigned. They also used the ANSYS ACP module to evaluate and visualize Tsai-Wu inverse reserve factors and Puck failure exposures in the turbine blade.

ANSYS composite cure simulation (ACCS) software tool is primarily used to simulate the curing behavior of the resin. It was developed by LMAT as a reliable simulation platform to support manufacturing and tooling engineers throughout the process design cycle. During the curing of thermosetting composites, the resin undergoes cross-linking resulting in gelation and vitrification which causes thermal and resin shrinkage. This sophisticated behavior of the resin can be captured by the ACCS material curing model making ACCS one of the very few tools to effectively model the complete composite cure process inside an autoclave. An approach to predict the final shape of the

composite part using ACCS was proposed by Patil et al. (2019). They also presented the thermal results of composite parts during cure. They applied ACCS chemical solver in the transient thermal module and simulation for the development of polymerization and glass transition temperature. They observed that the simulation results are 11% better than analytical calculations. Through this process, they conclude that it is possible to obtain the values of dimensional changes for different curing temperatures and cure cycles.

Kumbhare et al. (2021) investigated the process-induced shape deformations in composite structures and compared results to finalize the design parameters. Latin hypercube sampling (LHS) method was used to generate the random ply orientation angles. These values are then used in the ACCS tool to find the stress and distortion values. They used the ACCS tool to generate data with different references like curing cycle and layup symmetry. From the ACCS data, they observed that the single hold cure cycle caused more deformation compared to the double hold cycle. ACCS tool was also used to calculate processing induced stresses in composites to prevent warping (Shabalin et al., 2021). While ACCS has been used in the past to analyze deformations like spring-in, warpage, and residual stresses in composite structures (A. Patil et al., 2019), in this research ACCS tool was used to validate the warpage created in asymmetric layups in the experiments.

Sreekantamurthy et al. (2016) developed cure process models to analyze and understand the laminate cure responses with reference to the physics of the curing process. They used COMPRO software to simulate the cure process responses using the material properties available in the material database. COMPRO is another software tool

used by researchers to model the composite cure process. They compared the results from thermo-chemical, flow-compaction, and structural analysis results of 2D and 3D models with reference to the formation of residual strains and warpage. They found that many cure process results from the simulation were traced to the physical phenomenon occurring during cure such as cure kinetics, shrinkage, resin flow, and compaction. Twigg et al. (2004b, 2004a) conducted a parametric study of tool-part interaction induced warpage using COMPRO and compared the results with experimental warpage trends. They found that the elastic shear layer they used is unable to capture the shear stress that arises due to the sliding friction condition at the tool-part interface. The workaround they suggested to predict the warpage accurately is to adjust the shear layer stiffness. They also found that distribution of in-plane stress through the thickness of the part is also critical for accurate modeling of warpage.

The effect of tooling material, tool-surface condition, and cure cycle on spring-in behavior of composite laminates were studied by Fernlund and Poursartip (1999). They used COMPRO to predict the flange spring-in after cure and compare with experiments. They found that the two-hold cure cycle gives more spring-in than a single-hold cycle irrespective of the tool-surface condition because of the tool-induced stretching of the part during the second ramp-up. Comparing the experimental results with COMPRO predictions, they found that the predictions are about 20% higher than the experimental results. Hubert and Poursartip (2001) measured the compaction curve of unidirectional and quasi-isotropic AS4/3501-6 carbon epoxy prepregs. The compaction curve obtained is used in COMPRO to simulate the uniaxial compaction of 8 and 16 ply laminates at different temperatures. They found that the force-displacement response from the

simulations matched the experimental results. They also suggested that this method can be applied to other types of composite systems like woven and non-woven fabrics and this method can be used to process models to predict the laminate compaction under different processing conditions.

In summary, most of the studies that measured the residual stresses from the literature are destructive. Non-destructive monitoring methods such as AC and DC measurement, conductive nanocomposites, Carbon Nanotube (CNT) network, and hybrid CNT graphite nanocomposites, etc are limited to post-cure measurements. In-situ approaches that use sensors like embedded strain gauges and fiber optics introduce a foreign body into the laminate which changes the material properties. Approaches for continuous evaluation of residual stresses during cure are limited due to the experimental requirements of incorporating the monitoring setup inside an autoclave. Monitoring the evolution of residual stresses throughout the cure cycle will help in developing a deeper understanding of the manufacturing process. This can lead to changes in the manufacturing process that lower the residual stresses and thereby mitigate the associated processing defects and strength reduction. The focus of the current research is to address all the above constraints and develop an experimental approach to identify the conditions that cause ply-movement during manufacturing and continuously evaluate the processing induced residual stresses in composite laminates during cure. Further, the effect of layup configuration on the residual stress evaluation is examined by analyzing and comparing several symmetric and asymmetric layup configurations in subsequent chapters. Finally, a thermomechanical cure model is developed to understand the curing process through composite cure simulations.

3. Continuous Evolution of Processing Induced Residual Stresses

Processing induced residual stresses are often responsible for causing warping, undesired distortion, dimensional instability, and delaminations in composite structures. Monitoring the evolution of residual stresses throughout the cure is essential to understand their effect on the mechanical behavior of the composites. Most of the studies that measured the residual stresses from the literature are limited to post-cure measurements. In-situ approaches that use sensors like embedded strain gauges and fiber optics introduce a foreign body into the laminate which changes the material properties. Approaches for the evaluation of residual stresses continuously during cure are limited due to the experimental requirements of incorporating the monitoring setup inside an autoclave. In this chapter, a novel in-situ experimental approach is developed to measure the dimensional changes in the laminates during cure and combined with temperature-dependent moduli obtained from Dynamic Mechanical Analysis (DMA) to calculate the continuous evolution of residual stresses during composite processing. Further, the effect of layup configuration on the residual stress evaluation is examined by analyzing and comparing several symmetric and asymmetric layup configurations.

3.1. In Situ Experimental Procedure & Characterization

3.1.1. Experimental Setup

Unidirectional carbon fiber prepreg procured from Fibre Glast Corporation containing 12K tow raw material is pre-impregnated with an epoxy resin system of density 1.2 g/cc and has a fabric areal weight of 139 g/m^2. This prepreg is cured at the manufacturer-recommended curing temperature of 120°C (248 F) with a one-hour hold time. The specimen temperature is measured using a J-type thermocouple inside the autoclave. The

specially designed autoclave from ASC Systems is instrumented with a 3D digital image correlation (DIC) setup as shown in Figure 3.1. This autoclave is also equipped with borosilicate glass viewports on one side with an interior light which enables the DIC cameras to capture the pictures of the speckle pattern continuously and measure the changes as seen in Figure 3.1(b).

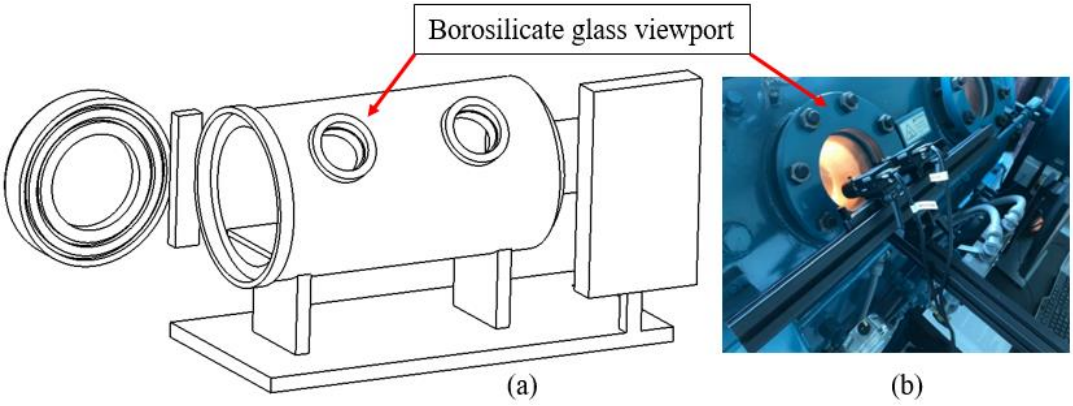

Figure 3.1 (a) Schematic of the autoclave with viewports; (b) DIC monitoring setup.

The cameras of the DIC system are set up pointing at the speckle pattern on the composite layup focussed through the viewport of the autoclave. The VIC-3D Real-Time DIC System from Correlated Solutions measures the surface ply deformations and strains during the composite processing by extracting full-field information from the high contrast random speckle pattern sprayed on the surface ply as seen in Figure 3.2 using high-temperature spray paint. Composite specimens of dimensions 101.6 mm x 152.4 mm (4-inch x 6-inch) are prepared for fabrication using four plies of unidirectional carbon fiber prepreg in two symmetric orientations of $[0/90]_s$, $[0/45]_s$, and two unsymmetric orientations of [30/-30/60/-60], [0/30/45/90] and one anti-symmetric orientation of [45/-45/45/-45].

3.1.2. Dynamic Mechanical Analysis (DMA)

Dynamic mechanical analysis (DMA) using PerkinElmer - DMA 8000 is performed to characterize temperature-dependent dynamic viscoelastic properties of the composite material used in this research. A small unidirectional four-ply sample of dimensions 50 mm x 7.5 mm was mounted using a three-point bending setup to obtain both temperature-dependent longitudinal and transverse modulus of the material.

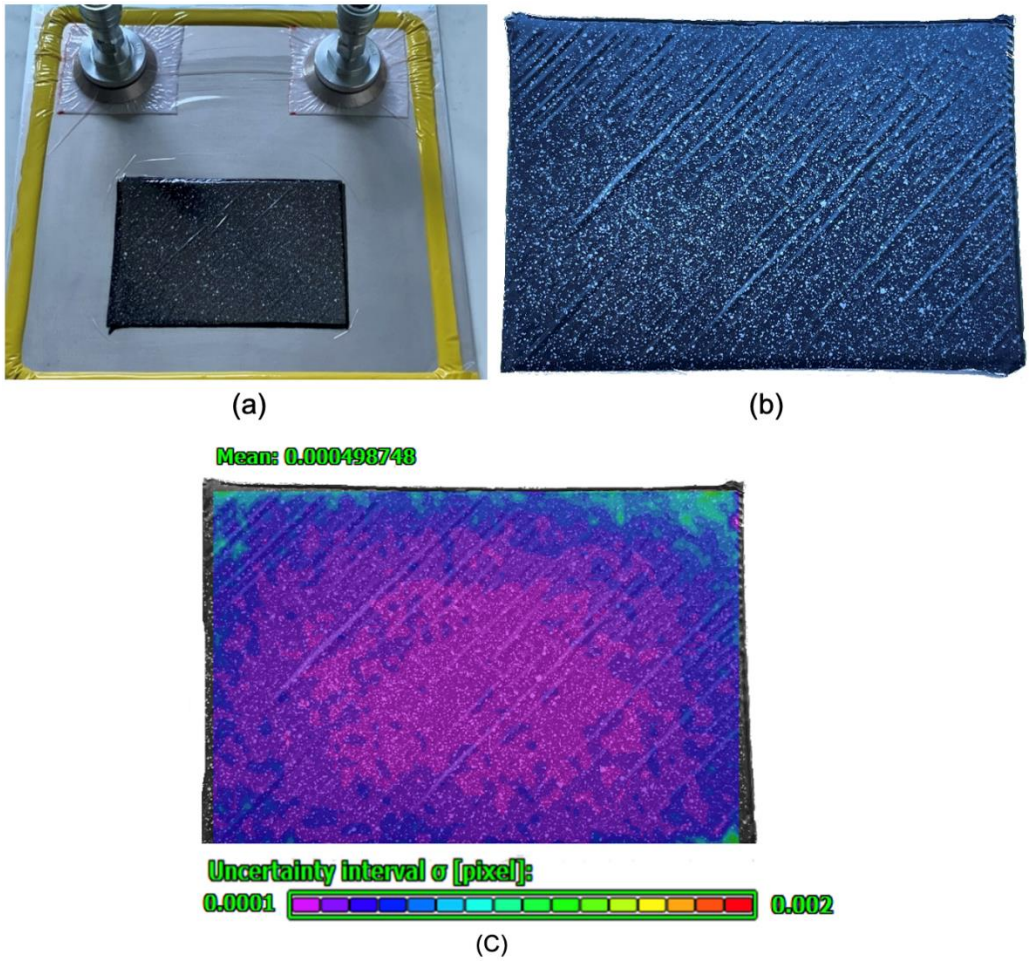

Figure 3.2 [45/-45/45/-45] laminate: (a) under vacuum bagging; (b) speckle pattern after cure; (c) DIC uncertainty of speckle pattern.

3.1.3. Differential Scanning Calorimetry (DSC)

Differential scanning calorimetry (DSC) using DSC-3 from Mettler Toledo is performed to measure the degree of cure for the prepreg resin used in this research. Resin

samples of weight 25 mg to 35mg extracted by scraping from the prepreg were placed and sealed in 40 µL aluminum crucibles. The experimental procedure is carried out in two steps, dynamic and isothermal. First, the samples are heated at a constant rate of 10°C/min between -25°C to 250°C (dynamic) and the temperature was held constant at 120°C (isothermal) for a time of 0 min to 60 min with 10 min intervals. The degree of cure of the resin from the composite sample at these 10 min intervals was calculated and plotted by comparing the isothermal heat of reaction to the total heat of reaction until complete cure.

3.2. Results & Discussion

3.2.1. Temperature-Dependent Elastic Properties

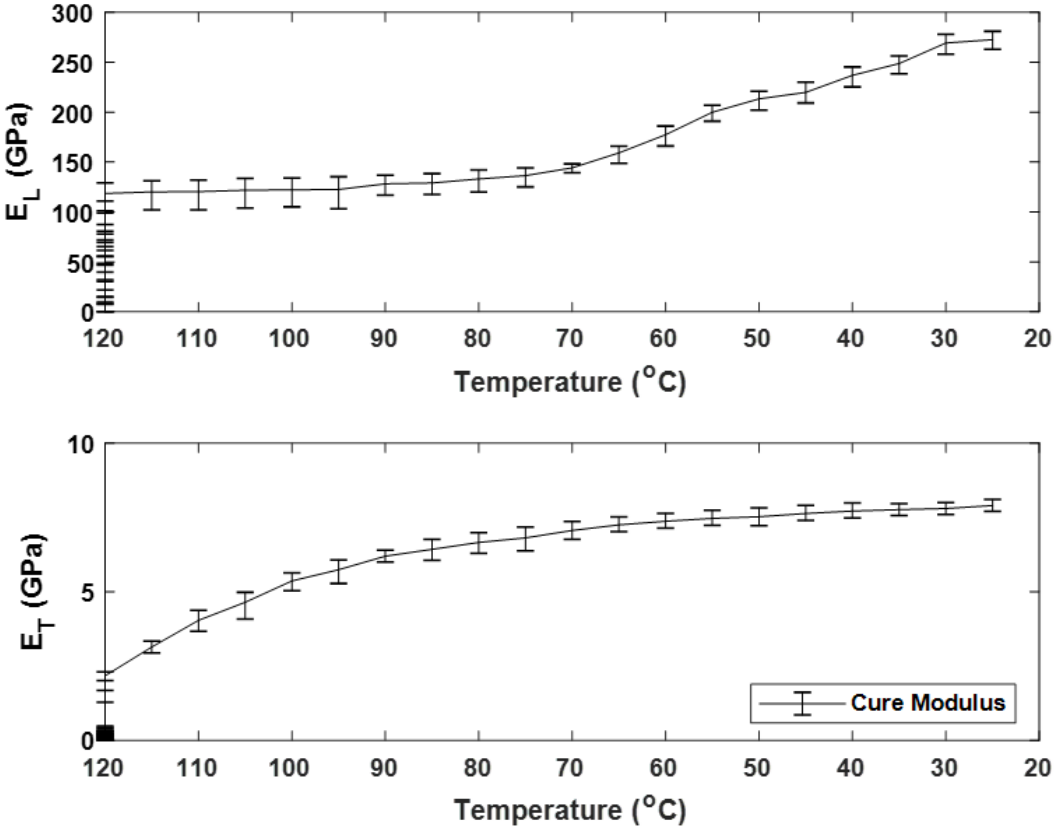

Figure 3.3 Change in Young's Modulus (EL and ET) to temperature

The results from the DMA are analyzed during the hold and cool-down phases of the cure cycle. Temperature-dependent Young's modulus ($E_L(T)$ & $E_T(T)$) values are experimentally extracted through the DMA of the sample and are plotted against temperature. The average change in modulus during the cool-down phase for four different samples can be seen in

Figure 3.3. The rate of change in longitudinal modulus is lower during the initial cool-down phase and then increases to an average of 272 GPa at room temperature. On the other hand, the transverse modulus increases sharply and then gradually levels off towards the end to 7.9 GPa at room temperature. The manufacturer provided tensile modulus for the prepreg is 275.8 GPa. A similar trend of change in modulus is also observed by Li et al. (2020) in their theoretical model and the experimental measurements of Kim and Hahn (1989). The error bars denote the standard deviation from four different samples.

3.2.2. Cure Kinetics

The cure kinetics of the resin was analyzed using the DSC and the degree of cure (DOC) (α) is calculated as the ratio of change in heat of reaction (ΔH_t) and total heat of reaction (ΔH_{total}) as shown in Equation 3.1 (Hardis et al., 2013).

$$\alpha(t) = \frac{\Delta H_t}{\Delta H_{total}} = \frac{\Delta H_{total} - \Delta H_R}{\Delta H_{total}} \tag{3.1}$$

Where, ΔH_R is the residual heat of reaction for the isothermally cured sample at 120°C for time (t). The total heat of reaction is measured through dynamic scanning test form -25°C to 250°C at a predefined heating rate of 10°C/min as the resin is completely cured. The degree of cure for the hold-phase and cool-down phase of the cure cycle can be seen in Figure 3.4.

The ΔH_R after the ramp-up with zero isothermal hold time corresponds to a degree of cure of 20%. Therefore, the B-stage resin in the prepreg is 20% cross-linked as-procured. The epoxy reaches vitrification, the point at which resin is converted from a rubbery state to a glassy state at 70 minutes. Comparing the mobility in the vitrified state before and after 70 minutes, the mobility after 70 minutes is much lower to permit further reaction, hence this point is considered as a vitrification point (Montserrat, 1992). This corresponds to 94% cross-linking as seen in Figure 3.4. The resin is 97% cured at the end of the cure.

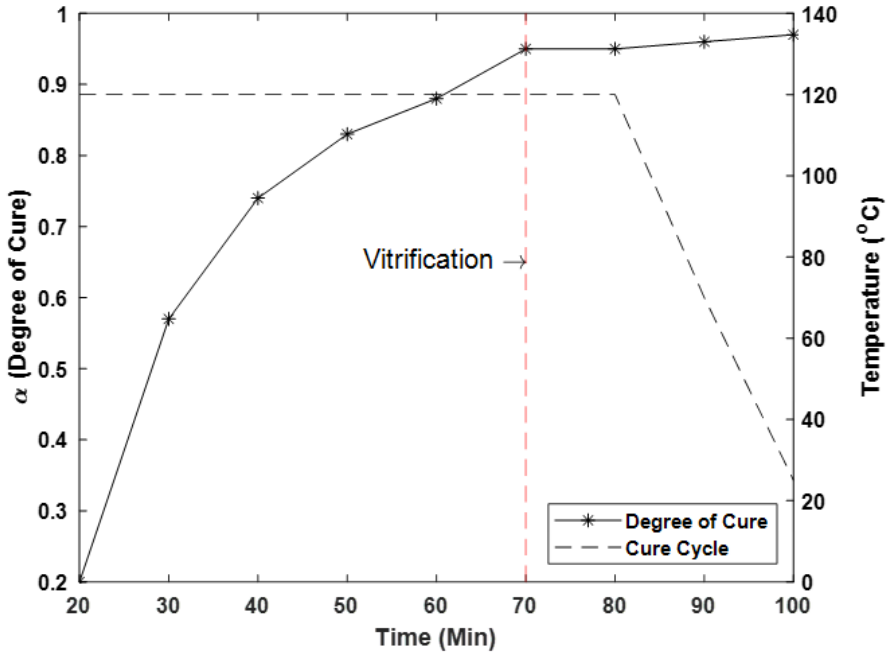

Figure 3.4 Degree of cure curve correlated with autoclave cure profile.

3.2.3. In Situ Strain Data and Analysis

DIC is employed to measure the surface strains of all the layup configurations used in this research. The DIC system used in this work has a minimum in-plane strain measurement capability of 0.005% (50E-6), with a resolution of 10E-6 (*Correlated*

Solutions DIC System Specifications, n.d.). The uncertainty in the displacement and strain measurement depends on several factors including focus, lighting, glare, F-stop, subset size, and the speckle pattern quality (Thai et al., 2019). For the typical experimental conditions and the speckle pattern used here, VIC 3D software computes a mean uncertainty of about 0.00049 pixels for every pixel as shown in Figure 3.2 (c). For the strain measurements in the range of 5E-3, typically observed in this work, this leads to a possible measurement error of around ±1%.

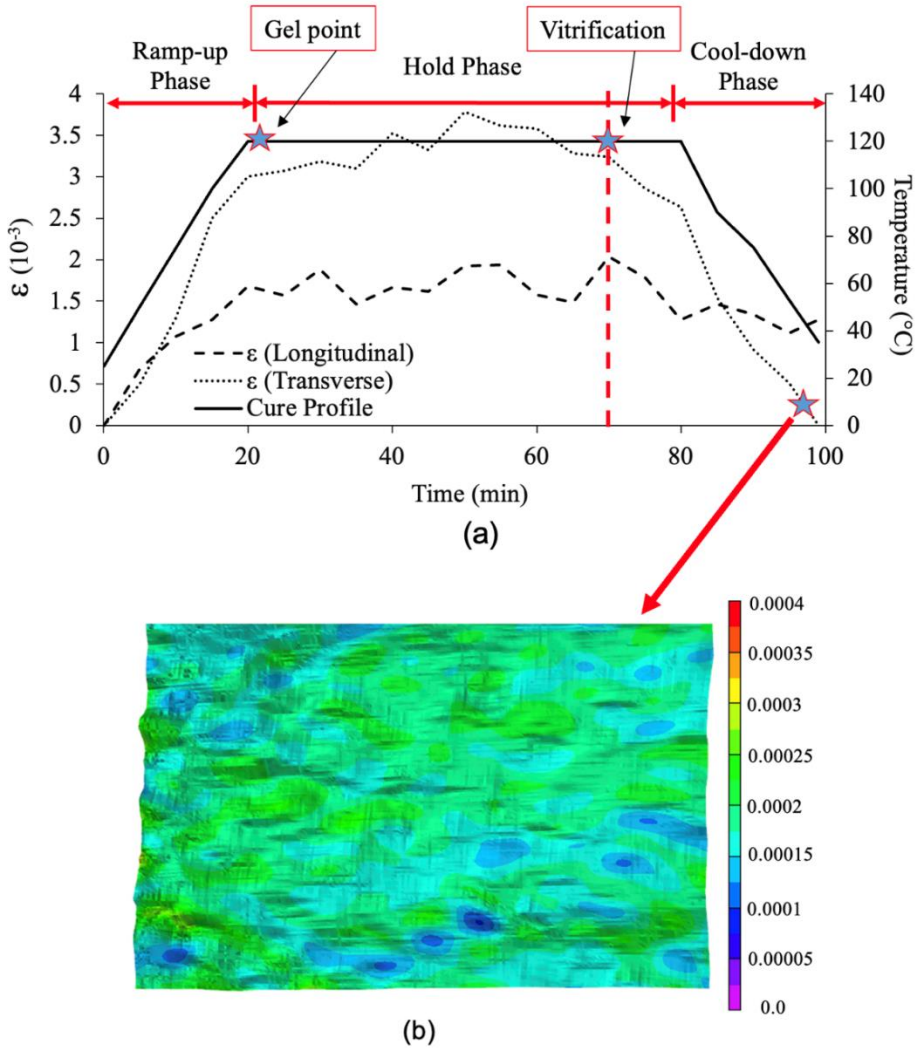

Figure 3.5 (a) Unidirectional single-ply average strains; (b) Longitudinal single-ply strain contour at the end of the cure.

For a unidirectional single-ply laminate, the average surface strains ($\varepsilon_{unidirectional}$) are correlated with the cure cycle of the composite as shown in Figure 3.5 (a). During the ramp-up phase of the cure, the composite expands in both longitudinal and transverse directions, primarily due to the thermal expansion of the matrix and fibers. At this stage, there is no contribution of cure shrinkage. This expansion is higher for transverse than longitudinal direction (3E-3 for T vs 1.7E-3 for L).

In the isothermal stage, cure shrinkage and thermal effects are both responsible for the strain. After vitrification and during cool down, the observed contraction is again primarily due to thermal effects. At the end of the cure, it can be seen that the longitudinal strain (1.2E-3) is higher than the transverse strain (2E-4) because the thermal effects are more prominent in the transverse direction both during ramp-up and cool-down. Figure 3.5 (b) shows the contour plot of the spatial distribution of the transverse strain at the end of the cure.

The measured surface strains ($\varepsilon_{laminate}$) for the other ply configurations in longitudinal and transverse directions are shown in Figure 3.6 and Figure 3.7 respectively. Although strain measurements using DIC are always on the top ply, the ability of the inner plies to restrict the motion of the top ply can be observed in these figures. Particularly three out of the five layup configurations adopted in this research have 0° ply as top ply but the difference in the evolution of strain throughout the hold phase and cool-down phase among these four layups is evident.

Since this paper's focus is on residual stresses, these figures are plotted from the 20 min point to focus on strain and stress build-up from the stress-free point. Also, the reference state of the strain (zero strain) is shifted from the initial state to the stress-free

point as the load transfer goes to zero at the stress-free point at the beginning of the isothermal stage and starts again as the cross-linking of the resin begins during the isothermal stage and continues through the cool-down.

In the longitudinal direction, the strain in $[0/90]_s$ layup increases continuously throughout the cure to 0.91E-3 by the end of the cure. The strain decreases to -1.0E-3 at the end of the cure. The longitudinal strain development in the unsymmetric layups is shown in the lower half of Figure 3.6. A maximum strain of 0.38E-3 is observed for the [30/-30/60/-60] layup and gradually decreases to -0.96E-3 at the end of the cure due to the balanced nature of the layup. For the unsymmetric [0/30/45/90] layup, the strain increases to a maximum during the hold phase and then slightly decreases to 0.05E-3 at the end.

In the transverse direction, as seen in Figure 3.7, for $[0/90]_s$ configuration, a maximum strain of 0.71E-3 is observed and then reduces to -0.13E-3 at the end of the cure. Due to the cross-ply nature of this configuration, the change in strain during cooling is relatively low. In the case of $[0/45]_s$ layup, a maximum strain is observed at the start of the hold-phase and gradually the strain decreases to -1.53E-3 at the end of the cure. For asymmetric layups, [45/-45/45/-45] exhibited negligible changes throughout hold and after cool-down, it reduced to -0.45E-3. For [0/30/45/90] layup with strain gradually decreasing from 1.05E-3 to -1.68E-3 during the hold and cool-down phases of the cure due to distinct ply orientations. Although these are surface strain measurements, any significant movement in the interior plies due to thermomechanical loads during cure as well as residual stresses generated due to the crosslinking of the polymer bonds will be reflected on the surface due to the relatively low thickness of the sample.

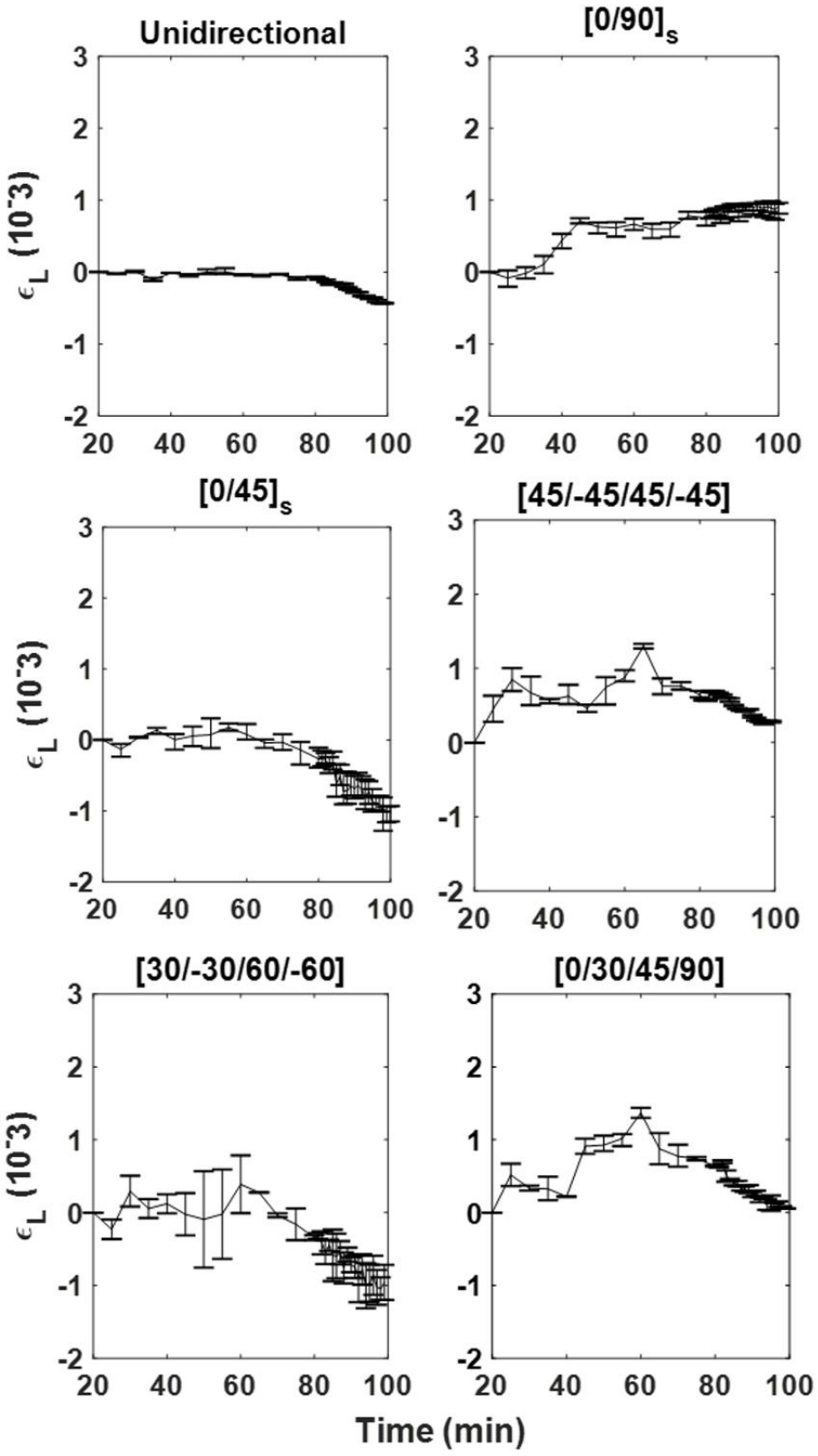

Figure 3.6 Laminate strains in the longitudinal direction.

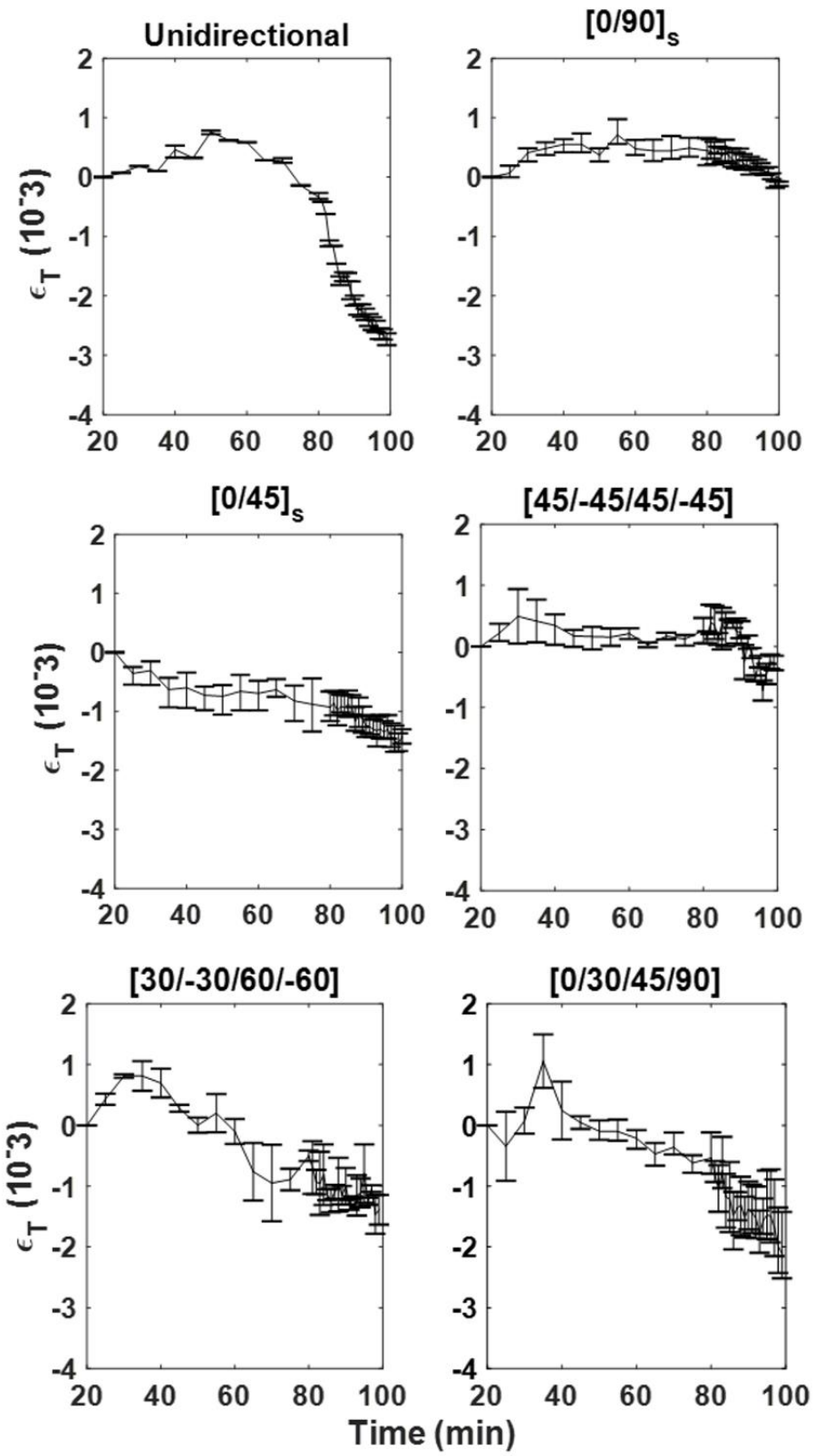

Figure 3.7 Laminate strains in the transverse direction.

3.2.4. Residual Stress Calculation

Residual stresses within a ply are calculated by using the liberated strain approach. This is the strain difference between what a ply is experiencing during the cure and what the ply would experience if it were not constrained by the neighboring plies. The liberated strain is calculated based on the assumption that strain measured at the surface through DIC matches the strain at any point in the interior of a thin plate. The four-ply laminate configuration adopted in this research is considered to be a thin structure. The residual strain for each ply was calculated as a difference between a ply's unidirectional strain and the strain within a laminate transformed by the transformation matrix as shown in Equation 3.2. The angle 'θ' in Equation 3.3 is the angle between the global coordinate x-axis and the direction of the fiber in the considered ply. This residual strain is a function of ply orientation and includes the thermal expansion/contraction as well as cure shrinkage.

$$\{\varepsilon_{residual}(T,t)\}_k = [\tau_k].\{\varepsilon_{laminate}(T,t)\} - \{\varepsilon_{unidirectional}(T,t)\} \tag{3.2}$$

$$\text{Here, } [\tau_k] = \begin{pmatrix} c^2 & s^2 & 2cs \\ s^2 & c^2 & -2cs \\ -cs & cs & c^2 - s^2 \end{pmatrix},\ c = \cos\theta \text{ and } s = \sin\theta \tag{3.3}$$

The temperature-dependent elastic compliance matrix, which is the inverse of the stiffness matrix, can be calculated using the temperature-dependent material properties obtained from DMA, the manufacturer provided Poisson's ratio of 0.35 and in-plane shear modulus of 5 GPa through Equation 3.4. While the material is expected to exhibit linear elasticity for small strains after vitrification, this behavior is also assumed before vitrification from the stress-free point. This assumption enables the computation of a

rough magnitude of residual stress during the hold phase. From the compliance matrix, the stiffness matrix is simply calculated as $[Q]=[S]^{-1}$.

$$[S(T)]=\begin{pmatrix} \frac{1}{E_L(T)} & \frac{-\upsilon_{LT}}{E_L(T)} & 0 \\ \frac{-\upsilon_{LT}}{E_L(T)} & \frac{1}{E_T(T)} & 0 \\ 0 & 0 & \frac{1}{G_{LT}} \end{pmatrix} \tag{3.4}$$

The residual stress for each ply is calculated using the residual strain determined from Equation 3.2 and the temperature-dependent stiffness matrix [Q] of the composite panel as shown in Equation 3.5. The continuous evolution of this residual stress in each ply for all sample configurations can be seen in Figure 3.8 to Figure 3.13(b).

$$\{\sigma_{residual}(T,t)\}_k=[Q(T)]\{\varepsilon_{residual}\}_k \tag{3.5}$$

The residual stresses are calculated using Equation 3.5 for all the layup configurations used in this research and are plotted in Figures 3.8 to 3.13. For $[0/90]_s$ configuration, the change in residual stress is less during the hold-phase until the vitrification point and then rapidly increases to a maximum of 110 MPa and 24.21 MPa in longitudinal and transverse directions for 0° ply as seen in Figure 3.8. This is the highest residual stress observed among the current ply configurations in the longitudinal direction due to the cross-ply nature of the layup. It can also be observed that the highest residual stress for 0° ply is in the longitudinal direction and for 90° ply, it is observed in the transverse direction as the fibers in these respective (parallel-to-the-fibers) directions have high modulus and low thermal expansion coefficient giving rise to the macro stresses during the cool-down (Cowley & Beaumont, 1997).

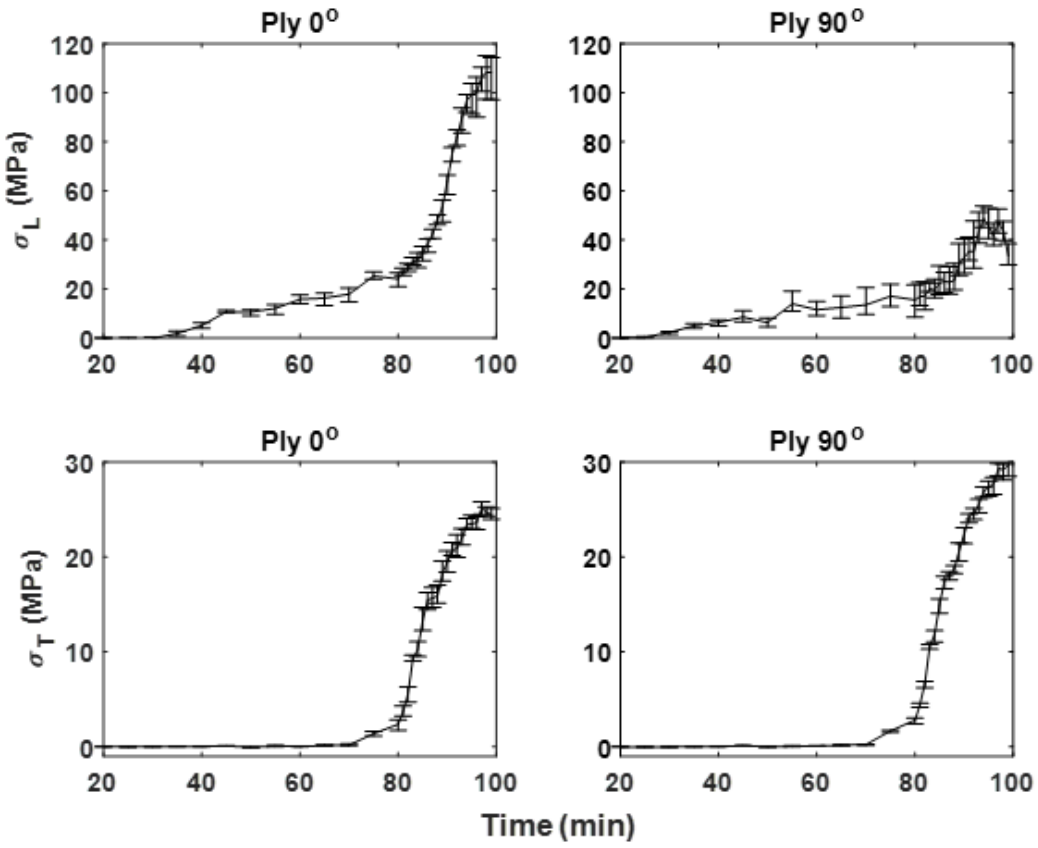

Figure 3.8 Ply stresses in $[0/90]_s$ laminate for the plies oriented in 0^o and 90^o: Plotted against time.

The residual stresses in $[0/45]_s$ along with the rest of the layup configurations follow a similar trend to $[0/90]_s$ changing rapidly after vitrification during the cool-down phase. In the longitudinal direction, 0° ply exhibited compressive stress of -47 MPa, and 45° ply has residual stress of -138 MPa at the end of the cure. In the transverse direction, they exhibit 6.5 MPa and 14.5 MPa respectively. The rate of change in longitudinal residual stress is higher in 45° ply at vitrification compared to 0° ply. This particular difference can only be observed through the continuous evolution of residual stresses as shown in Figure 3.10. In the case of anti-symmetric angle-ply [45/-45/45/-45] configuration, as seen in *Figure 3.11*, 45° ply and -45° ply exhibit similar stresses in both longitudinal and

transverse directions. The coordinate transformation in the stress calculations for this layup resulted in a wider range for the error bars. Note that the error bars for the corresponding longitudinal strain measurements in Figure 3.6 are relatively low.

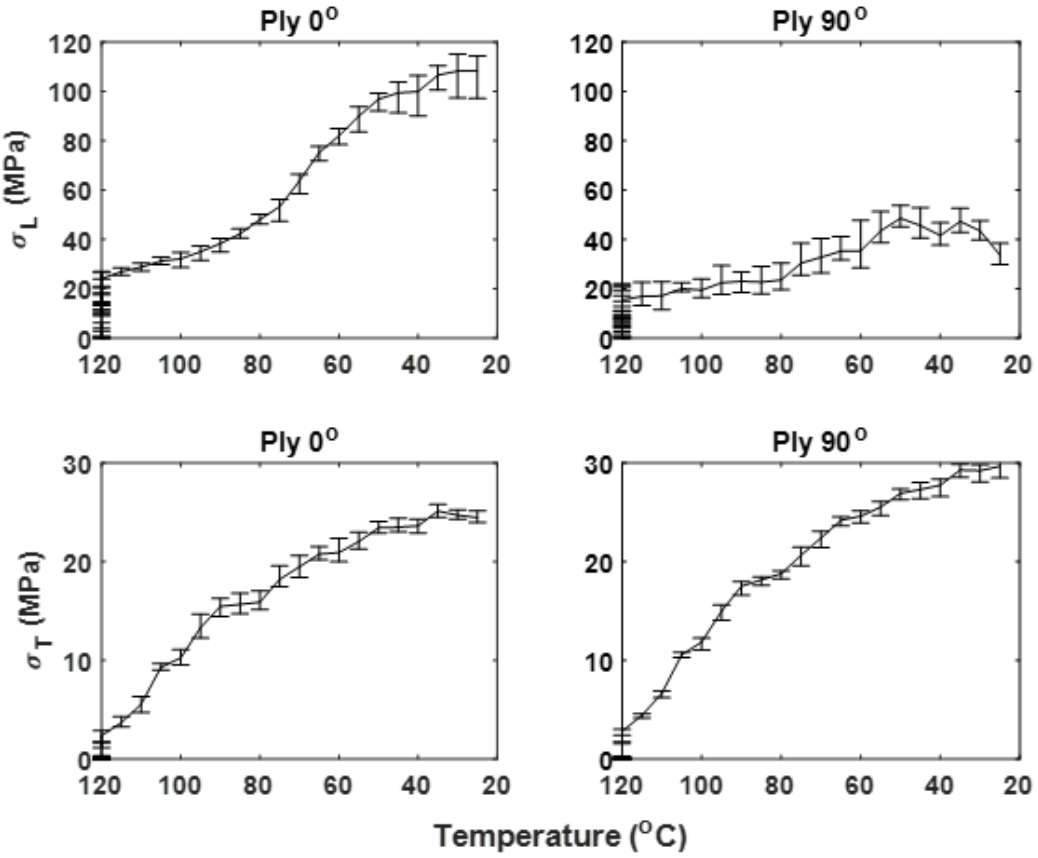

Figure 3.9 Ply stresses in $[0/90]_s$ laminate for the plies oriented in 0^o and 90^o: Plotted against temperature.

For balanced unsymmetrical [30/-30/60/-60] layup configuration, it can be observed from Figure 3.12 that in the longitudinal direction the plies exhibited compressive stresses and in the transverse direction, they are in tension. The rate of evolution of stresses in the longitudinal direction during the hold phase is higher for 60° ply followed by 30° ply, -30° ply, and -60° ply. The ability of 60° to relax stresses during the cool-

down phase is restricted by the -30° ply and -60° ply on top and bottom respectively. The in-situ ability of the current research approach to calculate the residual stress evolution of the internal plies can be clearly observed here. At the end of the cure, 30° ply has maximum longitudinal compressive stress of -71 MPa followed by 60° ply and -30° ply at -65 MPa and -44.5 MPa respectively. The lowest stress is exhibited by -60° ply. In the transverse direction, relatively smaller changes in the evolution of stresses are observed in all four plies in tension. The highest stress of 13.7 MPa was observed for the 60° ply and the lowest stress of 9.7 MPa for the -60° ply.

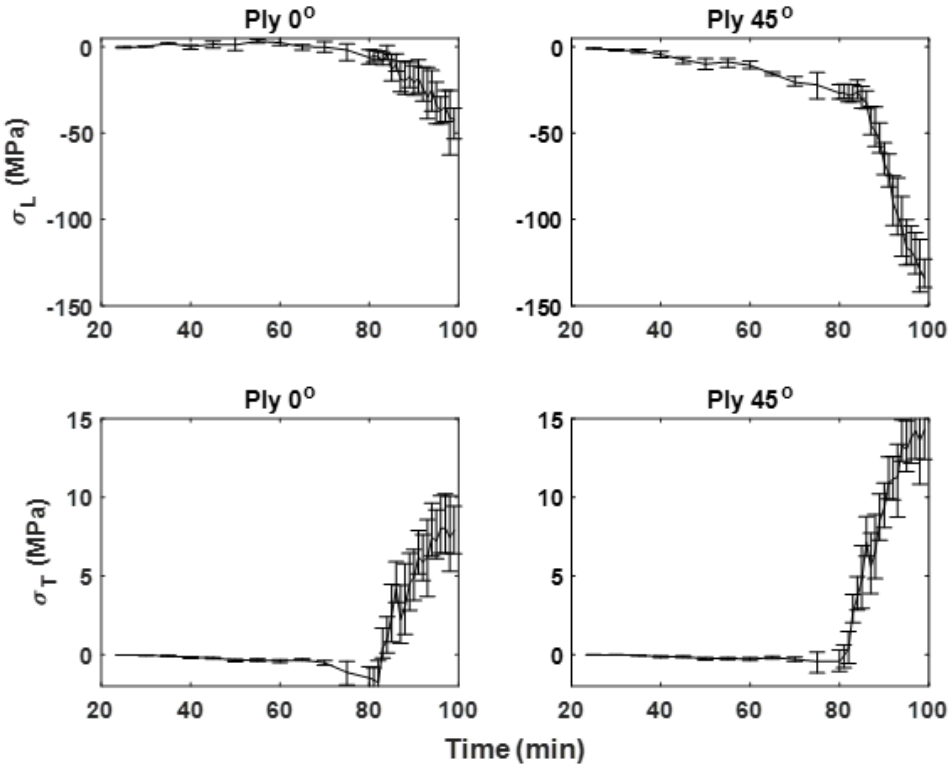

Figure 3.10 Ply stresses in $[0/45]_s$ laminate for the plies oriented in 0^o and 45^o.

In the unsymmetrical [0/30/45/90] layup, while the 0° top ply exhibited 41 MPa stress in tension, both 45° ply and 30° ply exhibit an increase in the rate of compressive residual stress during the hold phase and reached maximum longitudinal compressive stress of -53

MPa and -41 MPa respectively at the end of the cure. The highest longitudinal compressive stress of -132 MPa is observed in 90° ply. This ply also exhibits the highest stress of 17.9 MPa in the transverse direction. As seen in Figure 3.13, the rate of change in residual stresses is low during the hold phase until vitrification followed by a rapid increase after vitrification. A similar trend can be observed for all the layups adopted in this research except some plies are in tension and others are in compression. The cross-ply $[0/90]_s$ layup exhibits the highest residual stress, followed by the rest of the layup configurations.

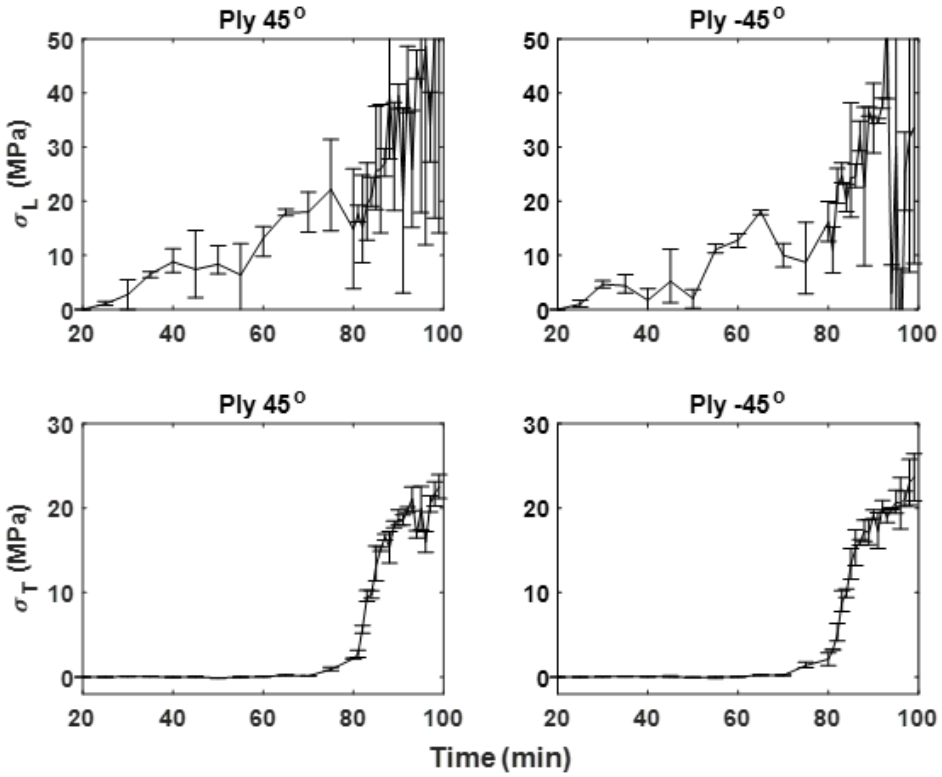

Figure 3.11 Ply stresses in [45/-45/45/-45] laminate for the plies oriented in 45° and -45°.

The amount of stress buildup during the hold and cool-down phase directly corresponds to the strain evolution of that particular layup and associated ply stiffness. For example, in the case of $[0/90]_s$ laminate, there is stress buildup in both 0° and 90°

plies in the longitudinal direction but not in the transverse direction. This is because the strain during the isothermal stage in the longitudinal direction is higher than in the transverse direction for $[0/90]_s$ laminate (as seen in Figures 3.6 and 3.7).

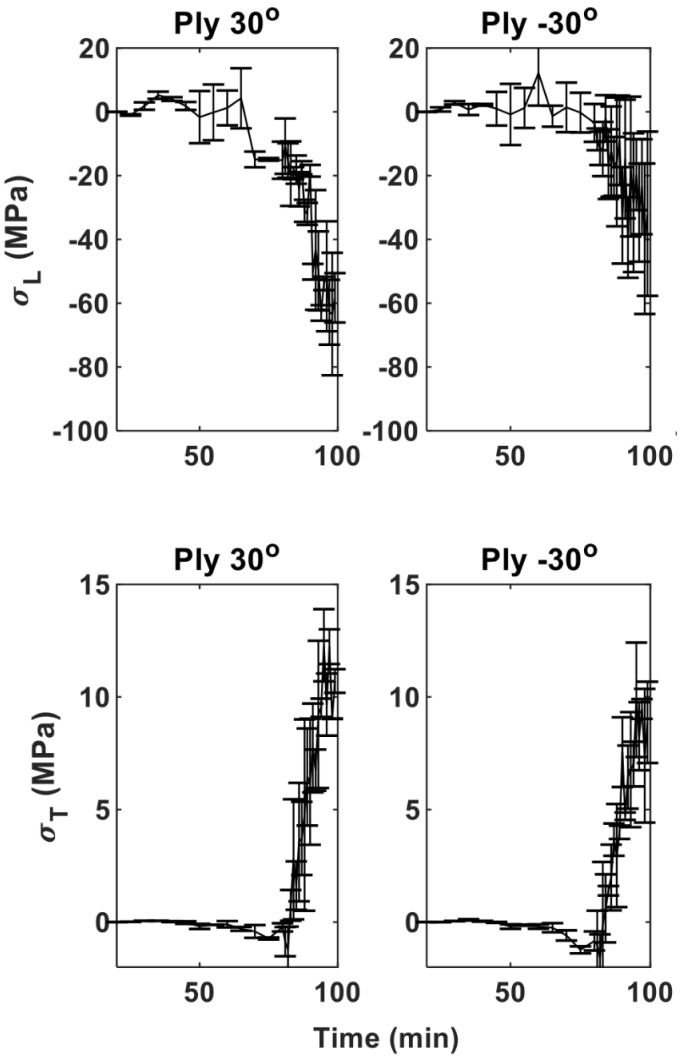

Figure 3.12 (a) Ply stresses in [30/-30/60/-60] laminate for 30,-30 plies in respective orientation.

It is to be noted that the DIC surface strain measurements are made in autoclave conditions i.e. under continuous vacuum and pressure. Hence the stresses measured are also under the same autoclave conditions. When the laminates are removed from the

autoclave after cure, residual stresses in certain asymmetric layups are relaxed by developing the warpage. The effect of the warpage is discussed in Section 3.6.

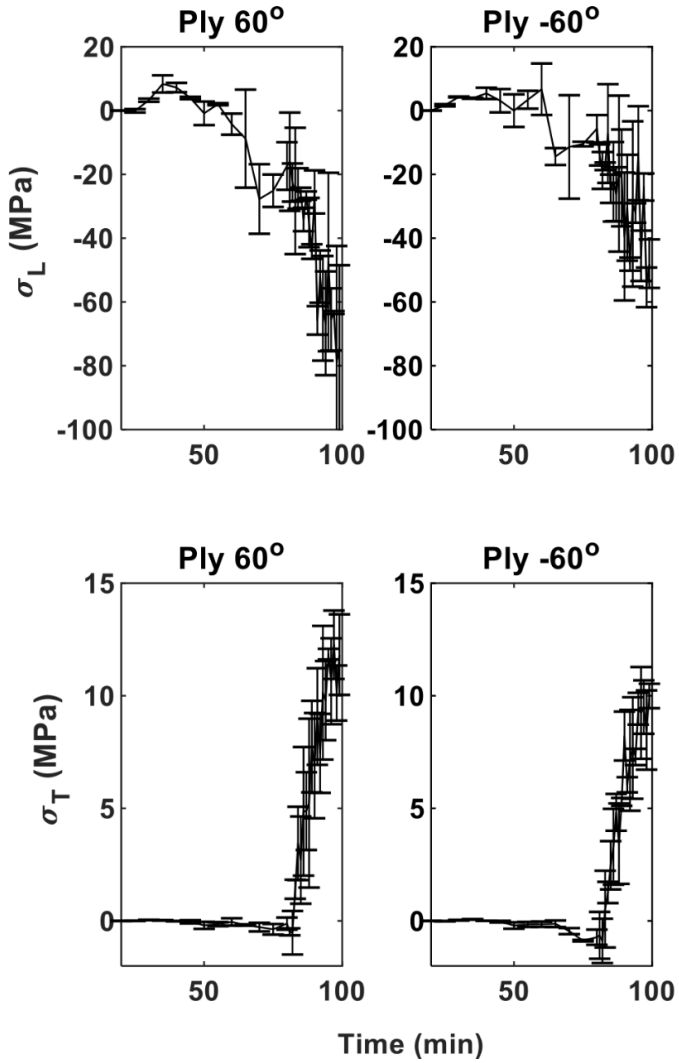

Figure 3.12 (b) Ply stresses in [30/-30/60/-60] laminate for 60,-60 plies.

3.2.5. Laminate Forces and Moments

In this section, the evolution of laminate forces and moments are calculated using the laminate strains obtained from DIC and the temperature-dependent stiffness matrix [Q]. The Classical Lamination Theory (CLT) approach based on the ABD matrix as shown in Equation 3.6 is used for calculating the forces and moments (Jones, 1998). Here, the

strains are under autoclave conditions of vacuum and pressure, and the laminate does not exhibit curvature (κ) under these conditions. Once the laminate is removed from the autoclave, the residual moments at the end of the cure cause warpage in the asymmetric layups.

$$\begin{Bmatrix} N(t,T) \\ M(t,T) \end{Bmatrix} = \begin{bmatrix} A(t,T) & B(t,T) \\ B(t,T) & D(t,T) \end{bmatrix} \begin{Bmatrix} \varepsilon(t,T) \\ \kappa \end{Bmatrix} \tag{3.6}$$

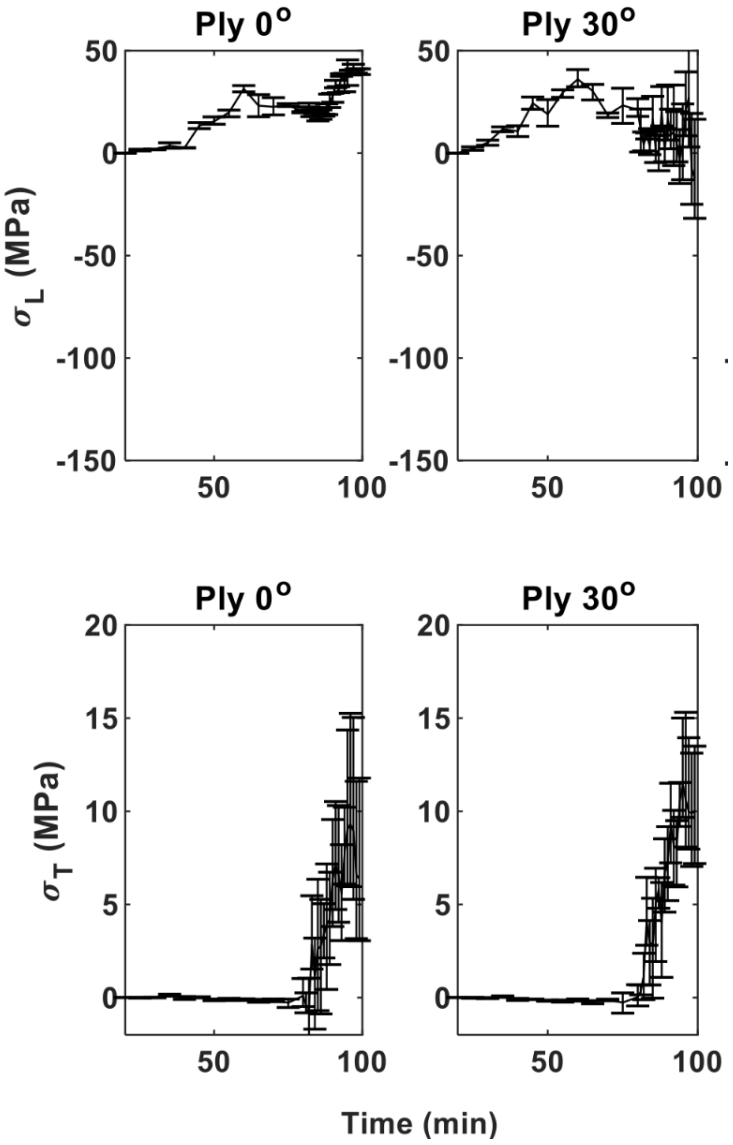

Figure 3.13 (a) Ply stresses in [0/30/45/90] laminate for 0, 30 plies.

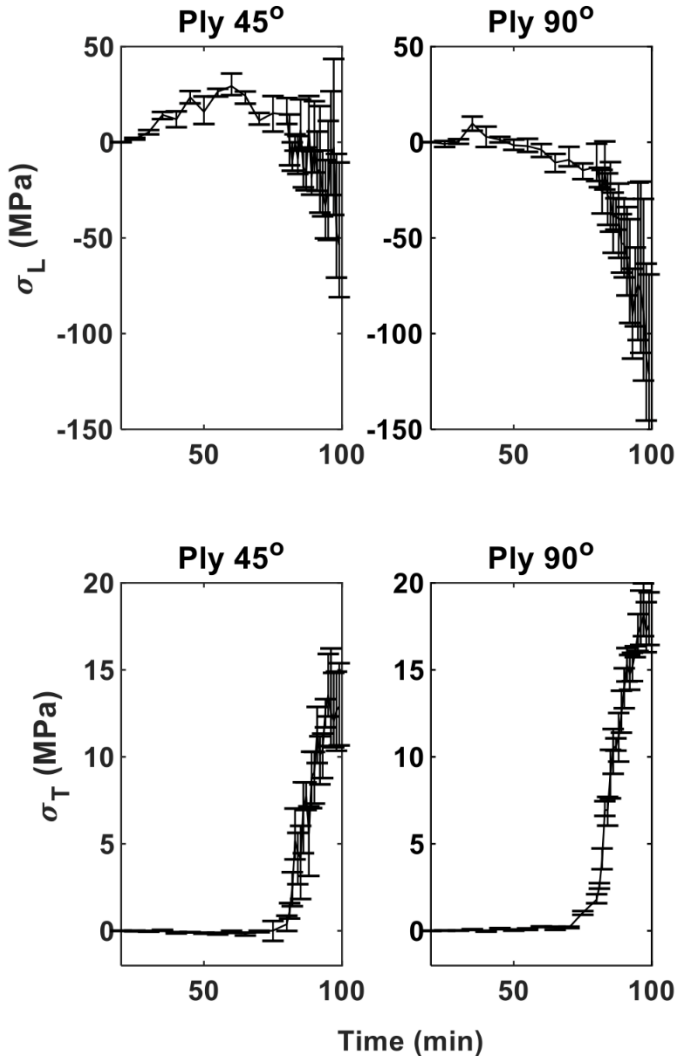

Figure 3.13 (b) Ply stresses in [0/30/45/90] laminate for 45, 90 plies.

The continuous evolution of normal forces N_{xx} and N_{yy} in the laminate are plotted for all sample configurations in Figure 3.14 and Figure 3.15 respectively. The evolution of moments for asymmetric layups is plotted in Figure 3.16. While residual stresses in a laminate are per ply, these normal forces and moments provide an overall effect of those residual stresses on the specimen. It can be seen in Figure 3.14 that the normal force (N_{xx}) for cross-ply $[0/90]_s$ layup is in tension and the rest of the layup configurations are in compression. Similarly, from Figure 3.15, it can

be observed that a maximum compressive normal force (N_{yy}) of -55 KN/m is observed for balanced [30/-30/60/-60] layup and the lowest compressive normal force of approx. 0 KN/m is observed for unidirectional single-ply lamina.

The evolution of moments for asymmetric layups can be seen in Figure 3.16. It can be observed that the maximum overall moment at the end of the cure is observed for balanced unsymmetric [30/-30/60/-60] layup followed by [45/-45/45/-45] layup and [0/30/45/90]. This agrees with the warpage calculations performed on the laminate after removing it from the autoclave vacuum and pressure as seen in Table 3.1.

3.3. Discussion

Residual stresses in carbon fiber composites arise during the manufacturing process due to the thermal and chemical properties of the material. Thermal residual stresses are primarily due to differential CTE when the material is heated and the chemical stresses are due to the matrix shrinkage during cure. The matrix is viscous until it reaches the gel point which is ~120°C for the prepreg used in this research and becomes rubbery after gelation (Chava & Namilae, 2021b).

This is also the point of stress-free temperature where the internal stresses present in the material are liberated (PETHRICK, 2000). For the manufacturer-specified cure cycle, this stress-free point is achieved at 20 min into the cure, and the vitrification point occurs at 70 min into the cure as shown in Figure 3.4. The combination of the glassy matrix after vitrification and the thermal relaxation of the matrix and fibers during the cool-down phase creates residual stresses when the laminate is cooled to ambient temperatures. This can only be observed in the continuous evolution of stresses analyzed in this research.

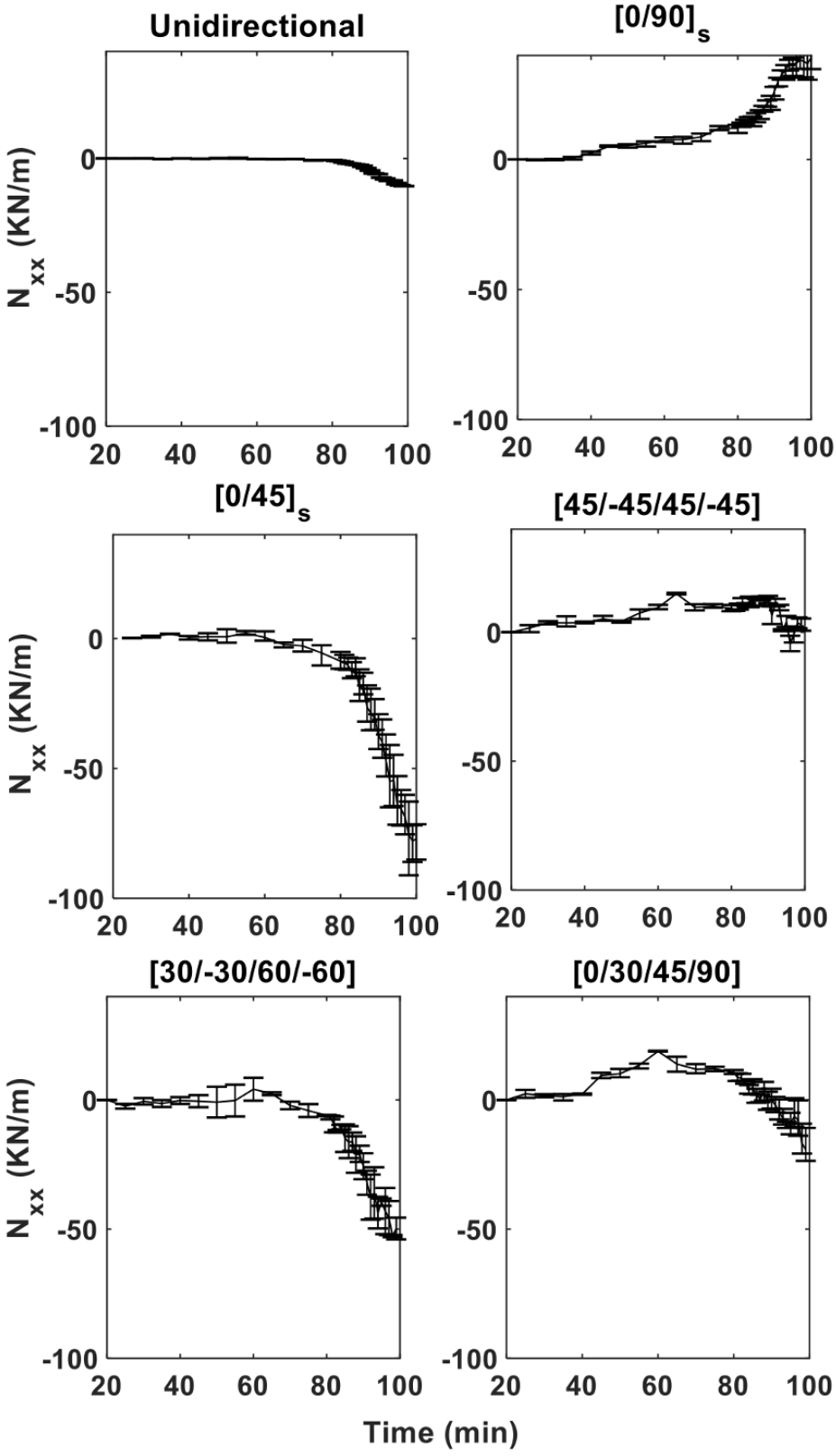

Figure 3.14 Laminate normal forces (N_{xx}).

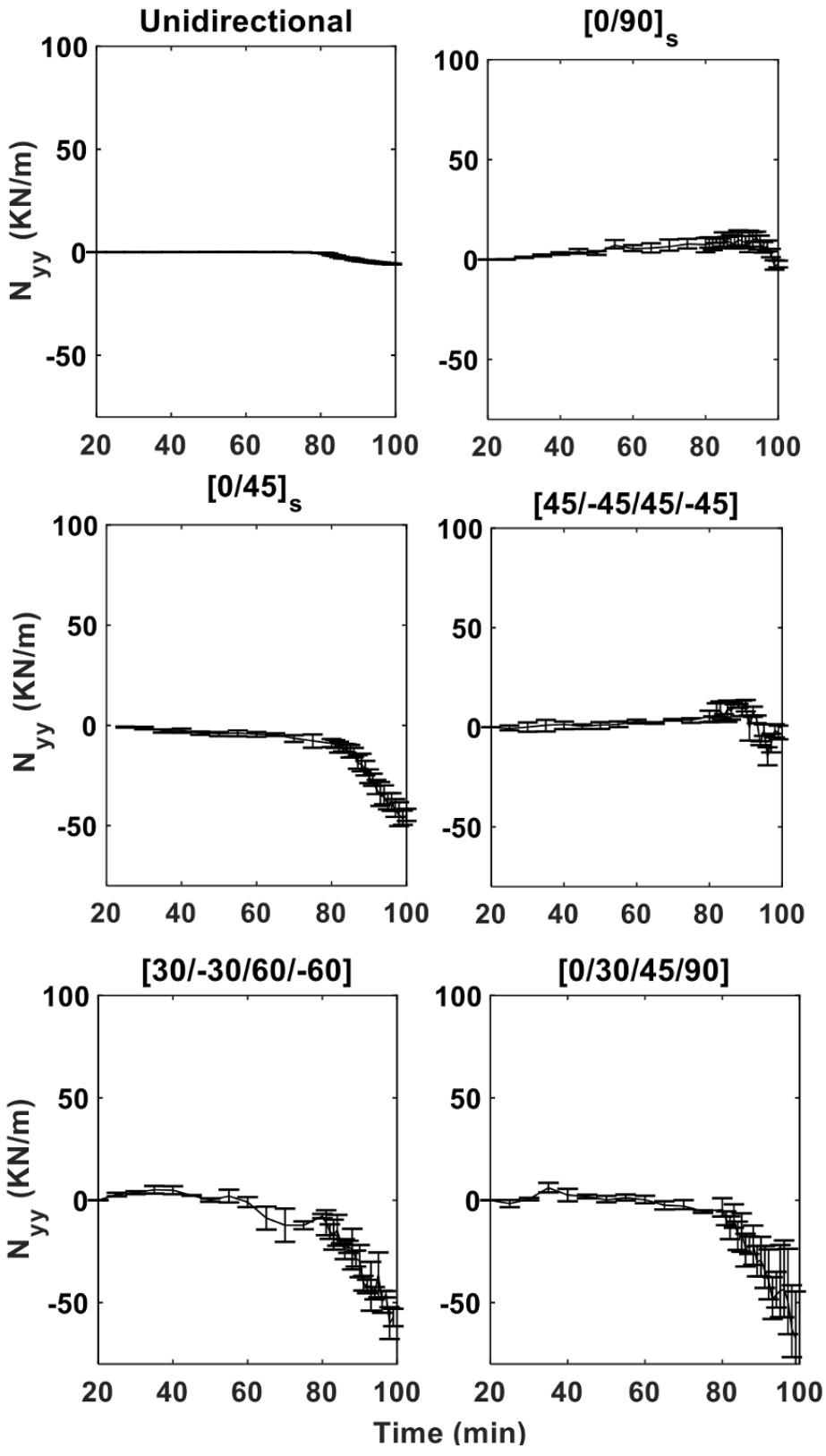

Figure 3.15 Laminate normal forces (N_{yy}).

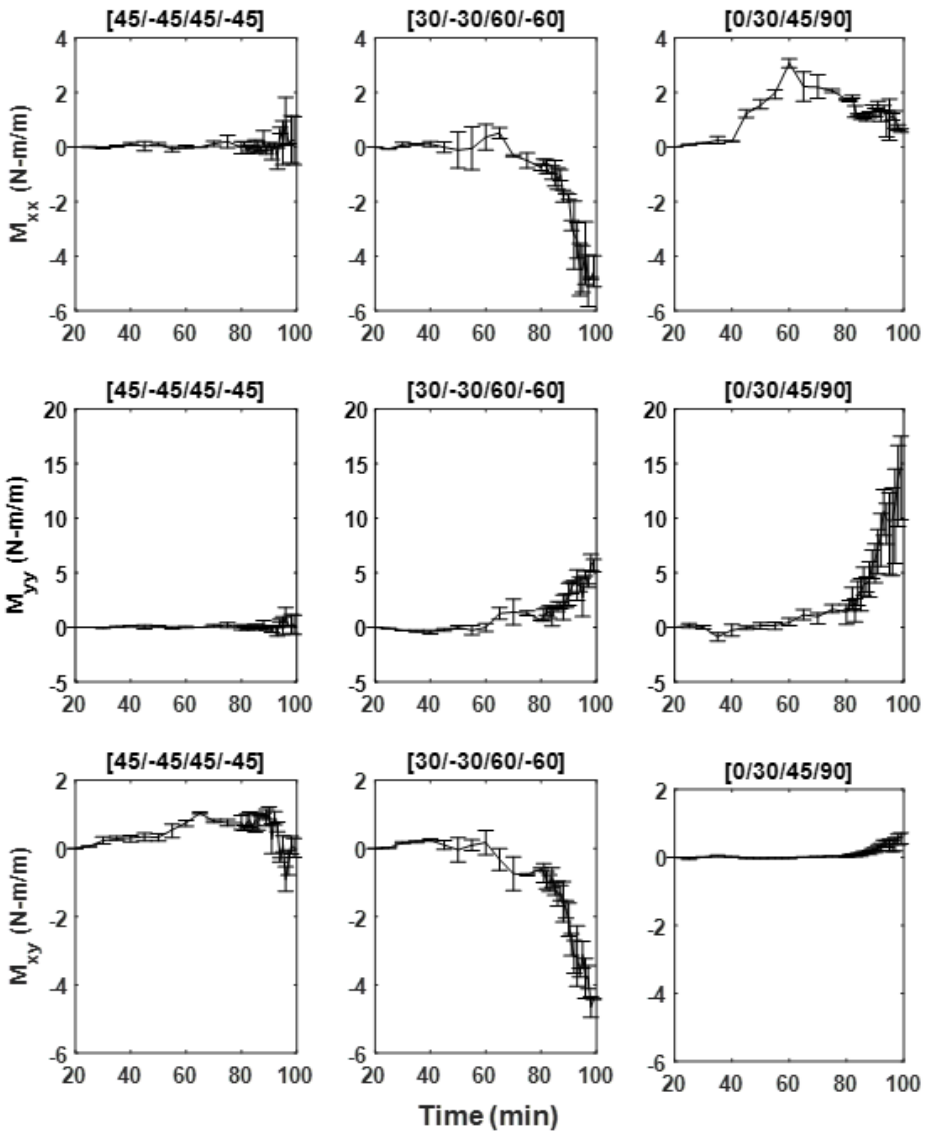

Figure 3.16 Laminate moments for all asymmetric layups.

Table 3.1

Average cup, bow, and twist measurements for asymmetric layups in mm

Configurations	Cup	Bow	Twist	Total Warp (mm)
[45/-45/45/-45]	0	0	0.83	0.83
[30/-30/60/-60]	0.23	0.6	0.63	1.46
[0/30/45/90]	0.53	0	0.18	0.71

It is to be noted that, if the coefficient of thermal expansion of the matrix is larger than the fiber, the resulting thermal stresses have the effect of making the interface strength of the composite look larger than it actually is (Nimmer, 1990). Hence the amount of residual stresses within the ply seen in the above results includes the thermal effect of both matrix and fiber.

Unbalanced residual stresses in asymmetric layups are relaxed by creating a warpage in the laminate after processing. Numerous researchers calculated the residual stresses using the warpage developed in asymmetrical laminates at the end of the cure using CLT. Wisnom et al. (2006) measured temperature-related change in curvature to study residual stresses in asymmetric laminates. Jain and Mai (1996) analyzed the curvature of structural components to estimate residual stresses using modified shell theory. These methods of calculating residual stresses cannot be applied to symmetric laminates due to their inability to develop curvature or warpage. A destructive method is adopted to calculate residual stresses in symmetric laminates by milling layers from one side of the laminate to relieve the residual stresses, thus producing a warped laminate (Cowley & Beaumont, 1997). The measured curvature after milling and CLT is used to calculate the residual stresses. The current method of calculating residual stresses is not only non-destructive but also gives the evolution of the residual stresses throughout the cure for both symmetric and asymmetric laminates. The DIC strain measurements obtained in this research are under autoclave conditions of vacuum and pressure, hence the residual stresses calculated in this research are the actual stresses in the laminates under vacuum bagging. In asymmetric laminates, some of these residual stresses will be relaxed to create a warpage after processing.

Warpage in flat laminates is calculated as a combination of cup, bow, and twist deviations from its initial flatness as shown in Figure 3.17. The angle ply nature of [45/-45/45/-45] layup contributes only to twist without any cup or bow warp. In the case of balanced [30/-30/60/-60] layup, while the difference in alternating orientations of ±30° and ±60° plies creates bow, the angled ply layup leads to the twist deformation. The combination of both bow and twist in this balanced layup creates small cup warpage. The absence of any negative direction ply eliminates bow warp in [0/30/45/90] layup. While the 30° and 45° plies in the middle contribute to twist, the 0° and 90° plies on top and bottom contribute to the cupping effect. The average warpage for the asymmetric layup configurations adopted in this research can be seen in Table 3.1. Comparing Table 3.1 and residual moments in Figure 3.16, it is clear that the relaxation of residual moments leads to warpage in asymmetric layups after removing from vacuum conditions.

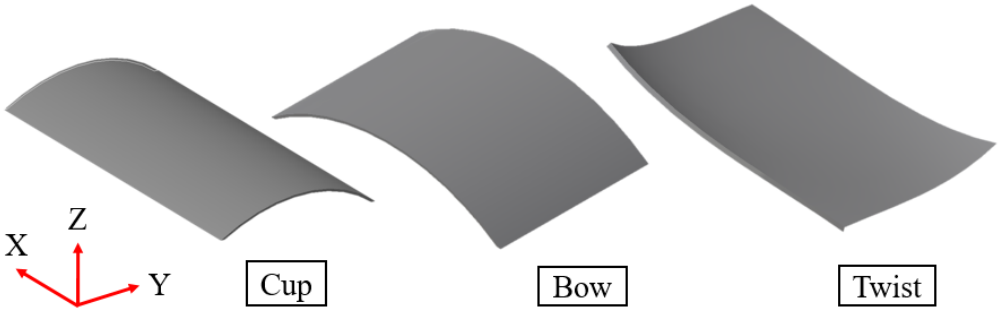

Figure 3.17 Warpage shown as cup, bow, and twist of the laminate.

3.4. Summary

The growing use of advanced composite laminates in recent years has focused attention on processing-induced defects such as delaminations and matrix cracking which are caused by residual stresses. In the current work, the continuous evolution of residual stresses during composite processing is investigated by combining the dimensional

changes measured using a novel in-situ experimental approach with temperature-dependent moduli obtained from DMA. The main research findings are summarized below:

A. The experimental approach developed in this research is effective in calculating the residual stresses throughout the cure for both symmetric and asymmetric layups. The pattern of residual stresses developed after curing in all the layup configurations correlates with knowledge from literature.

B. The combination of strain evolution and increase in modulus during cool down lead to a rapid increase in the residual stresses after vitrification. This is observed for all the layups considered in this research.

C. Among the symmetric layups, $[0/90]_s$ cross-ply layup exhibited maximum residual stress of 110 MPa in the longitudinal direction followed by $[0/45]_s$.

D. Among the asymmetric layups, balanced unsymmetric [30/-30/60/-60] layup exhibited maximum residual stress followed by [45/-45/45/-45] and [0/30/45/90] layups.

E. Warpage is developed in all three asymmetrical layups after processing. Higher residual stresses resulted in higher average warpage with the balanced unsymmetric [30/-30/60/-60] layup exhibiting an average warp of 1.46 mm.

4. Residual Stress Reduction during Manufacturing

Residual stresses are detrimental to composite structures as they induce processing defects like debonding, delamination, and matrix cracking which significantly decrease their load-bearing capability. In the present chapter, residual stresses during manufacturing are reduced using two different approaches. A cure cycle modification approach through cure interruption and interfacial modification approach by growing ZnO nanorods.

The novel in-situ experimental approach developed in Chapter 3 is utilized to analyze the effect of the cure cycle modification on residual stress evolution during processing. It was found that the modified cure cycle comprising abrupt cooling after gelation reduces the residual stresses. This continuous evolution of residual stresses helps understand the mechanisms by which residual stresses decrease due to the changes in the cure cycle. Variation in residual stresses due to the symmetry and angles of the plies is studied by analyzing and comparing different layups. The changes in the tensile strength of the composite due to residual stress reduction are also investigated.

An exploratory study is conducted to evaluate how interface modification changes residual stress evolution. The interface between the plies of a laminate is modified by growing ZnO nanorods on the surface of these plies before cure. Preliminary results show that this approach is effective in reducing residual stresses.

4.1. Experimental Procedure for Cure Cycle Modification

4.1.1. Experimental Setup

Unidirectional carbon fiber prepreg procured from Fibre Glast Corporation is pre-impregnated with an epoxy resin system of density 1.2 g/cc and has a fabric areal weight

of 139 gsm. The manufacturer recommended curing temperature is 120°C with one hour hold time. The in-situ experimental method described in section 3.1 is used here. The setup is shown in Figure 4.1 (a). The VIC-3D Real-Time DIC System cameras from Correlated Solutions Inc., are set up pointing at the composite layup through the viewport of the autoclave. A random high contrast speckle pattern was sprayed on the surface ply of the specimen using high-temperature spray paint as shown in Figure 4.1 (b). Surface ply deformations and strains during the composite processing are obtained by extracting full-field information from the speckle pattern. The cure cycle from the manufacturer and the modified cure cycle is converted into a step-by-step recipe, which is then programmed into composite processing control (CPC) of the autoclave computer.

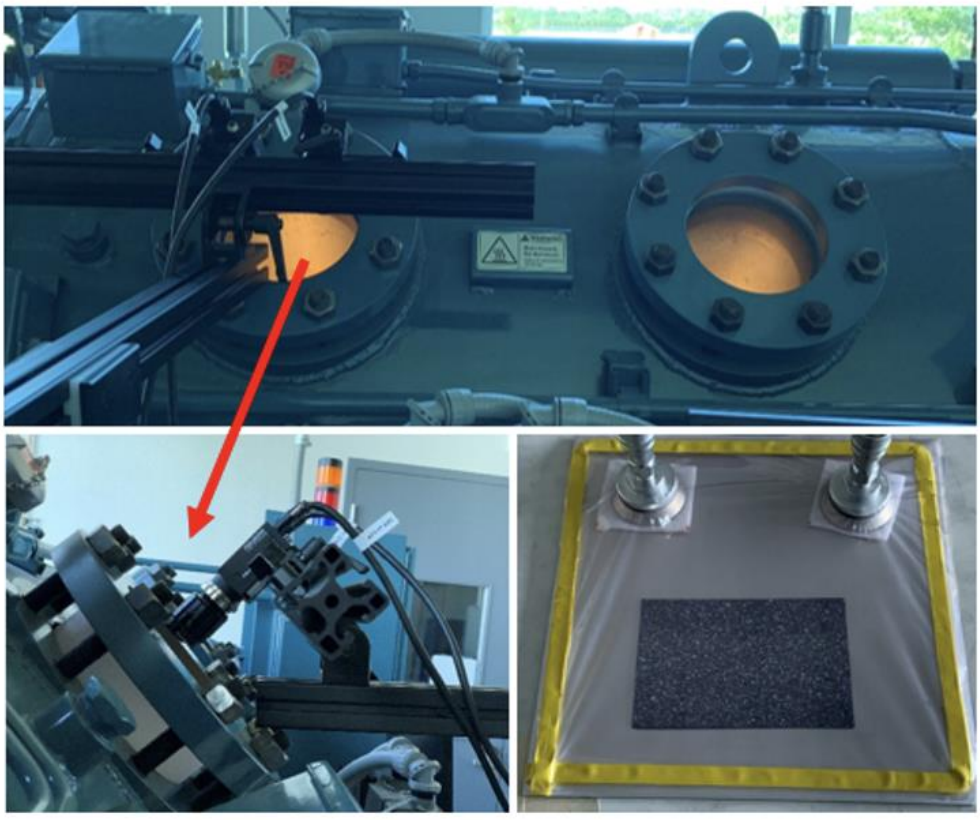

(a) (b)

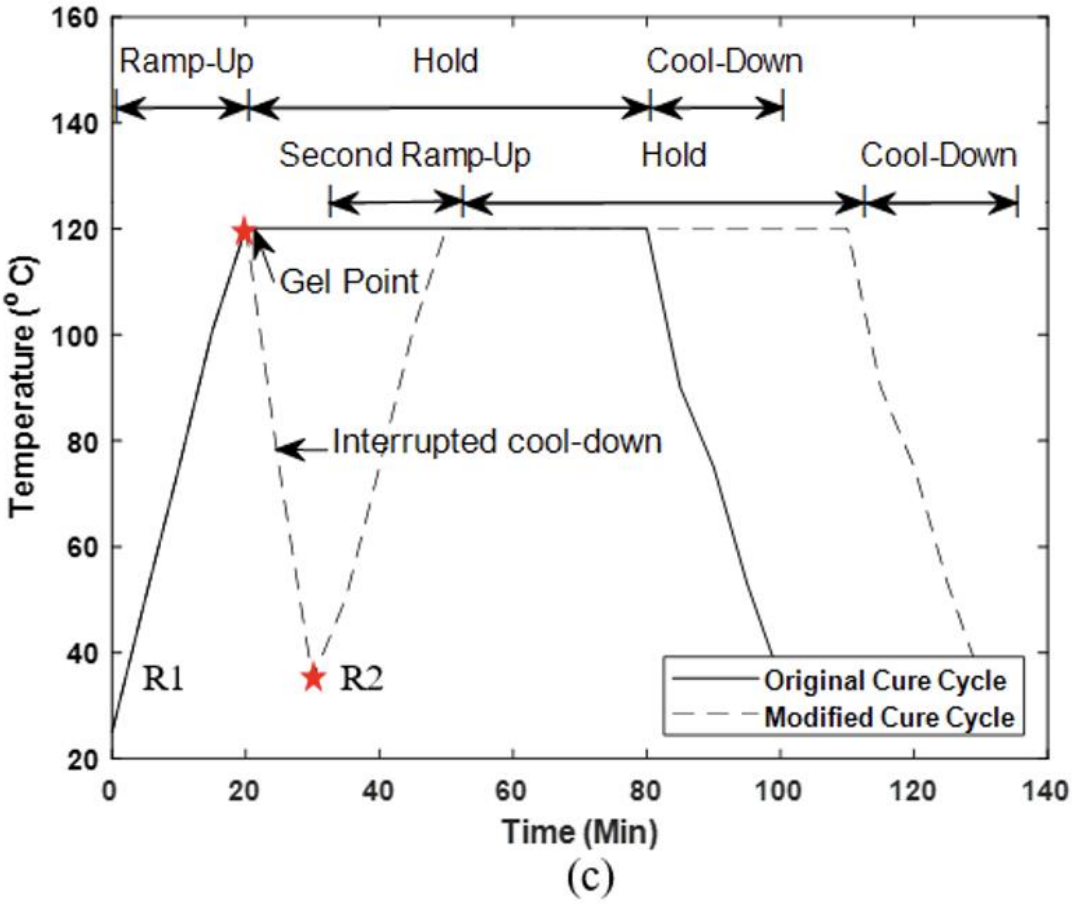

Figure 4.1 (a) Autoclave with DIC; (b) Sample with speckles; (c) Cure cycle comparison.

The modified cure cycle consists of controlled abrupt cooling as the matrix reaches the gel point at ~120 °C. This typically happens 20 minutes into the cure. The cooling operation is performed by relocating the sample from the autoclave to a walk-in freezer. All the samples consist of four-ply layups and are of similar weight. The samples reach room temperature in 12 minutes to achieve an average cooling rate of -8°C/min. FLIR A615 thermal machine vision camera was used for thermal analysis of the specimen during the abrupt cooldown process. After cooling, the sample is moved back to the

autoclave to the same (pre-marked) location. The rest of the cure from 20 min to 100 min is performed as shown in Figure 4.2.

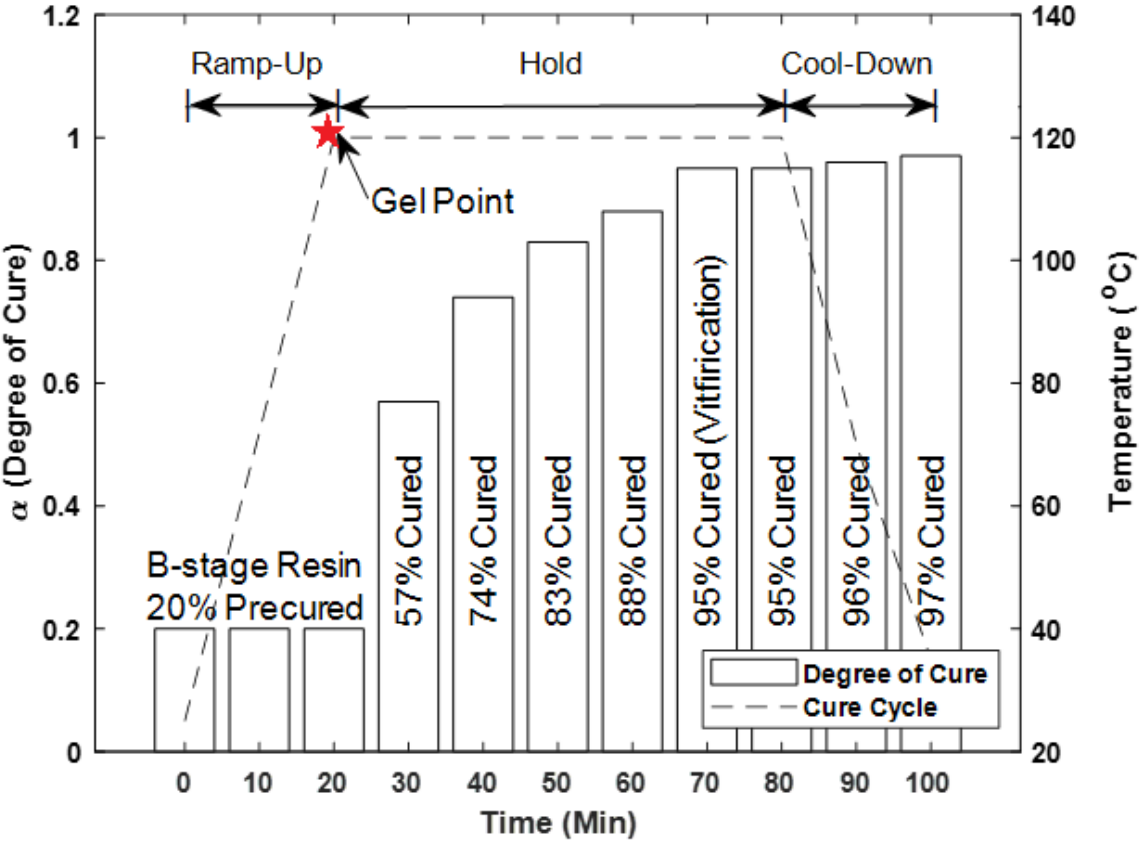

Figure 4.2 Original cure cycle and the corresponding degree of cure.

4.1.2. Thermal Characterization

Temperature-dependent dynamic elastic moduli of the composite material are characterized through dynamic mechanical analysis (DMA) by DMA8000 procured from PerkinElmer. A three-point bend fixture is used for the mechanical analysis of a small unidirectional four-ply sample with dimensions 50 mm × 7.5 mm as it can eliminate the possibility of potential clamping errors. Temperature ranges from 30°C to 120°C were considered based on the manufacturer's recommended cure cycle for the prepreg along

with the maximum displacement of 0.01 mm at 1Hz frequency for the DMA. The cure characteristics of the epoxy are analyzed using a DSC-3 differential scanning calorimetry (DSC) from Mettler Toledo.

4.1.3. Mechanical and Microstructural Characterization

Composite plates of dimensions 101.6 mm x152.4 mm (4 inch x 6 inch) were prepared for fabrication using four plies of unidirectional carbon fiber prepreg in two symmetric orientations of $[0/90]_s$, $[0/45]_s$, and three asymmetric orientations of [30/-30/60/-60], [0/30/45/90] and [45/-45/45/-45]. Another set of specimens for tensile testing with dimensions 25.4 mm x 152.4 mm (1-inch x 6-inch) were prepared for all five layups from the original samples using a composite water jet cutter.

Mechanical tests for assessing the first-ply failure load and stress at failure are executed using an MTS tensile machine. The first-ply failure test is commonly used to analyze the effect of residual stresses present in the laminate (Crasto & Kim, 1993; Kam & Sher, 1995; R. Y. Kim & Hahn, 1979).

The tensile strength is quantified through acoustic emission of the first crack, hence the term ‘first-ply failure’. The acoustic emission in this work is captured using an omnidirectional microphone connected to a smartphone running a decibel meter application. Fracture analysis (FA) is performed for all the laminates cross-sections after tensile testing using FEI Quanta 650, scanning electron microscope from Thermo Fisher Scientific Co. The results from the fracture analysis clearly show the difference in the fracture between regularly cured and interrupted cure samples.

4.2. Results and Discussion for Modified Cure Cycle

4.2.1. DIC Data Analysis

The continuous strain evolution in the longitudinal direction is shown in Figure 4.3. For the $[0/90]_s$ layup, the strain gradually increases during the cure to reach a maximum strain of 2.1 µm/mm at the end of the cure. For the $[0/45]_s$ layup, a maximum strain of 3.8 µm/mm is observed at the start of the isothermal stage and the strain rapidly decreases after resin vitrification (70 min) to 2.9 µm/mm at the end of the cure. For the anti-symmetric angle ply [45/-45/45/-45] layup, only a small change in strain can be observed throughout the cure. A maximum strain of 4.2 µm/mm is observed for the [30/-30/60/-60] layup and the strain gradually decrease to 2.7 µm/mm at the end of the cure due to the balanced nature of the layup. For the unsymmetric [0/30/45/90] layup, a rapid decrease in strain can be observed after vitrification due to distinct ply orientations.

The strain in the transverse direction for [0/90]s cross-ply layup increases slightly from the start of the isothermal stage to the end of the cure, as shown in Figure 4.4. The angled effect of the 45^o ply in [0/45]s layup resulted in a max strain of 5.1 µm/mm which later reduced to 3.5 µm/mm at the end of the cure. The [45/-45/45/-45] layup exhibits a constant strain in the isothermal stage until vitrification and the strain decreases after that during the cool-down.

A maximum transverse strain of 5.3 µm/mm is observed for [30/-30/60/-60] layup which gradually reduced to 2.9 µm/mm towards the end of the cure. In the case of unsymmetric [0/30/45/90] layup, the transverse strain increases initially in the isothermal stage but then reduces continuously to 1.3 µm/mm at the end due to the combination of dissimilar ply orientations in the same layup. In general, for unidirectional carbon fiber prepregs, the transverse thermal expansion is higher than in the longitudinal direction (Bowles & Tompkins, 1989). This can be observed in the above results as well.

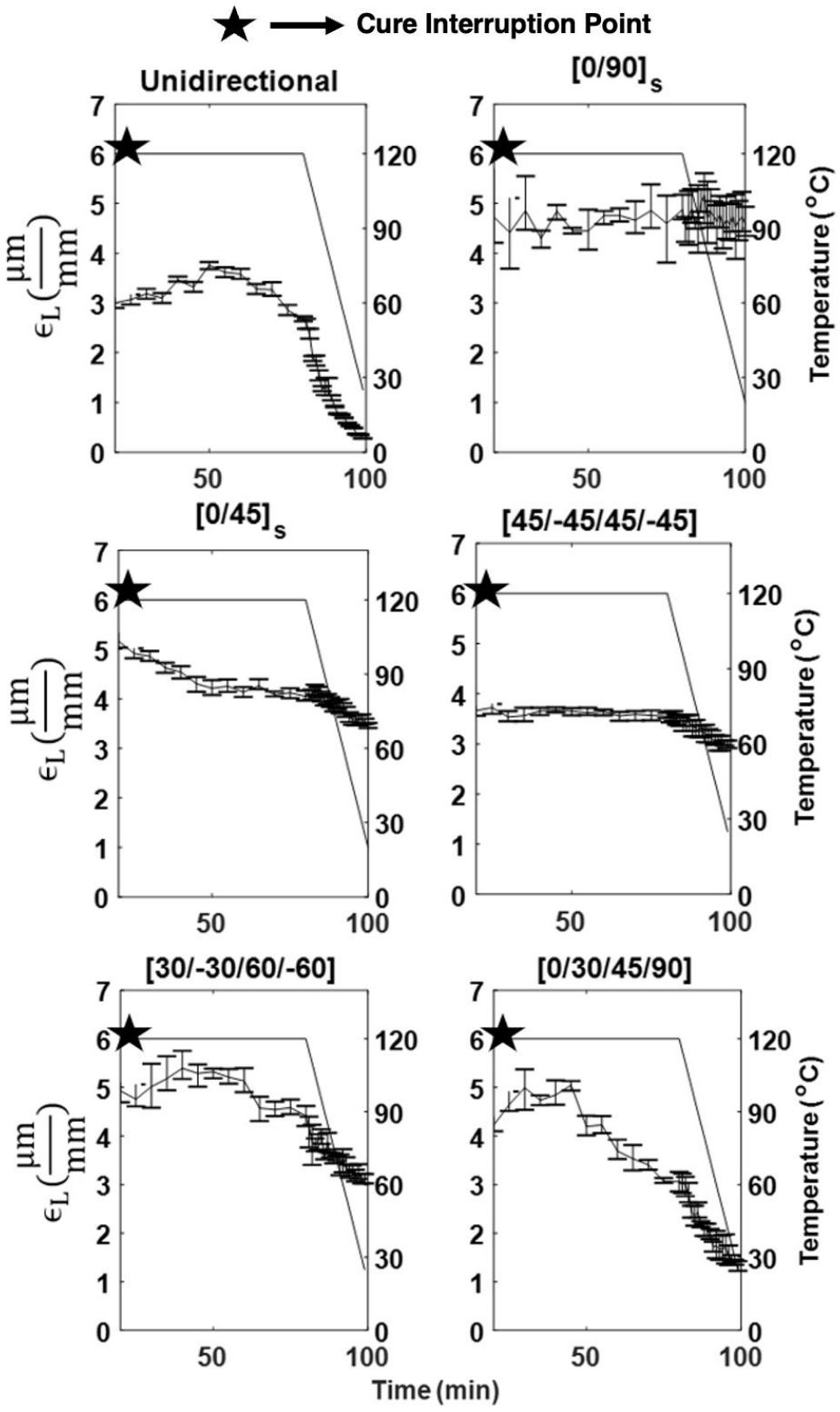

Figure 4.3 In-situ interrupted strains in the longitudinal direction.

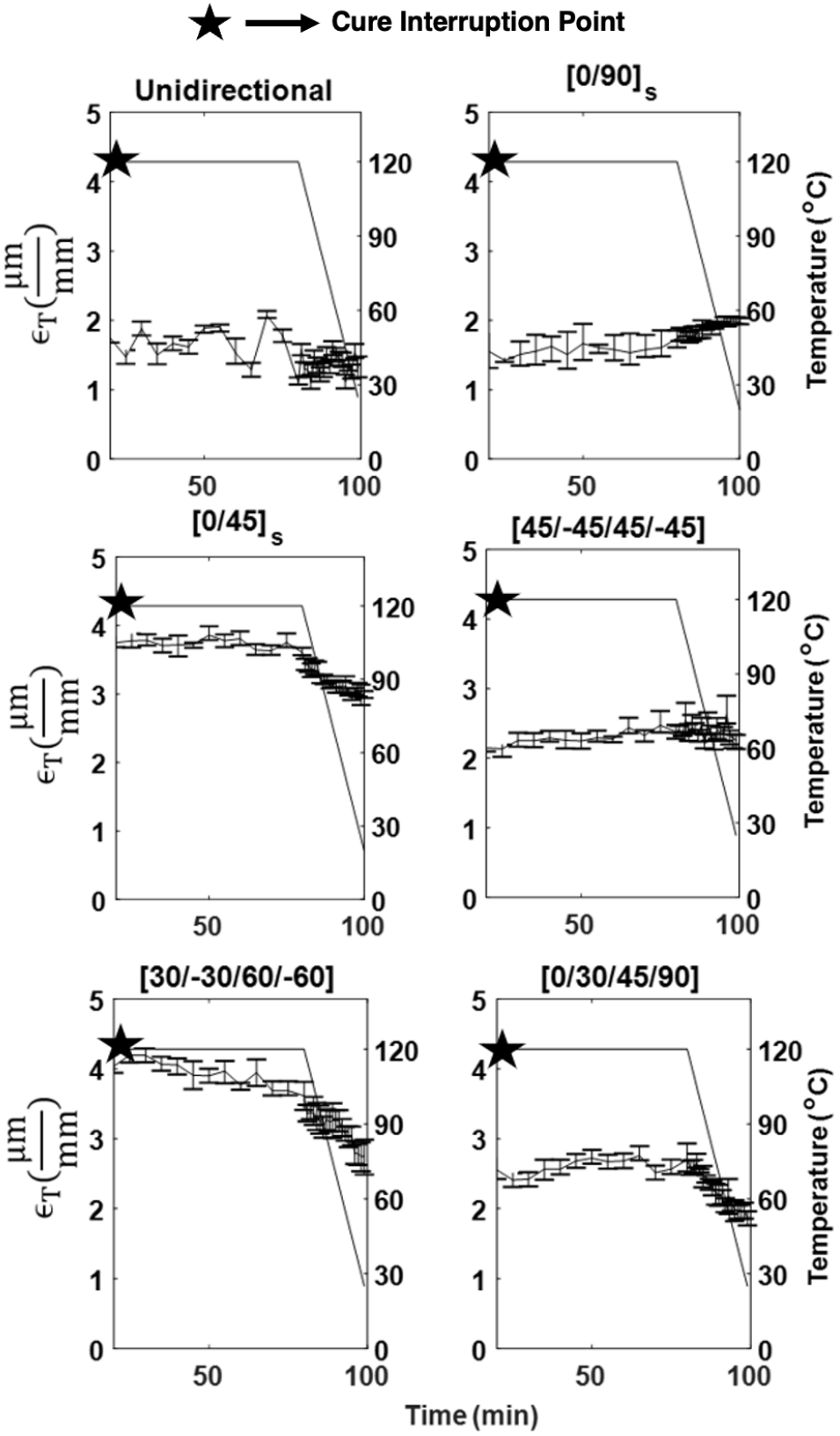

Figure 4.4 In-situ interrupted strains in the transverse direction.

4.2.2. Residual Stress Calculation

The continuous evolution of residual stresses within each ply of the laminate throughout the cure is calculated using the liberated strain approach developed by the authors (Chava & Namilae, 2021a). The temperature and time-dependent residual stress during composite processing for each ply are calculated using the residual strain determined from DIC analysis and the temperature-dependent stiffness matrix [Q] as shown in Equation 4.2.

$$\{\sigma_{residual}(T,t)\}_k = [Q(T)]\{\varepsilon_{residual}\}_k \tag{4.2}$$

The stiffness matrix is calculated using the temperature-dependent material properties obtained from DMA, the manufacturer provided Poisson's ratio of 0.35 and in-plane shear modulus of 5 GPa. While the strain is considered to be identical to the surface strain for the four plies, the residual stresses are dependent on ply stiffness and are calculated separately for each orientation.

The residual stresses calculated for the laminates cured using the modified cure profile are compared with the stresses calculated for the manufacturer's recommended cure cycle in Figure 4.5-Figure 4.9. These results are an average of four tests for each layup with the solid line representing the regular cure and the broken line representing the modified cure. The regular cure cycle is 100 min long and the modified cure cycle is 130 min. However, the residual stresses are compared from the start of the hold phase between both the cure cycles which is 20 min point for the regular cure cycle and 50 min point for the modified cure cycle. Hence the total time from the start of the hold phase till the end is 80 min long in both cure cycles as seen in Figure 4.5-Figure 4.9.

For the cross-ply $[0/90]_s$ laminate as shown in Figure 4.5, the residual stresses are lower for the modified cure approach in both longitudinal and transverse directions. Stresses in the transverse direction exhibited a higher relaxation after vitrification compared to longitudinal. This layup exhibited the highest residual stress among all the ply layups considered.

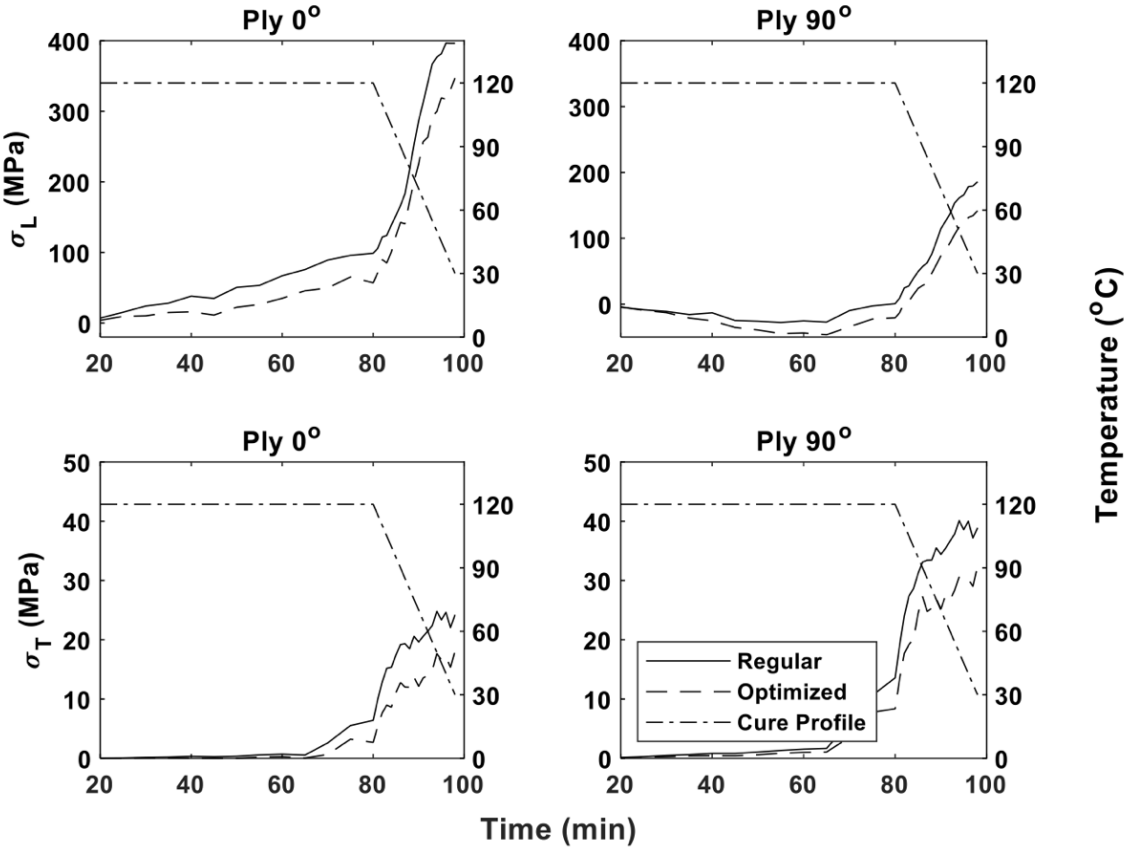

Figure 4.5 Residual stresses comparison for [0/90]s laminate.

The residual stresses evolution for $[0/45]_s$ laminate is shown in Figure 4.6. For this layup in the longitudinal direction, both plies experienced slightly lower residual stresses from the start of the isothermal stage with 45° ply experiencing a reduction from 198 MPa to 180 MPa at the end of the cure for the modified cure. In the transverse direction,

the plies did not experience any major change until vitrification but after vitrification and during cool-down both 0° ply and 45° ply experienced a decrease of about 2MPa at the end of the cure.

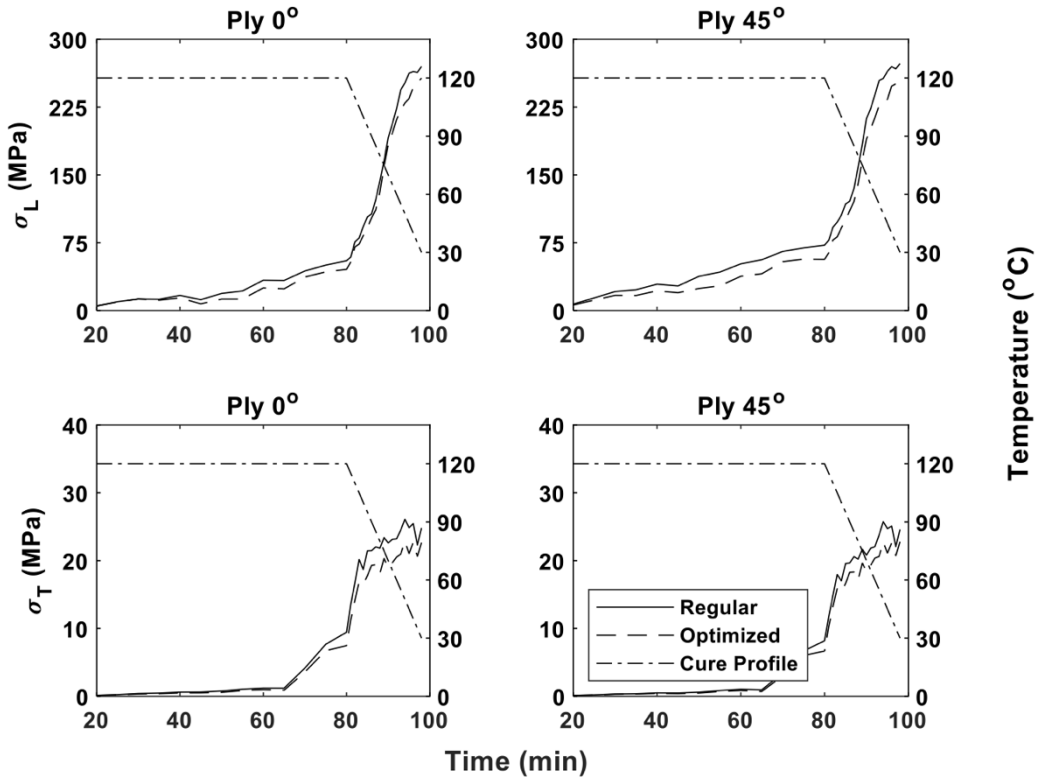

Figure 4.6 Residual stresses comparison for $[0/45]_s$ laminate.

The residual stresses evolution for the [45/-45/45/-45] laminate is shown in Figure 4.7. In this layup, the 45° ply in longitudinal direction experienced lower stresses from the isothermal stage and rapidly increased towards the end of the cool-down stage. In the transverse direction, the difference is observed during the cool-down stage only. The -45° ply, exhibits a small change in stresses between regular and modified cures until vitrification, but after vitrification, the difference gradually increased to a maximum of 10 MPa and 3 MPa in the longitudinal and the transverse directions, respectively.

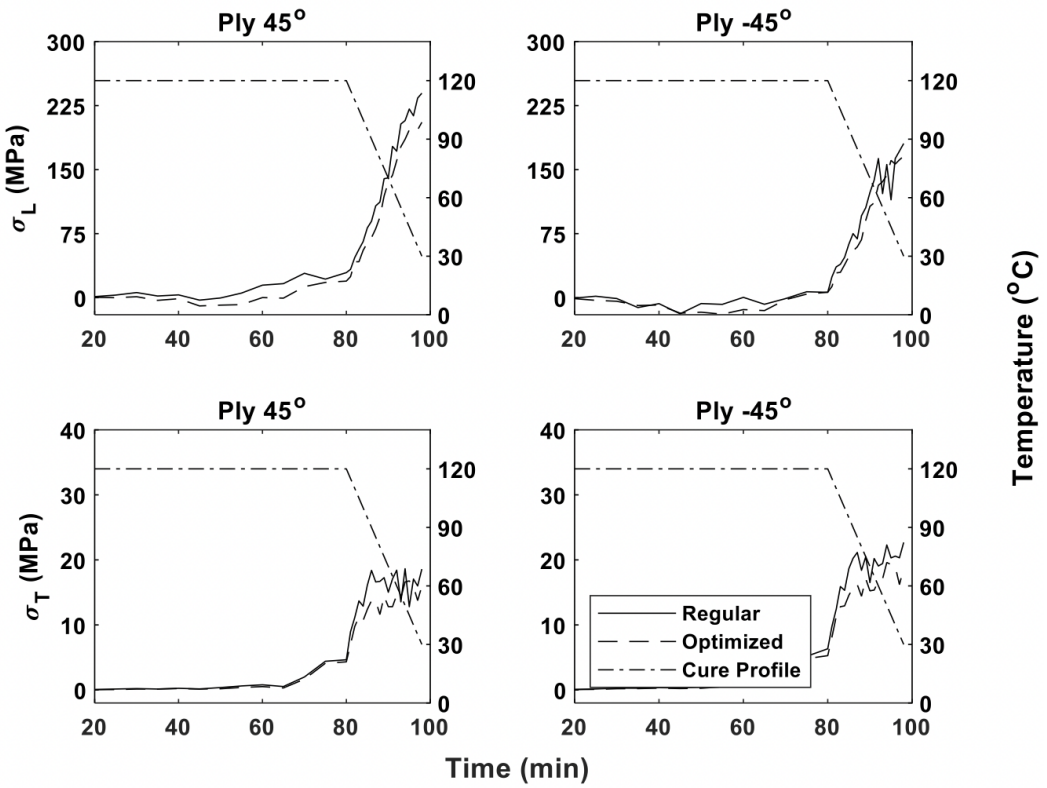

Figure 4.7 Residual stresses comparison for [45/-45/45/-45] laminate.

Residual stresses evolution for the balanced unsymmetrical [30/-30/60/-60] laminate can be seen in Figure 4.8. It can be noticed that for this laminate all the plies experienced large residual stress reduction for the laminate manufactured through modified cure compared to the one manufactured through regular cure. This reduction of 31.82% is the highest among all the layups considered in this research as seen in Table 4.1.

For this balanced unsymmetrical [30/-30/60/-60] laminate, during the isothermal stage, the 60° ply exhibits a minimal change in residual stress, while the -30° ply shows a higher difference in the stresses, in the longitudinal direction. In the transverse direction, there is a small change during the isothermal stage of the cure but the residual stresses associated with the modified cure are lower during the cool-down stage.

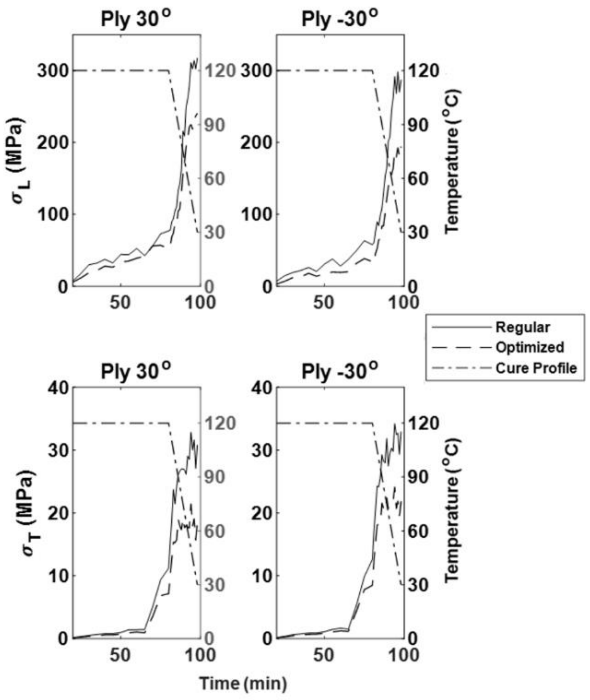

Figure 4.8 (a) Residual stresses for [30/-30/60/-60] laminate in 30 and -30 plies.

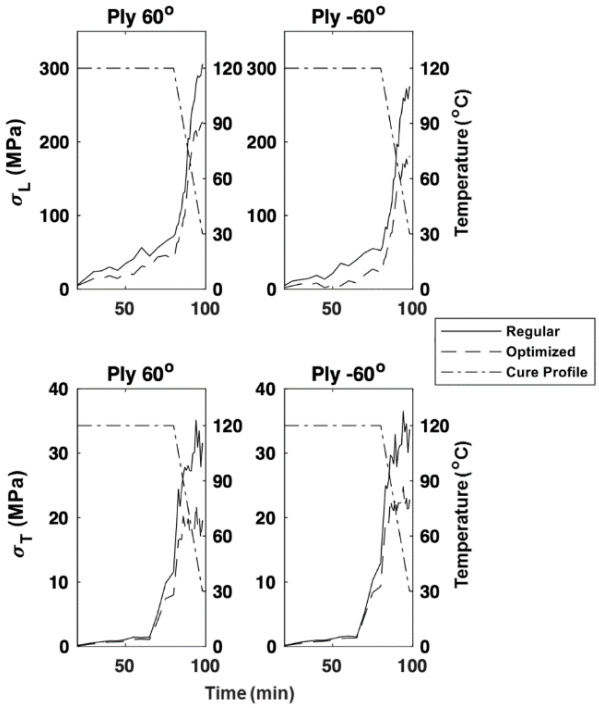

Figure 4.8 (b) Residual stresses comparison for [30/-30/60/-60] laminate in 60° plies.

The continuous evolution of residual stresses during the cure for the unsymmetrical [0/30/45/90] laminate is shown in Figure 4.9. For this layup, in the longitudinal direction, the 0^o ply exhibited reduced stresses from the start of the isothermal stage, unlike the other three plies where the difference in stresses is observed only during the cool-down stage. In the transverse direction, like the other layups, only a small difference is observed during the isothermal stage, but the residual stresses are significantly reduced during cool down for all the plies. Maximum residual stress in each layup for the regular cure and modified cure are compared in Table 4.1.

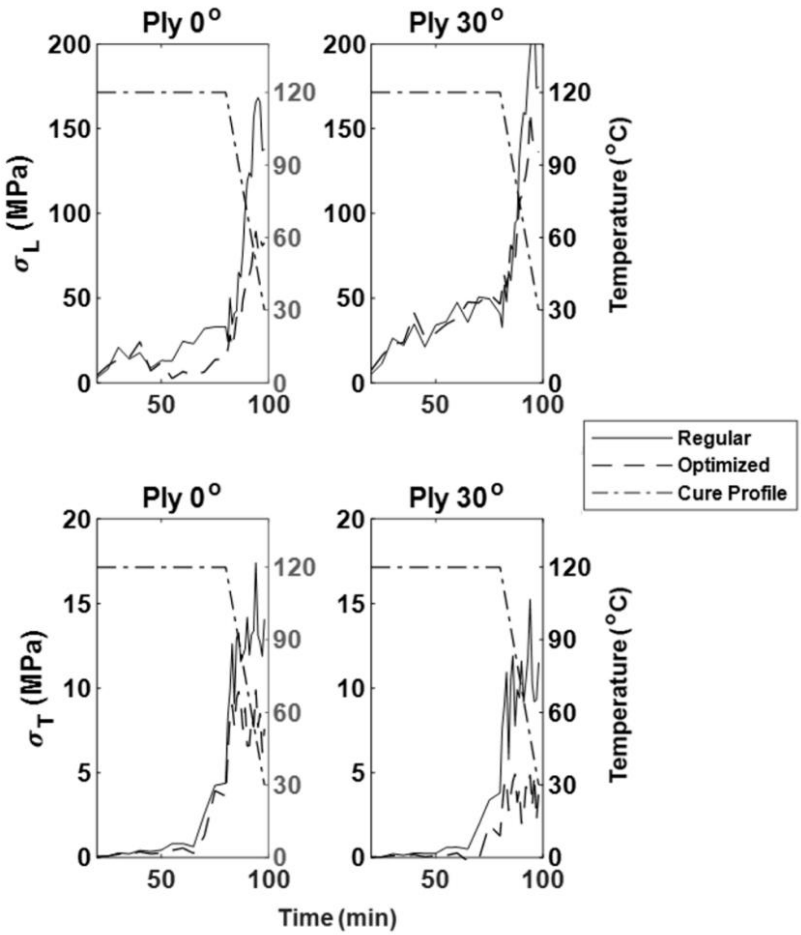

Figure 4.9 (a) Residual stresses for [0/30/45/90] laminate for 0 and 30 plies.

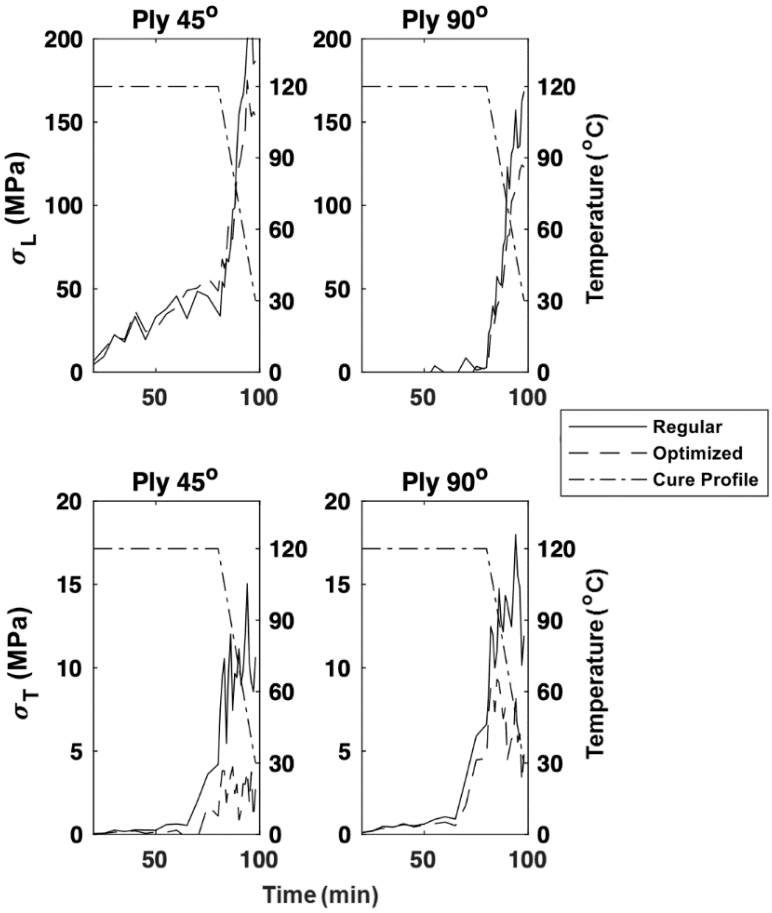

Figure 4.9 (b) Residual stresses for [0/30/45/90] laminate for 45 and 90 plies.

Table 4.1

Maximum residual stresses and respective ply orientation for all configurations

Layup Configuration	**Ply Orientation**	**σ max (MPa)**	**σ max (MPa)**	**% Decrease**
		(Regular)	**(Modified)**	
$[0/90]_s$	90°	321	272	15.26
$[0/45/]_s$	45°	198	180	9.09
[45/-45/45/-45]	45°	164	130	20.73
[30/-30/60/-60]	60°	242	165	31.82
[0/30/45/90]	30°	115	81	29.57

4.2.3. Mechanical Testing

The first-ply failure strength for the layups considered is shown in Figure 4.10 (b). Figure 4.10 (a) shows the loading response for a [0/90]s specimen. The first ply failure is captured using the acoustic emission due to the first crack, which often causes a kink in the loading response due to the load redistribution in most of the tests. This is observed for both regular cure and modified cure as shown in the insets in Figure 4.10 (a). All the mechanical testing results in this research are an average of three tests per layup configuration as shown with error bars in Figure 4.10 and Figure 4.11.

In general, the plies perpendicular to the loading direction in a tensile test are prone to fail first. Here, the tensile testing direction is 0° and the perpendicular direction is 90°. Among all the laminates, the cross-ply [0/90]s and unsymmetric [0/30/45/90] laminates contain 90° ply in their layup. The 90° ply in [0/90]s exhibited a 12% decrease in longitudinal residual stresses through modified cure while improving 5% in the first-ply failure strength.

In the case of [0/30/45/90] laminate, the 90° ply exhibited a 71% decrease in longitudinal residual stresses with a 22% increase in the first-ply failure strength as seen in Figure 4.10 (b). Similarly, the first ply failure strength increased for all the specimens processed through the modified cure cycle. This increase in strength can be directly attributed to the decrease in residual stresses in the respective layups. Samples from all the layups are also tested until ultimate failure and the corresponding stresses at failure are shown in Figure 4.11. The strength of the laminates increased for all the layups due to cure cycle modification. A maximum increase in strength of 12% is observed for unsymmetric [0/30/45/90] laminate followed by the cross-ply layup.

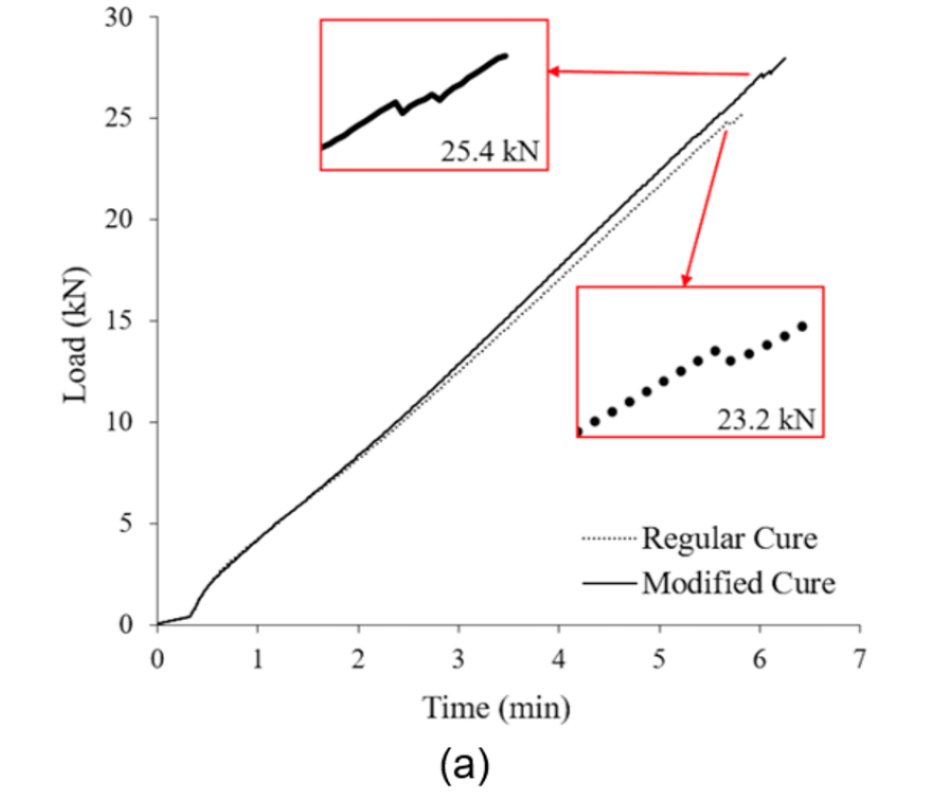

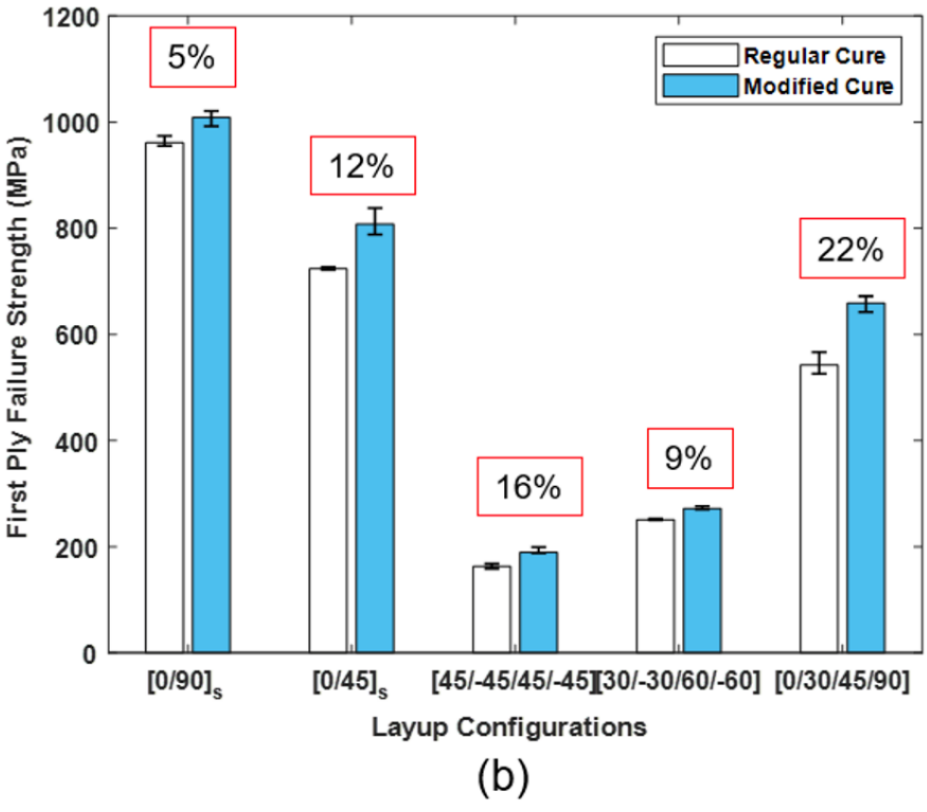

Figure 4.10 First-ply failure load for all the layup configurations.

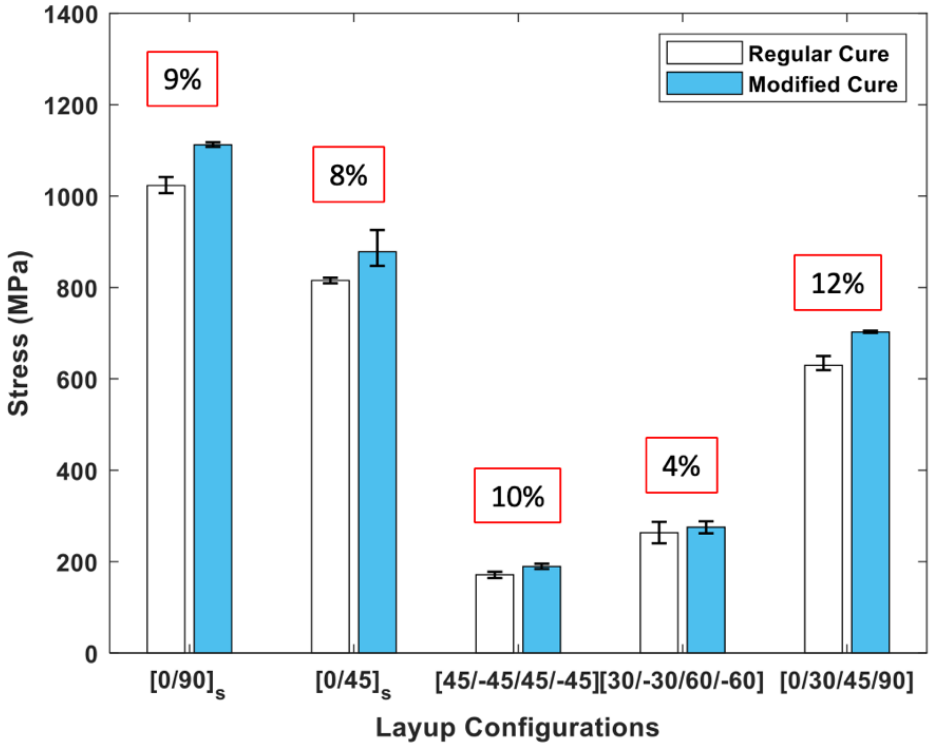

Figure 4.11 Stress at failure for all the layup configurations.

The micrographs of the fracture analysis for all the laminates cross-sections after tensile testing from SEM are shown in Figure 4.12 (i) & (ii) (a-e). The fracture initiates in the middle of the tensile specimen in most of the samples. The analysis indicates that there is an initial fracture of the specimen which corresponds to first ply failure, in addition, there is subsequent delamination as is commonly observed in composite fracture. A kink in the tensile response corresponding to the acoustic emission in many tensile tests confirms this independently.

Processing of the composite without pressure contributes to the delamination after the initial fracture (Strong, 2008). Further, the extent of damage in unsymmetric laminates correlates with the ply angle distribution. The laminates with coarse ply angle distribution exhibited more damage due to the development of interlaminar edge stresses. Each ply in

the laminate will carry the load along the direction of the fibers which explain the more visible fibers damage in the [0/90]s and [0/30/45/90], compared to symmetric laminate such as [0/45]s and balanced laminates such as [30/-30/60/-60]. These observations reinforce the recommendation to select both symmetric and balanced layups for structural applications to avoid extension/bending and shear couplings during tensile loading (Agius et al., 2016).

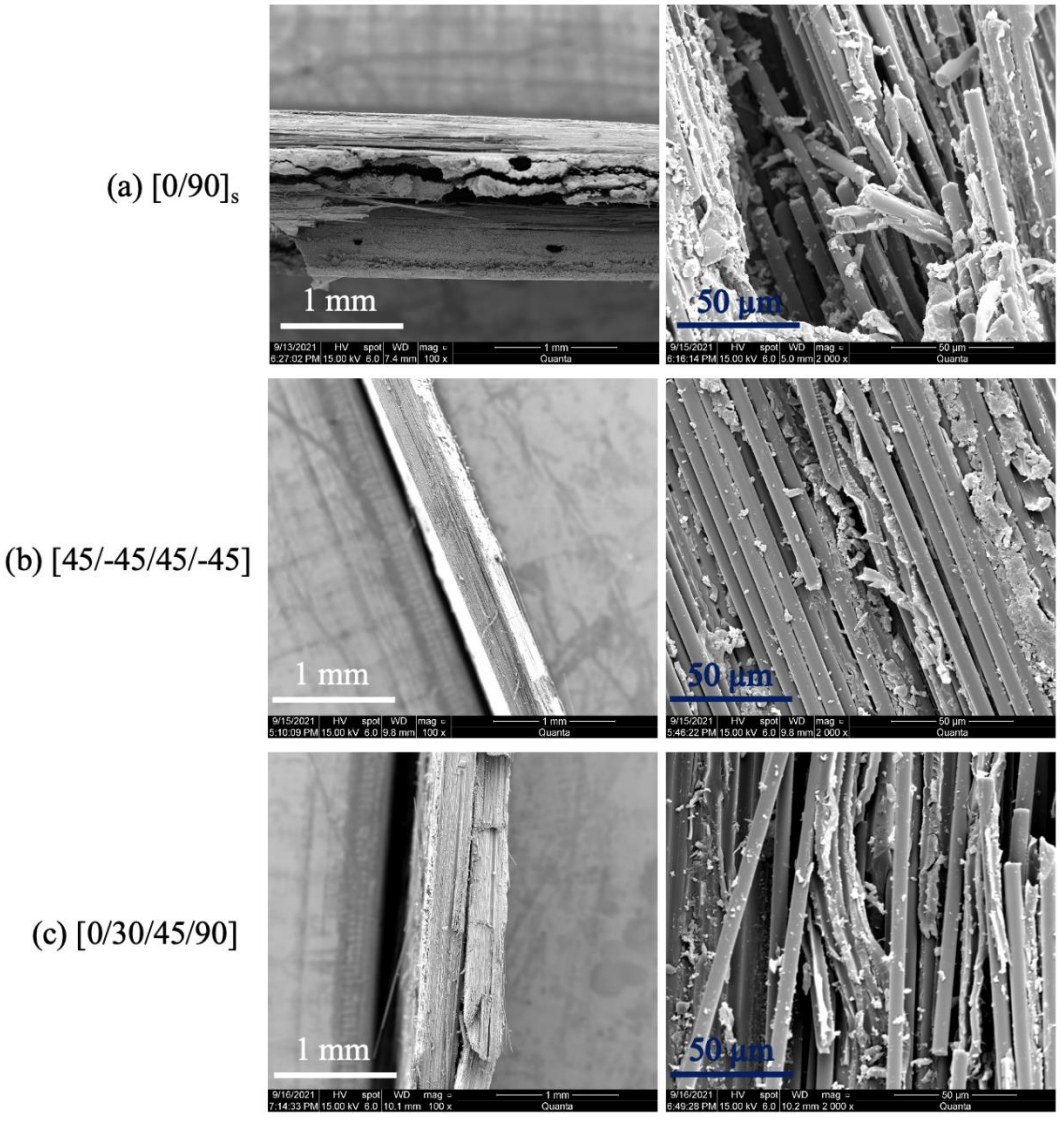

Figure 4.12 (i) Scanning Electron Microscopy (SEM) of the fracture surfaces at two scales (1mm (Left) & 50µm (Right)) for (a) $[0/90]_s$, (b) [45/-45/45/-45], (c) [0/30/45/90].

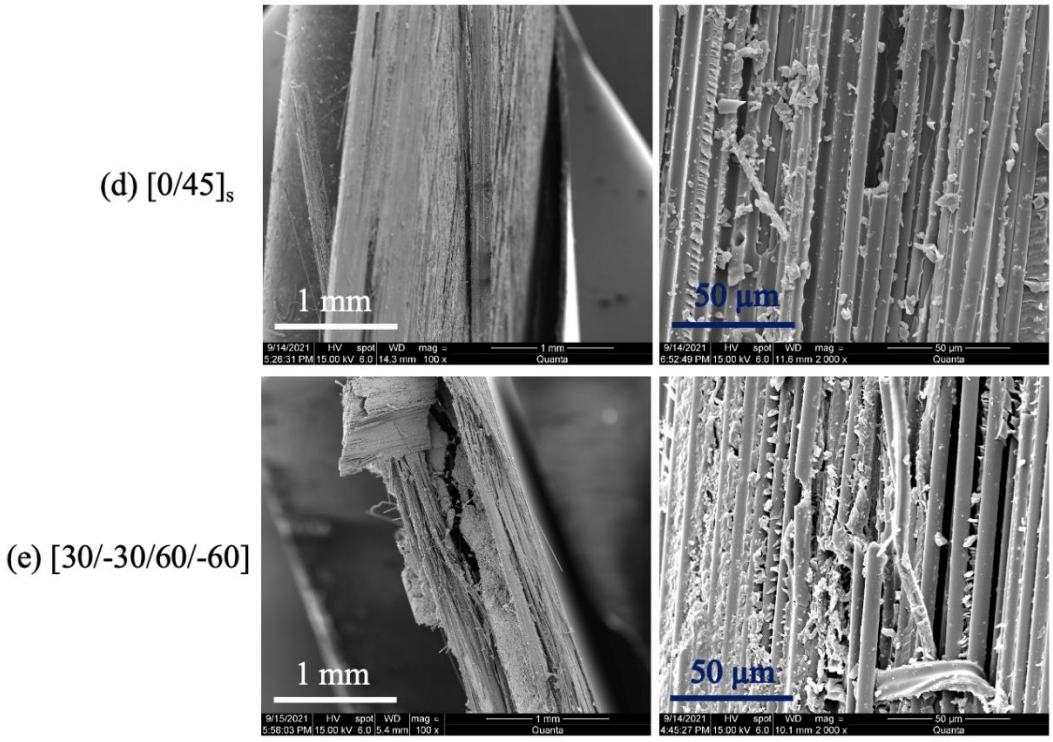

Figure 4.12 (ii) Scanning Electron Microscopy (SEM) of the fracture surfaces at two scales (1mm (Left) & 50µm (Right)) for (d) $[0/45]_s$ and (e) [30/-30/60/-60].

4.2.4 Discussion

Residual stresses in composite laminates can cause debonding, delamination, warpage, and other processing induced defects. While there are several experimental and modeling techniques to measure residual stresses, there are only a few techniques available in the literature developed for reducing the residual stresses. Based on the calculations of the micromechanical residual stresses within the epoxy, Weitsman (1979) suggested that modifying the cure profile by designing a cool-down path considering the viscoelastic response of material will yield lower residual stresses after the cure. White et al. (1993) investigated the effects of dwell temperature, dwell time, cool-down rate, and cool-down pressure on residual stresses using unsymmetric cross-ply composite laminate.

They reported that low-temperature curing reduced the residual stresses as the curvature decreased by 30%, but it increased the cure time from 240 min to 400 min. Kim et al. used three rapid cooling points in the cure profile to control the bonding temperature of the interface between the fiber and resin during the curing of carbon/epoxy composites (S. S. Kim et al., 2012). They reported that adding a rapid-cooling point in the cure profile will decrease the processing induced thermal residual stresses.

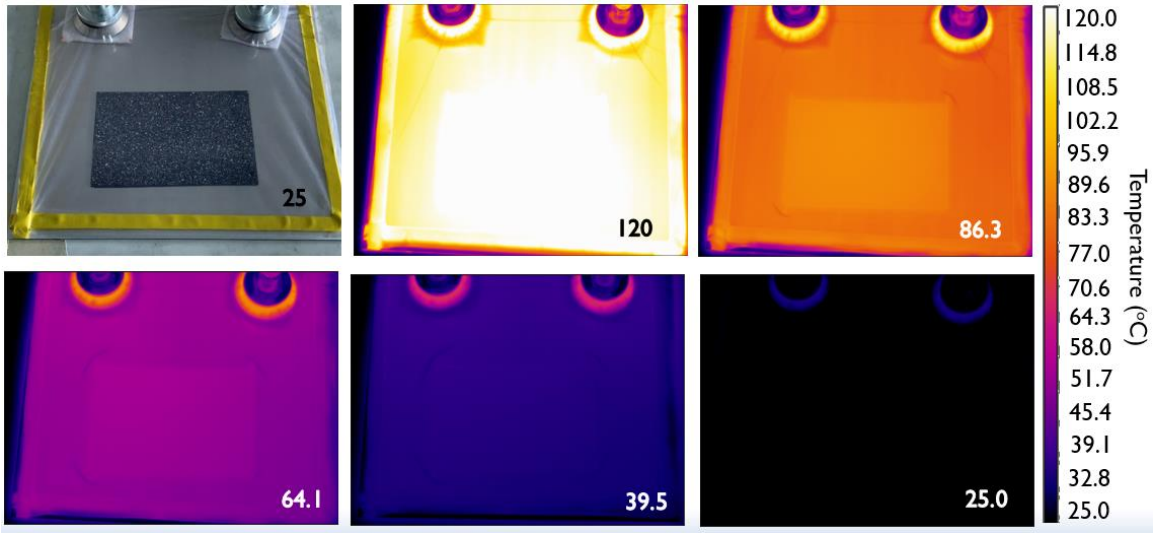

Figure 4.13 Thermal images of $[0/90]_s$ laminate during interrupted cool-down.

Experiments show that an abrupt-cooling operation after gelation could efficiently dissipate the strain generated by the laminate thermal contraction due to the resin's viscoelastic behavior (H. S. Kim et al., 2013). It is reported that this reduction in strain decreases the bonding temperatures between adjacent plies thereby reducing the residual stresses. All the layups considered in this research have only four plies and the total thickness of the laminate after cure is around 1mm. Due to the lower thickness of the samples, through-thickness variations in temperature are likely very small. Therefore, the contribution of thermal gradients to residual stress and deformations is expected to be

negligible (Hubert et al., 2012). Regarding chemical gradients, Palmese et al. (1994) noted that when the characteristic time for diffusion is less than the duration for chemical reaction, there are no significant chemical gradients. Interrupting the cure at the gel point and abruptly cooling the sample decreases the resin diffusion. On the other hand, the chemical reaction continues due to the exothermal reaction heat during the cure interruption. Therefore, chemical gradients are not expected to play a significant role.

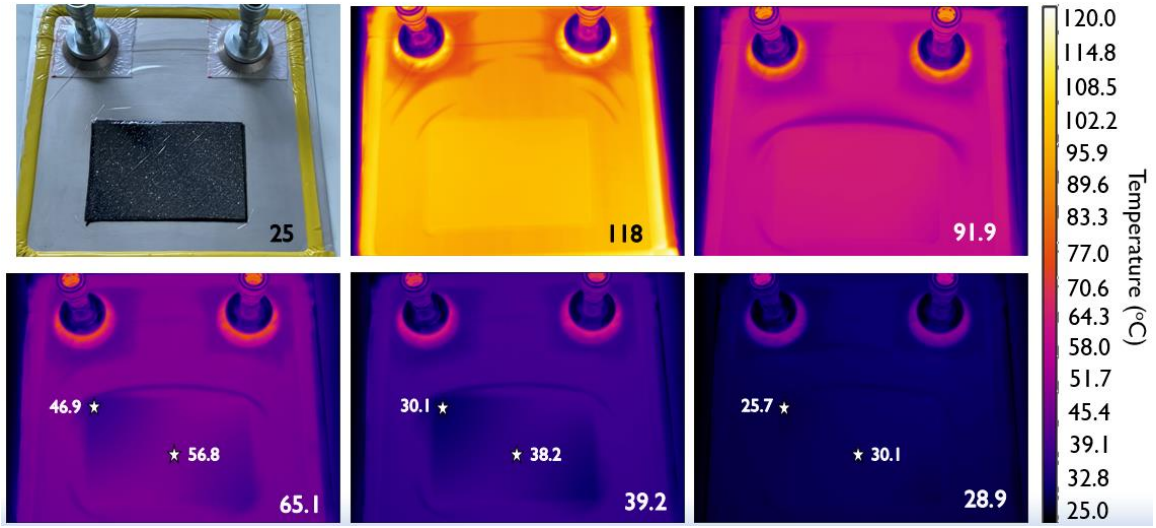

Figure 4.14 Thermal images of [45/-45/45/-45] laminate during interrupted cool-down.

The phenomenon of low-temperature curing during the rapid cooling process can be analyzed using thermal images of the specimen. Thermal analysis pictures in Figure 4.13 – Figure 4.16 correspond to the region between gel point and R2 in Figure 4.1 (c) for the $[0/90]_s$, [45/-45/45/-45], [30/-30/60/-60], and [0/30/45/90] respectively. It is instructive to observe the images of asymmetric layups as these layups are expected to create warpage during cure (Chava & Namilae, 2021a). For example, the anti-symmetric angle-ply [45/-45/45/-45] layup will have a twist warpage at the corners associated with curing. This warpage reduces the contact between the tool and the part, resulting in a higher cooling

rate at the corners, which can be observed in Figure 4.14. This indicates that the curing and bonding are happening during the rapid cooling process. A similar phenomenon of low temperature curing during interrupted cool-down can also be observed in Figure 4.15 and Figure 4.16. This low-temperature cure is responsible for lower bonding temperatures and also the decrease in residual stresses.

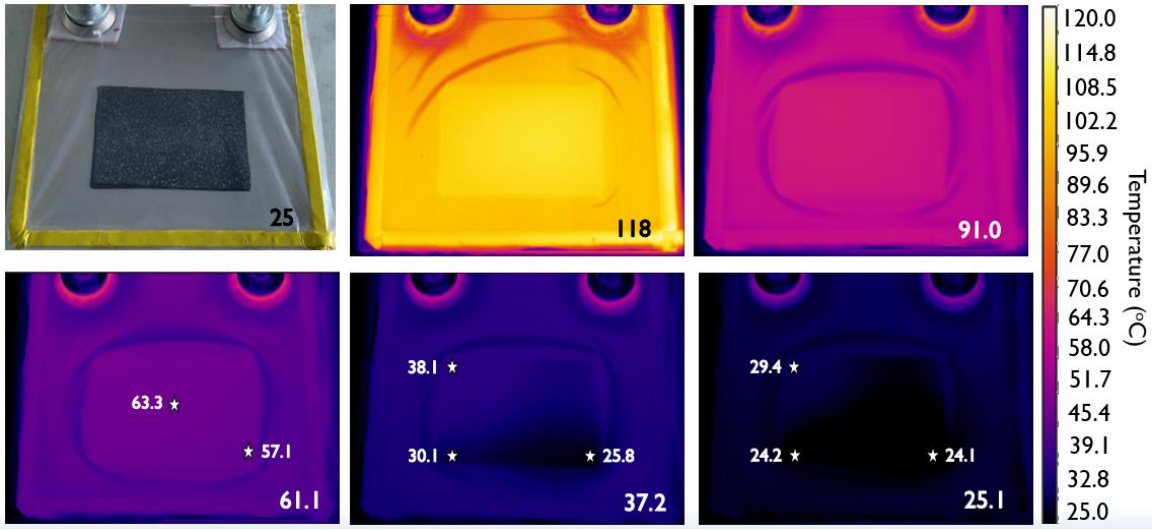

Figure 4.15 Thermal images of [30/-30/60/-60] laminate during interrupted cool-down.

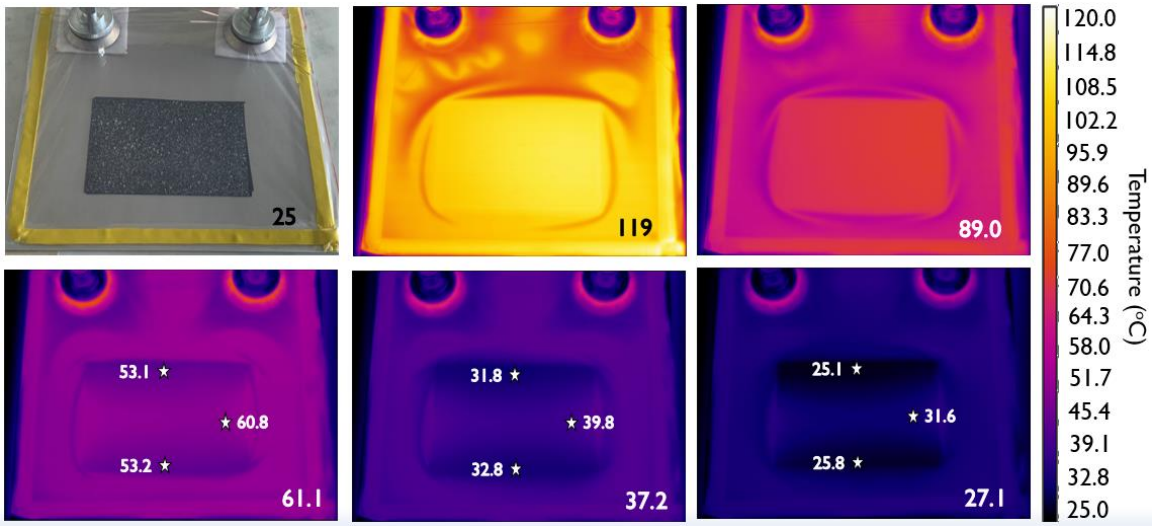

Figure 4.16 Thermal images of [0/30/45/90] laminate during interrupted cool-down.

The varying temperatures during cure, mismatch of CTE between the fiber and matrix, the chemical stresses due to matrix shrinkage, and the bonding temperature, play vital roles in residual stress buildup after the resin reaches its gel point. As the bonding temperature is reduced, the stress buildup from the stress-free point is also reduced. This reduction in stresses is amplified after vitrification and during the cool-down stage. From Figure 4.5-Figure 4.9, it can be observed that in the longitudinal direction all layups exhibited lower stresses for the modified cure cycle compared to the regular cure cycle from the starting of the cure cycle. The difference however between modified cure and regular cure is substantially increasing after vitrification during the cool-down. In the transverse direction, all layups exhibited almost identical stresses in the isothermal stage, but the modified cure approach results in much lower residual stresses during the cool-down. This detailed observation can only be made through the novel in-situ experimental approach developed in this research.

The cure interruption point in the modified cure profile is the primary process design variable that plays a key role in reducing the residual stresses. This is chosen to be the gel point of the resin i.e., the cross-linking of the resin begins at this temperature. For the matrix considered in this research, the gel point is at 120^{o}C. Abruptly cooling the material at this point will continue the chemical reaction at low temperatures as seen in the thermal images in Figure 4.13-Figure 4.16. Choosing the interruption point before the gel point is ineffective as the resin cross-linking will not start before the gel point. To achieve chemical bonding to happen at lower temperatures, interrupting the cure post gel point will not be effective either. Therefore, the cure interruption point is chosen when the sample reaches this temperature. Several other researchers (H. S. Kim et al., 2006; S. S.

Kim et al., 2012; Koyama et al., 2005; Soohyun et al., 2015) use a similar approach for cure interruption.

Numerous researchers have reported that the decrease in residual stresses results in an increase in the strength of the composites after the cure. Kim et al. (2013) observed that a 50% reduction in thermal residual stresses for a cross-ply $[0_5/90_5]_s$ layup improved the static strength and fatigue life by 16% and 614%, respectively. Agius et al. (2016) reported that a 25% increase in residual stresses in resin-infused carbon-fiber laminates reduced the composite's short beam shear strength by 16%. The first-ply failure is another method adopted by researchers to quantify the amount of residual stresses within a composite laminate (Crasto & Kim, 1993; Hassan et al., 2017; R. Y. Kim & Hahn, 1979).

Typically, a decrease in residual stresses should amplify the first-ply failure strength. It can be observed from Figure 4.10 that the first-ply failure load increased for all the layups with modified cure profile with unsymmetric [0/30/45/90] layup exhibiting a maximum increase of 22%. Similarly, the stress at complete failure for modified cure profile also increased for all the layups considered in this study with unsymmetric [0/30/45/90] layup exhibiting a maximum increase of 12%. These strength increases are identical to those observed in the literature. While there are several methods to evaluate the residual stresses post-cure, the current approach can uniquely perform continuous evolution of processing induced residual stresses throughout the cure. This approach was used to modify the cure cycle to reduce residual stresses and thereby increase the strength of the specimen. The current approach also has the potential to dynamically adjust the cure cycle while curing based on the real-time residual stress evolution data.

4.3 Experimental Procedure for Interfacial Modification

4.3.1 ZnO Nanorods Synthesis

Plain-woven carbon fiber fabric samples with ZnO nanorods used in this research are provided by Dr. Marwan Al-Haik's group. A brief description of the synthesis process is described here and a detailed description can be found at (Ayyagari & Al-Haik, 2019). Two procedures: seeding and growth are used for the ZnO nanorod synthesis bonded to the carbon fabric substrate. The dip-coating method was employed for seeding and the seeding solution was prepared with 658.4 mg of zinc acetate dehydrate (Alfa Aesar, Tewksbury, MA, USA), 600 mL of deionized (DI) water, and 80 mL of ethanol, sonicated together for 10 min. The carbon fiber substrate is dipped in this solution for five iterative cycles that include dipping, drying, and rinsing with ethanol. The substrate is further dried at 100^{o}C for 30 min after the completion of the seeding procedure.

The growth procedure involves preparing a bath of DI water, in which zinc acetate dehydrate and hexamethylenetetramine (HMTA, Alfa Aesar, Tewksbury, MA, USA) were added in adequate amounts. The homogenized mixture of zinc acetate dehydrate (15.72 g) and HMTA (10.09 g) with DI water (3600 mL) is achieved via sonication. Growth time of 8 hrs. at 90^{o}C is chosen based on a parametric study for the time and temperature dependence of the length and diameter of nanorods. After this time, ZnO nanorods are fully grown on the carbon fiber fabric.

4.3.2 Experimental Setup

The fabric samples with ZnO nanorods are impregnated with a PR2032 and PH3665 epoxy resin system. This resin system has a specific gravity of 0.95 with a viscosity of 200-250 cps. The manufacturer recommended curing temperature is 93^{o}C (200F) with a

30 min dwell time at 30°C and 2.5 hours hold time at 93°C. This cure cycle is divided into two stages with the first stage executed in Grieve oven executing the 30 min dwell at 30°C followed by temperature ramp-up to 93°C. In the second stage, the specimen is moved to autoclave which is preheated to 93°C and the specimen is cured for 2.5 hours followed by cool-down. The custom autoclave 3D DIC is again used in this study. A random high contrast speckle pattern is sprayed on the surface ply of the specimen after the first stage before moving to autoclave using high-temperature spray paint. Surface ply deformations and strains during the composite processing are obtained by extracting full-field information from this applied speckle pattern. The cure cycle recommended by the manufacturer is converted into a step-by-step recipe, which is then programmed into Grieve oven and composite processing control (CPC) of the autoclave computer. All the samples consist of two-ply layups and are of similar weight.

4.3.3 Specimen Preparation

Composite laminates of dimensions 152.4 mm x152.4 mm (6 inch x 6 inch) are fabricated using two plies of woven carbon fiber fabric in two sets: without ZnO nanorods (regular) and with ZnO nanorods (modified) in [0/0] orientation. After cure, another set of specimens with dimensions 12.6 mm x 152.4 mm (0.5-inch x 6-inch) are prepared for both regular and modified layups from the original samples. Mechanical tests are executed using MTS tensile machine. Dynamic mechanical analysis (DMA) using PerkinElmer - DMA 8000 is performed to characterize temperature-dependent dynamic mechanical properties of the composite material. Differential scanning calorimetry (DSC) using DSC-3 from Mettler Toledo is performed to measure the degree of cure for the prepreg resin.

4.4 Results & Discussion for Interfacial Modification

4.4.1 Elastic Properties & Cure Kinetics for Fabric Samples

Temperature-dependent modulus (E(T)) values are experimentally extracted through the DMA of the sample. The average modulus at the end of the cure is 570 GPa at room temperature. DMA has also been employed to get the tanδ peak of the prepreg used in this research. This peak is occurring around 93°C which represents the point of stress-free temperature or gel point of the matrix in the resin.

4.4.2 DIC Data Analysis for Interfacial Modification

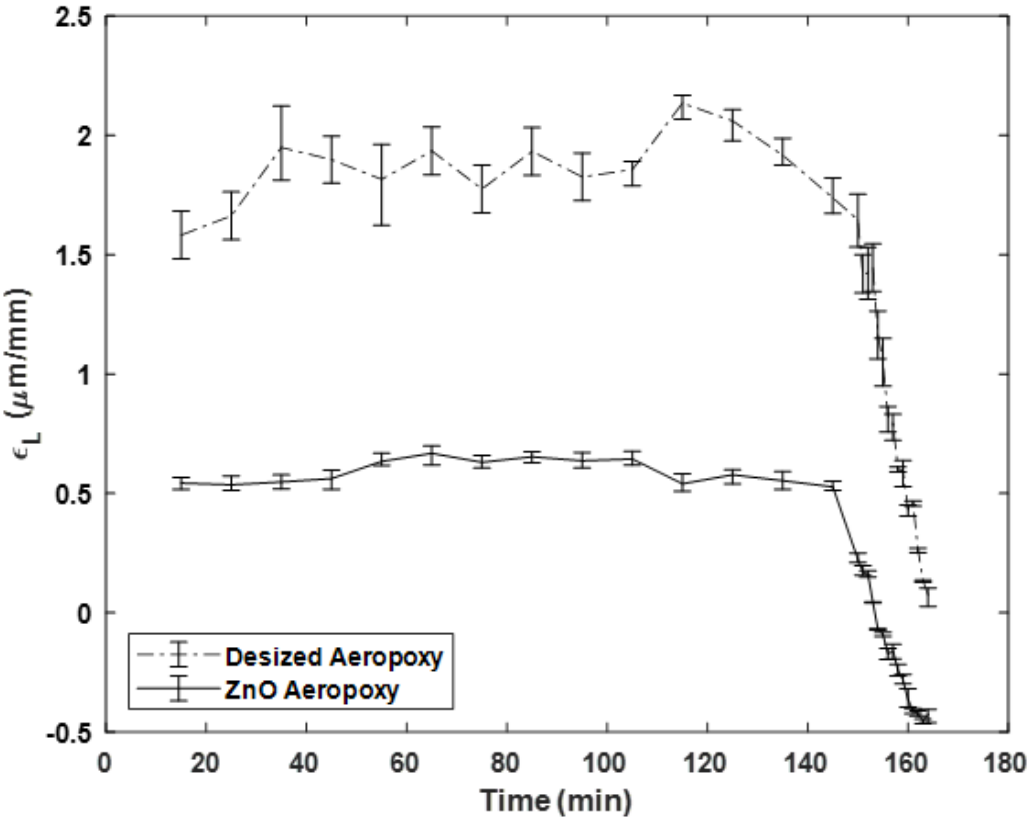

Figure 4.17 Longitudinal strain comparison during cure.

Pictures from DIC cameras are analyzed using VIC-3D software to measure the in-situ surface strains of both desized and ZnO specimens during the second stage after

moving it to the autoclave. As the focus of this research is on residual stresses, the strains are plotted from the start of the isothermal stage to analyze the strain and stress build-up from the stress-free point (gel point).

The continuous strain evolution in the longitudinal direction and transverse direction can be seen in Figure 4.17 and Figure 4.18 respectively. For [0/0] layup, the strain in both directions can be seen decreasing after vitrification. Comparing the results between the regular desized sample and the ZnO Aeropoxy sample, the preliminary results using this approach in the experimental setup look very promising in decreasing strains. As a future direction, this interfacial modification has the potential to decrease residual stresses in composite laminates.

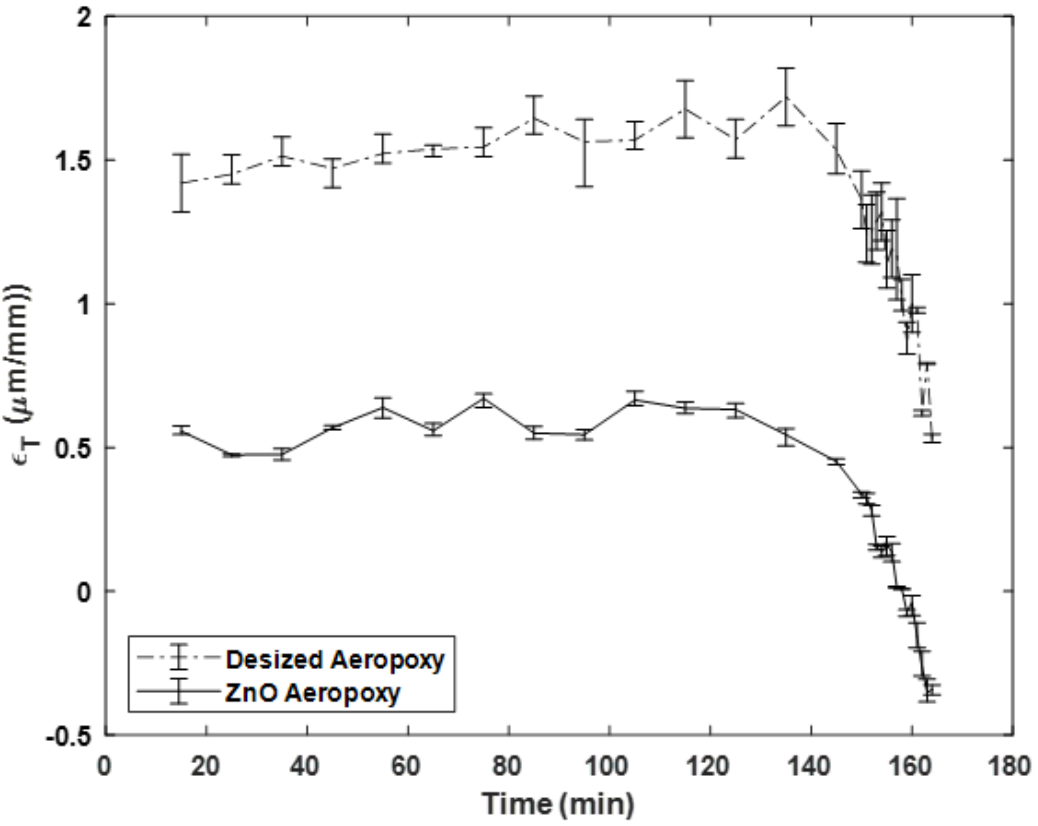

Figure 4.18 Transverse strain comparison during cure.

4.5 Summary

Residual stresses are detrimental to any composite structure as they induce defects like debonding, delamination, matrix cracking, etc. The ability to monitor the residual stresses throughout the cure process and develop methods to reduce these stresses is vital due to the rapid growth in the use of composite structures.

In the current work, a modified cure approach is developed to reduce processing-induced residual stresses in composite laminates. A novel approach to using ZnO nanorods to modify the ply interface to reduce in-situ cure strains is also examined. The main research findings are summarized below:

a. An in-situ characterization approach is developed to monitor the evolution of residual stresses during processing and is used to develop approaches to reduce residual stresses.

b. A modified cure approach based on interrupting the cure after gelation is effective in reducing the residual stresses for both symmetric and asymmetric layups.

c. The decrease in bonding temperatures due to the abrupt cooling operation resulted in lower residual stresses after vitrification. This is observed for all the layups considered in this research.

d. Among all the layups, a maximum reduction of 31.8% is observed for the balanced unsymmetric angle-ply [30/-30/60/-60] laminate.

e. The decrease in residual stresses after cure increased both the first-ply failure load and ultimate strength of all the layups studied in this research.

f. A maximum increase of 22% for first-ply failure load and 12% for failure strength is observed for the unsymmetric [0/30/45/90] laminate.

g. Approach using ZnO nanorods to modify the ply interface show promising results in reducing cure-induced strains which often correlate with a reduction in residual stresses.

5. In-situ Detection of Defects during Composite Manufacturing

The kinematics of composite ply-interfaces critically affects both the manufacturing processes and deformation mechanisms and is often responsible for the formation of defects such as wrinkles and delamination. In the present chapter, processing induced defects in a carbon fiber prepreg composite are evaluated by devising a novel in-situ experimental approach. Carbon fiber prepreg laminates are cured in a specially designed autoclave with viewports with plies laid up on a mold with cylindrical tooling set up to maximize the ply movement. Four-ply layup orientations of $[90/90]_s$, $[90/0]_s$, $[90/45]_s$ and $[90/-45]_s$ and three mold configurations with cylindrical tools of diameter 9.5 mm (3/8 inch), 12.7 mm (1/2 inch) and 15.9 mm (5/8 inch) are used for the parametric study. Strains, ply-movement, and formation of defects are observed in-situ using Digital Image Correlation (DIC) during the autoclave cure cycle, through the viewports. The processing induced defects in the composite are further characterized by X-ray micro-computed tomography (micro-CT). We observed that the mold with a larger radius of curvature (15.9 mm cylinder) leads to higher strains in both in-plane directions and higher displacement in out-of-plane directions. The maximum average out-of-plane ply movement, as well as the largest wrinkle, are observed for $[90/-45]_s$ layup on the mold with the highest radius of curvature.

5.1. Experimentation

5.1.1. Materials

Unidirectional carbon fiber prepreg was procured from Fibre Glast Corporation with manufacturer specified tensile modulus of 275.8 GPa (40 msi) and strength of 5.65 GPa (820 ksi) (*Prepreg Unidirectional Carbon Fiber Fabric*).

5.1.2. Experimental Setup

A high temperature (400 C/752 F) and high pressure (1.38 MPa/200 psi) autoclave from ASC Systems is instrumented with 3D digital image correlation (DIC) described in the earlier chapters is used here. The cure cycle from the manufacturer is converted into a step-by-step recipe, which is then programmed into composite processing control (CPC) of the autoclave computer. CPC constantly monitors the cure parameters of the cycle throughout the cure and makes changes dynamically if needed. Digital image correlation described earlier is used to measure the surface ply deformations and strains and the resulting defects during the composite processing. DIC technique works by tracking the changes in the gray value pattern in small neighborhoods called subsets in the images (Schreier et al., 2009). A reference square subset with sufficient intensity variations is selected from the reference image and compared with a deformed subset from the target image. The differences between the reference subset and the target subset yield the subset center's displacement vector.

5.1.3. Experimental Procedure

Composite specimens of dimensions 203.2 mm x 152.4 mm (8 inch x 6 inch) are prepared for fabrication using four plies of unidirectional carbon fiber prepreg in four laminate configurations with ply orientations of $[90/90]_s$, $[90/0]_s$, $[90/45]_s$ and $[90/-45]_s$. A detailed axis with orientations can be seen in Figure 5.1(c). A white speckle pattern is sprayed on the top layer of the layup as shown in Figure 5.1(b). This creates a random and high contrast pattern for digital image correlation. The layup and the tool configuration in this research are designed to maximize the inter ply-movement. Figure 5.1 (a) and (b) show the mold configurations used for this purpose.

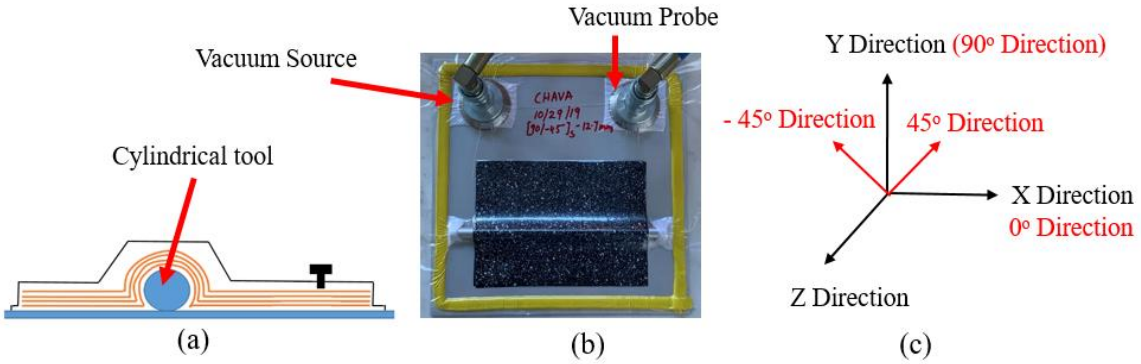

Figure 5.1 (a): Schematic of layup; (b) Layup over cylindrical tool; (c) Axis orientations.

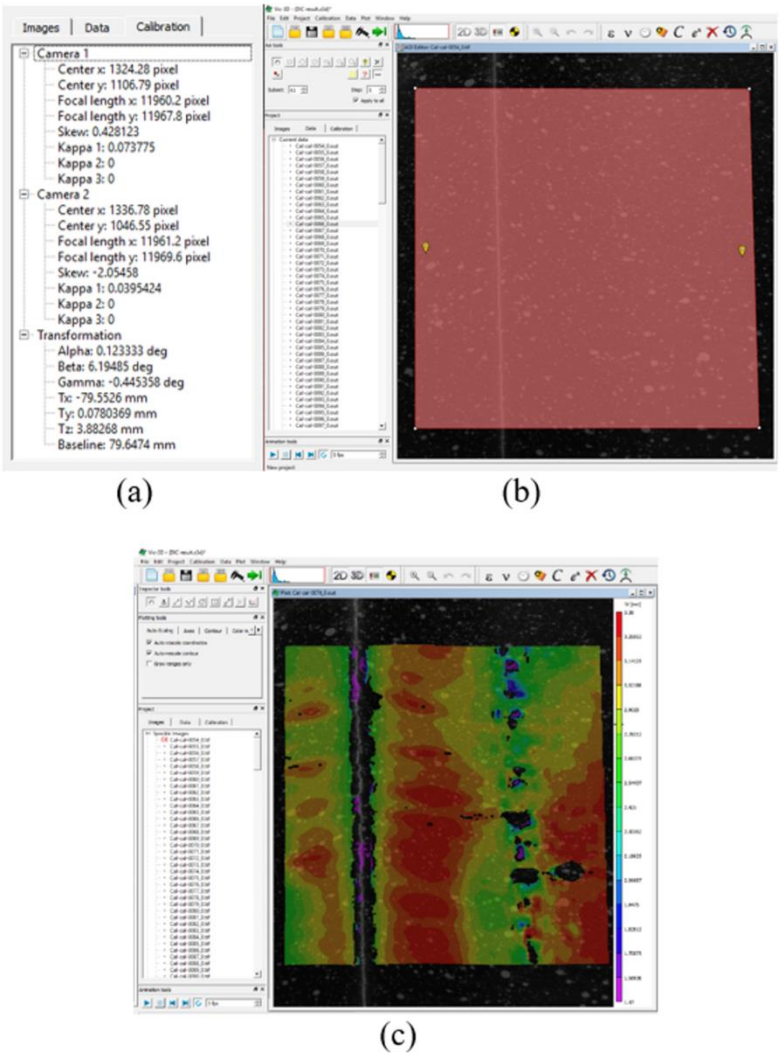

Figure 5.2 Snapshot of VIC-3D: (a) Calibration; (b) Specimen before analysis; (c) Specimen after analysis.

Researchers have observed a 40% compaction pressure drop in the curved regions of L section tools resulting in local thickness variations (Levy & Hubert, 2019). The mold configuration used in this research consists of a cylindrical rod affixed on a flat plate to create an unsupported curved region. This exaggerates the pressure drop associated with curved L-sections and thereby enables studying defect formation. Three cylindrical tools of diameter 9.5 mm (3/8 inch), 12.7 mm (1/2 inch), and 15.9 mm (5/8 inch) are used in preparing three mold configurations. A schematic of the mold configuration and the layup is shown in Figure 5.1 (a). The plies are laid upon this mold and prepared for cure using the vacuum bagging technique as seen in Figure 5.1 (b). A total of 72 specimens in 12 different configurations are tested in this research. The manufacturer provided a cure cycle programmed into the autoclave consisting of a ramp-up to 120 C (248 F) at 5 C/min and a pressure of 0.69 MPa (100 psi) for a hold time of 1 hr followed by a ramp down.

The cameras of the DIC system are set up pointing at the composite layup through the viewport of the autoclave. Calibrating the DIC system helps the cameras identify their location in space and the angles between them (see Figure 5.2 (a)). After transferring the layup to the autoclave both the autoclave and the DIC are started at the same time capturing pictures throughout the cure cycle. Due to the ply movement, there will be a relative movement in the speckles on the top layer of the layup. This relative movement of the speckle pattern is analyzed in VIC-3D software to determine the surface displacements and strains as seen in Figure 5.2 (b) & (c). The results of this experimental approach provide an insight into the interfacial motion between plies resulting in surface deformations. Further, it can be used to quantify the process conditions (temperature, pressure, cure cycle) and the tool geometry that leads to the movement of plies and the

formation of defects. The results of the in-situ experiments are combined with post-processing characterization using X-ray micro-tomography. The combination of both in-situ DIC measurement and ex-situ X-ray micro-CT defines the novel experimental approach devised in this research.

The interfacial kinematics and the related defect formation post-curing are characterized using a high-resolution X-ray microtomography (micro-CT) to reconstruct interior structural details of the specimen using the Bruker 3D X-ray SkyScan 1275. Additionally, this characterization serves as a validation for the in-situ measurements. Due to the size limitations of this X-ray machine, a portion of the original specimen of dimensions 50.8 mm x 38.1 mm (2 inch x 1.5 inch) was cut using a composite table saw. After installing the sample in the scanner, an X-ray with an energy of 40 kV is used to scan the sample from different angles. The scan is then reconstructed using NRecon software to obtain the complete 3D structural detail of the sample.

5.2. Results and Discussion

5.2.1. DIC Data Analysis

The results from the DIC are correlated to the cure cycle of the carbon fiber composite. The following plots (Figure 5.3, Figure 5.4, and Figure 5.5) are a result of one of the samples with the layup orientation of $[90/-45]_s$ laid upon a mold with the cylindrical tool of diameter 15.9 mm. The dotted line in Figure 5.3 and Figure 5.4 represents the average normal strain ε_{xx} and ε_{yy} and in Figure 5.5 it represents the average displacement in the Z (out-of-plane) direction. The corresponding contour plots show the distribution of the average displacement in the region of interest. These strains and displacement are correlated with the cure cycle temperature profile plotted against time.

The maximum average strain in X-direction is 23.63 µm/mm at the 60 min mark into the cure and from there on the strain gradually reduces to 20.92 µm/mm towards the end of the cure cycle as seen in Figure 5.3.

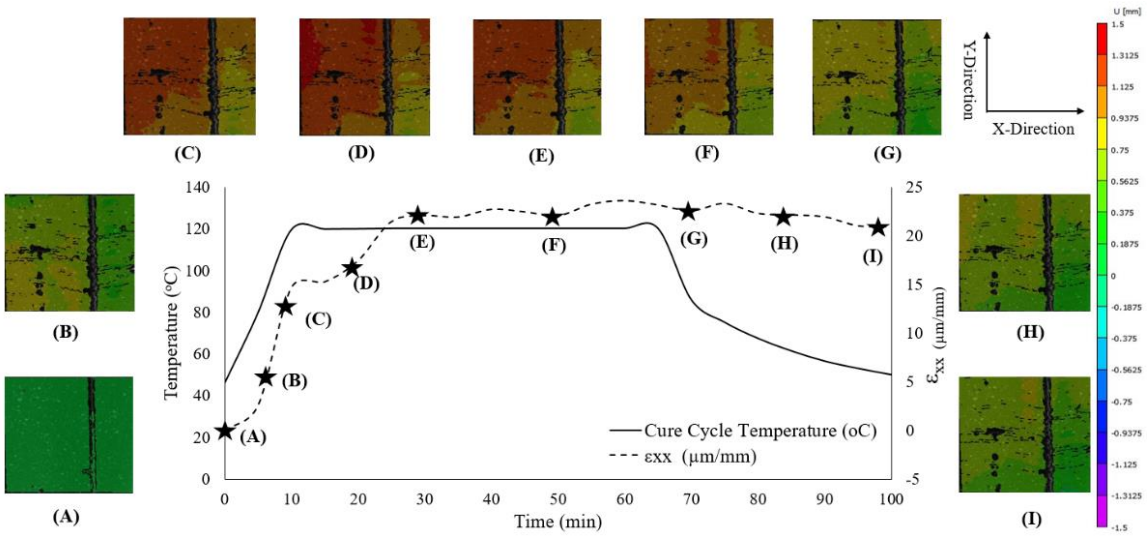

Figure 5.3 Average normal strain in the X direction and contour plots of X displacement in the region of interest.

In the Y-direction, the strain reaches a maximum average of 5.37 µm/mm at the 65 min mark which is at the end of hold time in the cure cycle. The strain then slightly reduces to 5.08 µm/mm at the end of the cycle as seen in Figure 5.4. These in-plane strains in X and Y-directions are due to the movement of speckle pattern on the surface ply, however, any significant movement in the interior plies due to thermomechanical loads during cure as well as residual stresses generated due to crosslinking of the polymer bonds will be reflected on the surface due to the relatively low thickness of the sample.

The out-of-plane displacement in the Z direction and the temperature profile are plotted against time in Figure 5.5. The maximum movement observed during the ramp-up is due to the thermal expansion and the readjustment of plies as temperature increases. A

tan delta vs temperature plot for the material used in this study is obtained from a Dynamic Mechanical Analysis (DMA) as seen in Figure 5.6. This plot shows the peak of tan delta occurring around 120 C which is the point of stress-free temperature or gel point for the material (PETHRICK, 2000). From Figure 5.5 we can note that after the ramp-up and gelation, the interfacial ply slippage next to the cylindrical tooling surface slowly increases. The restricted movement post gelation towards the end of the cure results in the formation of wrinkles as shown in displacement contours (G) to (I) in Figure 5.5.

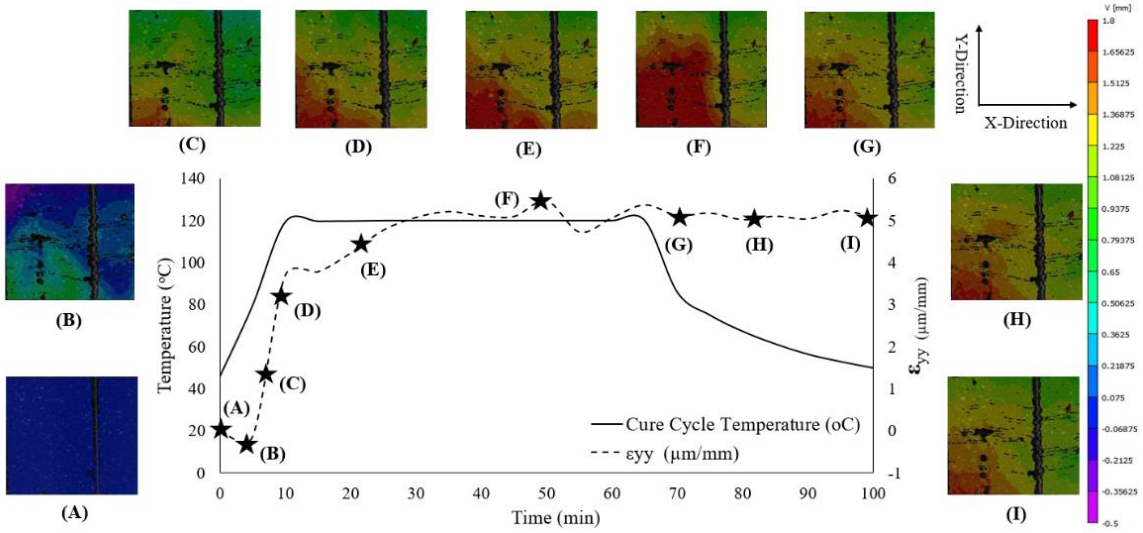

Figure 5.4 Average normal strain in the Y direction and contour plots of Y displacement in the region of interest.

The average out-of-plane displacement is -0.13 mm at the end of the cure for the region of interest (the region corresponding to the contour plot). The negative sign implies the shrinkage of thickness in z-direction during cure. The formation of wrinkles can be observed in the contour plots of Figure 5.5.

The wrinkle starts to appear initially in Figure 5.5 (G) towards the end of the hold phase and is fully developed by the end of the cure after the cool-down phase as seen in

the contours of Figure 5.5 (I). The maximum out-of-plane movement at one of the largest wrinkles after cure observed for this layup configuration is estimated to be 1.51 mm. The average results along with ply movement for all the layups are explained further in Section 3.2.

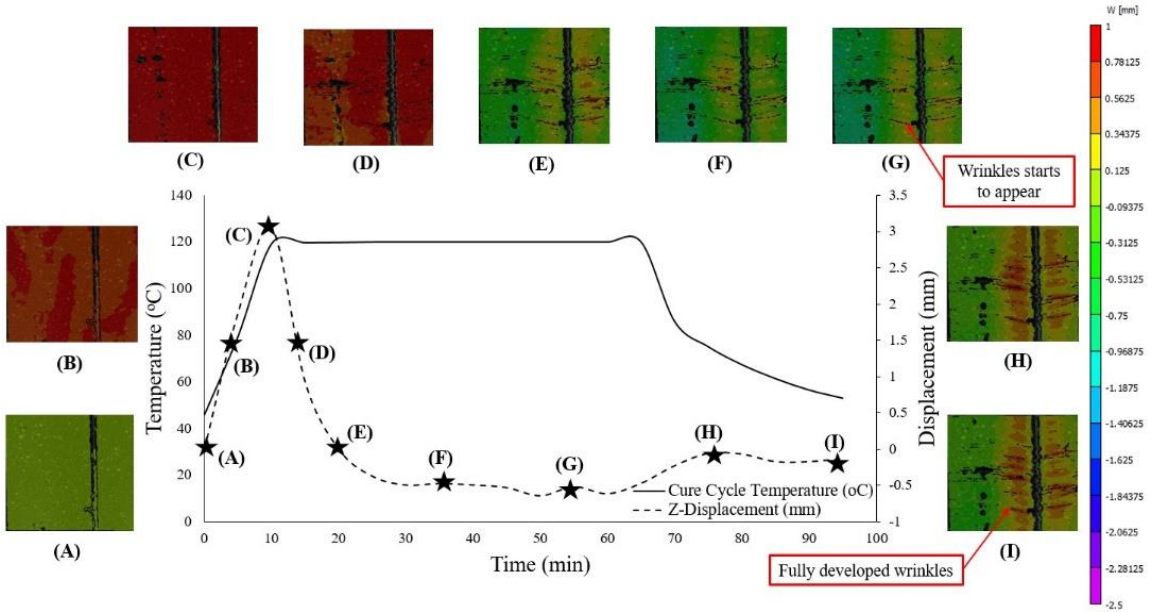

Figure 5.5 Average out of plane displacement (Z) and contour plots of Z displacement in the region of interest

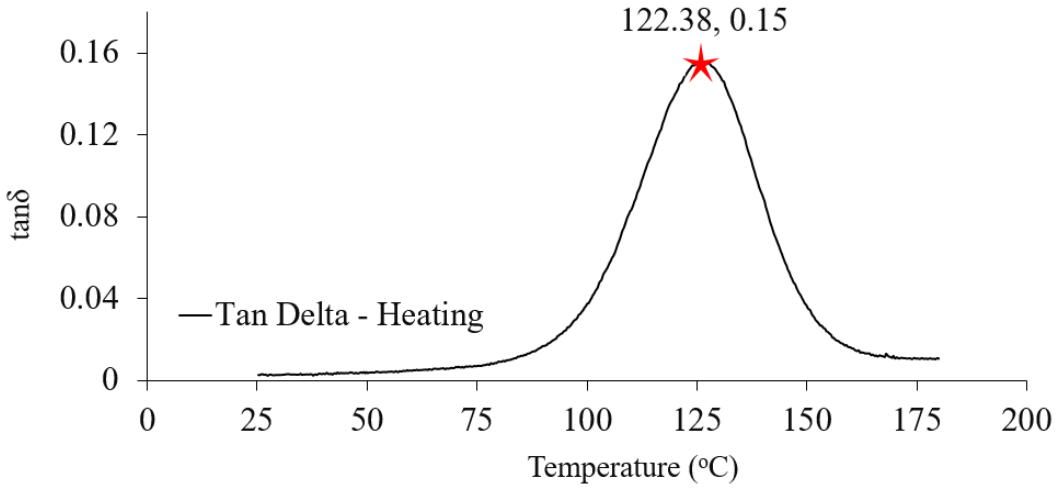

Figure 5.6 Tan delta peak showing the gel point of the prepreg material

5.2.2. Parametric Analysis of In Situ Cure Displacements

In this section, the data from DIC is analyzed with respect to the effect of the temperature cure profile followed by the effect of tool curvature and fiber orientation. DIC measures direct changes in the speckle pattern, however, the significant movements of the entire laminate including fibers are captured in these surface displacements. The cure profile consists of three phases as shown in Figure 5.7-Figure 5.9. The initial ramp-up temperature phase is followed by the hold phase and the cooling phase at the end. During the ramp-up phase of the cure cycle, the rate of change in strain is high in X-direction for all the layup configurations (see Figure 5.7). The strain rate in Y-direction is lower compared to X-direction for all the sample configurations as shown in Figure 5.8. The ply displacement in Z-direction shown in Figure 5.9, is maximum in this phase because of ply readjustment due to the thermal expansion of the plies during the ramp-up. These general trends are true for all layups and mold configurations.

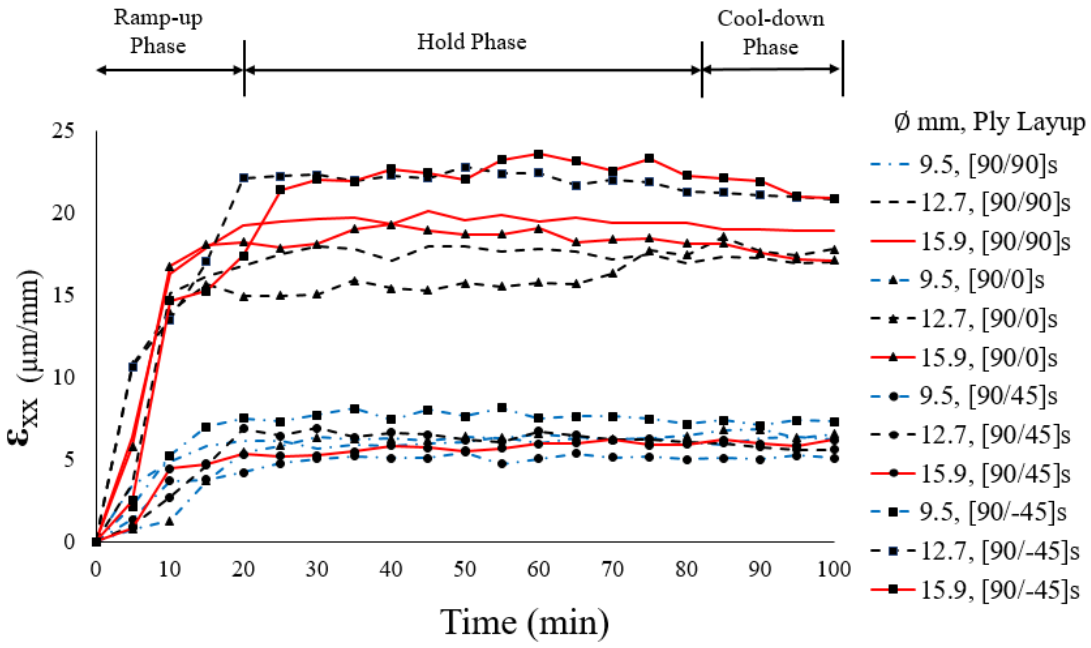

Figure 5.7 Average in-plane strain for all sample configurations through the three stages of curing.

During the hold phase of the cure cycle, a low rate of change of strain is observed in X-direction and Y-direction for all the sample configurations. In Z-direction, the displacement observed during the ramp-up phase is gradually decreased during the start of the hold phase due to chemical shrinkage. A negative Z-displacement (shrinkage compared to the original sample) can also be observed towards the end of this phase. During the cool-down phase of the cure cycle, a small if not no change in strain can be observed in X-direction. Strain in Y-direction is constant throughout the cool-down phase for all the sample configurations. In Z-direction, the displacement increases in this phase after hold due to the thermal relaxation in the sample while it is cooling down.

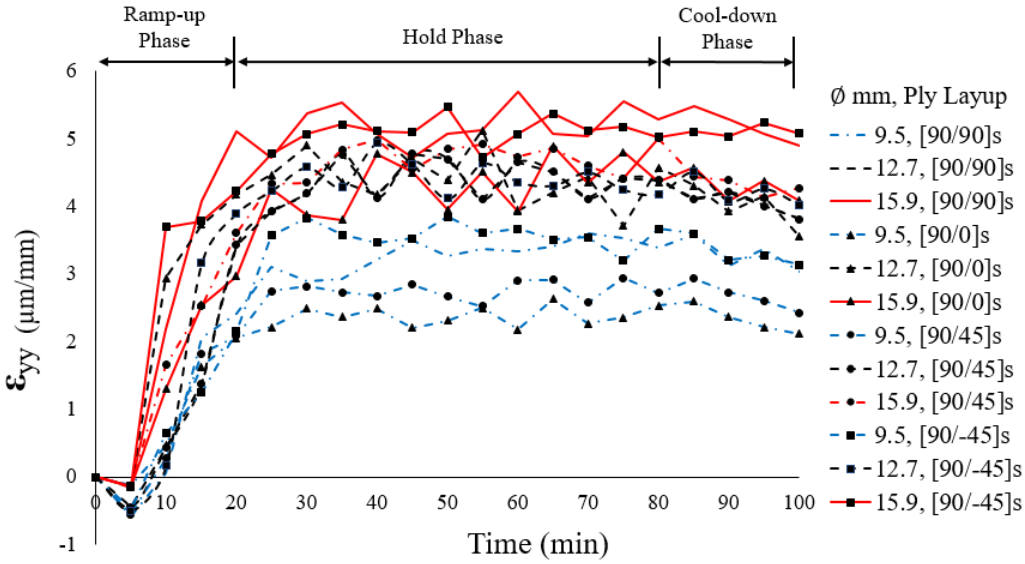

Figure 5.8 Average in-plane strain for all sample configurations through the three stages of curing.

The effect of tool geometry on the in-plane strains and out-of-plane displacement is now considered. Three cylindrical tools with diameters of 9.5 mm, 12.7 mm, and 15.9 mm were fixed on a flat plate to make the molds 1, 2, and 3 respectively for four different ply layups of $[90/90]_s$, $[90/0]_s$, $[90/45]_s$, and $[90/-45]_s$. Figure 5.10 shows the in-plane

strains in X and Y directions averaged over the region of interest. The error bars denote the standard deviation from six samples.

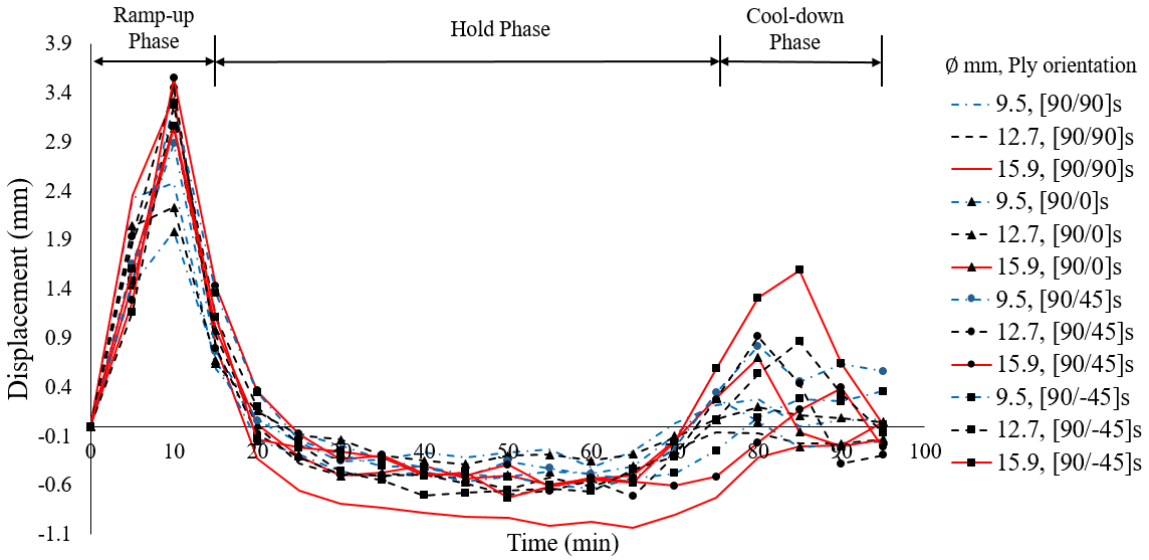

Figure 5.9 Average Z-displacement for all sample configurations through the three stages of curing.

The average strain in X and Y directions is highest for mold configuration 3 and least for mold configuration 1 across all the samples. Note that mold configuration 3 has the highest radius of curvature and the largest unsupported laminate area. Also, the strain in X-direction is more than the strain in Y-direction for all the samples. In X-direction, an average strain of 19.38 µm/mm is highest for the combination of mold 3 and $[90/-45]_s$ layup, and 4.51 µm/mm is lowest for the combination of mold 1 and $[90/45]_s$ layup. This difference between the $[90/-45]_s$ and $[90/45]_s$ layups is primarily due to the directional loading caused by the location of the vacuum source as shown in Figure 5.1. During the ramp-up, as the temperatures increase to the gel-point, the friction between plies reduces and the plies readjust to the autoclave conditions. Only in this phase, the directional loading due to the location of the vacuum source causes the difference in movement

between the $[90/-45]_s$ and $[90/45]_s$ layups. The change in strain after the ramp-up during the hold phase is relatively similar in the different layups.

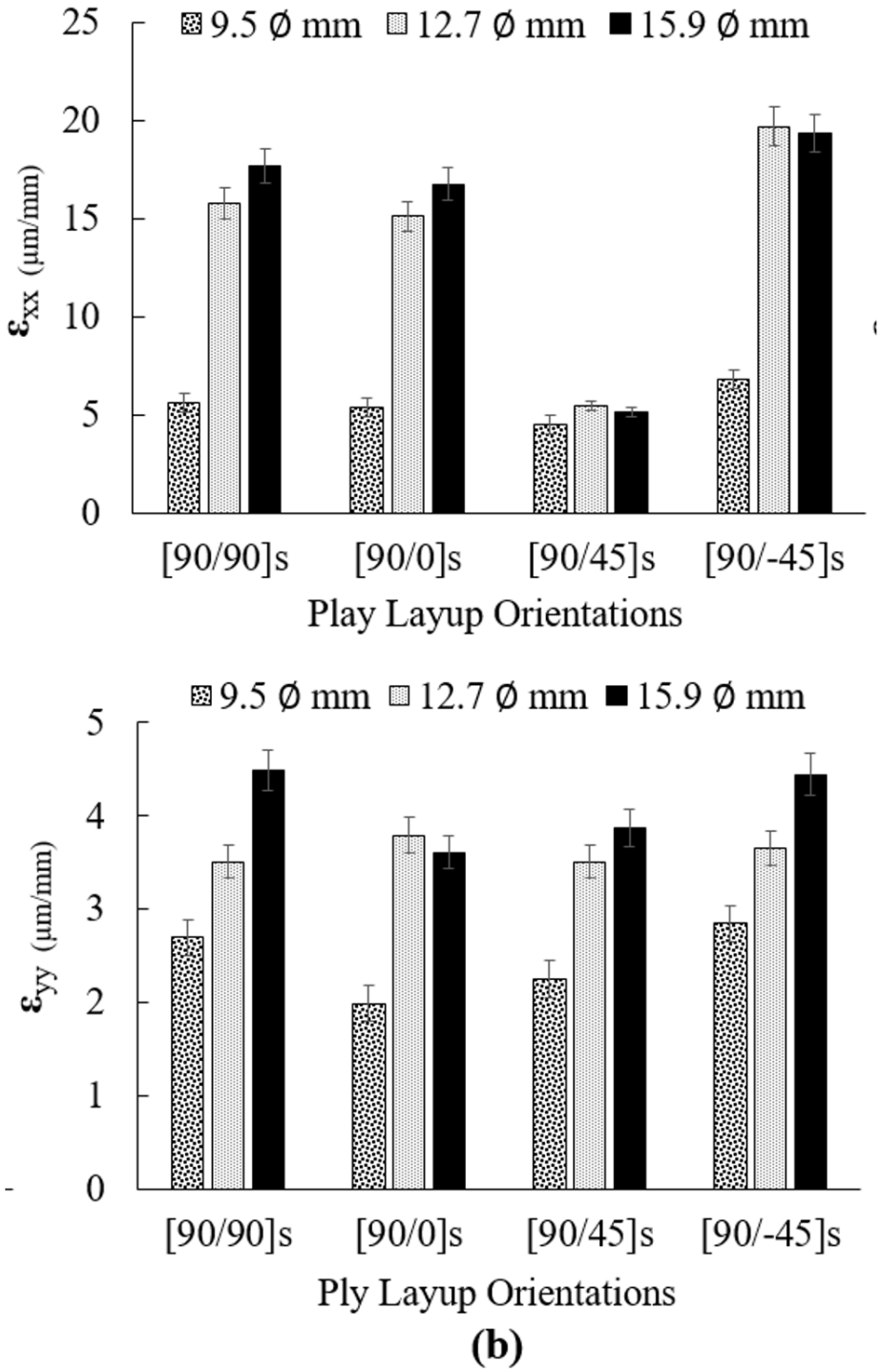

Figure 5.10 (a) Average in-plane strain in the X direction and (b) for the Y direction.

In Y-direction, the highest strain of 4.48 µm/mm is observed for mold 3 and $[90/90]_s$ layup, and the lowest average strain of 1.99 µm/mm is observed for mold 1 and $[90/0]_s$ layup. These results show that the strain produced by the ply movement increases with an increase in the radius of the curvature of the tool.

The out-of-plane ply displacement in Z-direction averaged over the region of interest is shown in Figure 5.11. The negative displacement in this plot indicates ply shrinkage after cure. The average displacement for mold 3 in $[90/90]_s$ and $[90/-45]_s$ is positive due to the high number of wrinkles that are observed in these two layups. In general, higher shrinkage is observed in $[90/0]_s$ layup and lower shrinkage is observed for $[90/-45]_s$ layup. In terms of mold configuration, shrinkage is high for mold 1 and it is low for mold 3. The highest shrinkage of -0.07 mm and -0.069 mm is observed for $[90/0]_s$ layup for mold 2 and mold 1 respectively. The lowest shrinkage is observed for $[90/-45]_s$ layup of mold 3.

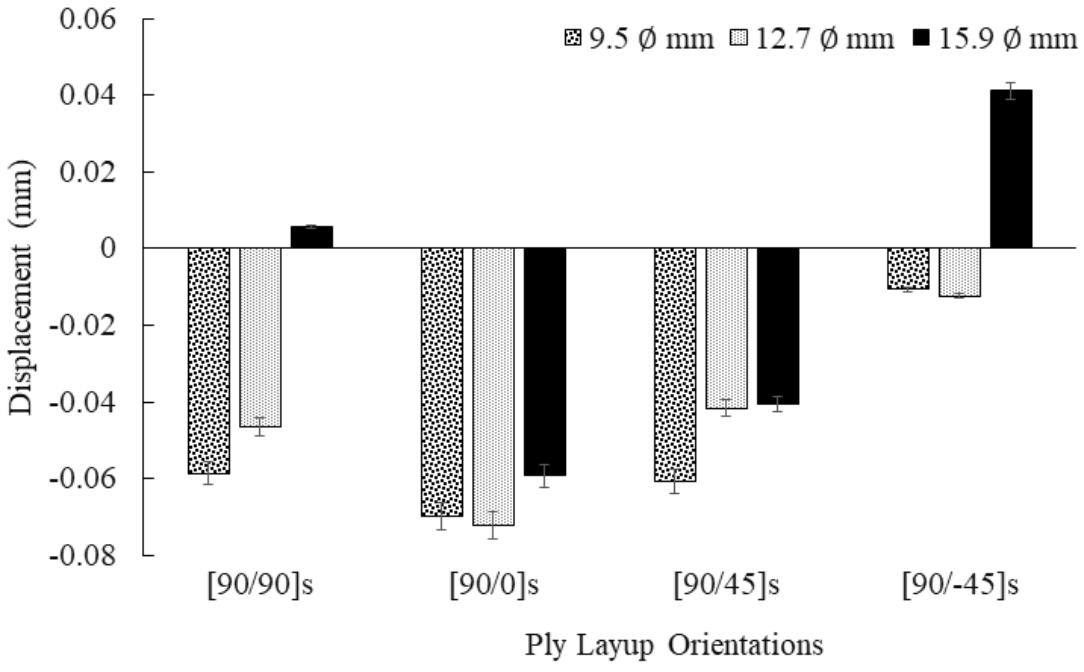

Figure 5.11 Average out-of-plane ply-movement in the Z-direction.

5.2.3. In Situ Examination of Wrinkle Formation

The maximum average Z-displacement at the wrinkle (height of the wrinkle) is plotted for three configurations of the cylindrical tool molds (9.5 mm, 12.7 mm, and 15.9 mm) in all four layups in Figure 5.12. It can be observed that the biggest wrinkles are observed for mold 3 with a 15.9 mm diameter cylindrical tool and the smallest wrinkles are observed for mold 1 with a 9.5 mm cylindrical tool for all layups. Among the different layups, $[90/-45]_s$ has the highest tendency for wrinkle formation, and $[90/0]_s$ has a relatively lower propensity for wrinkle formation. In general, for all the sample configurations, more wrinkles are observed for mold with a higher radius of curvature, and fewer wrinkles are observed for mold with a lower radius of curvature. From Figure 5.12, it can be observed that the highest wrinkle of 1.5 mm is observed for the combination of mold 3 and $[90/-45]_s$ layup.

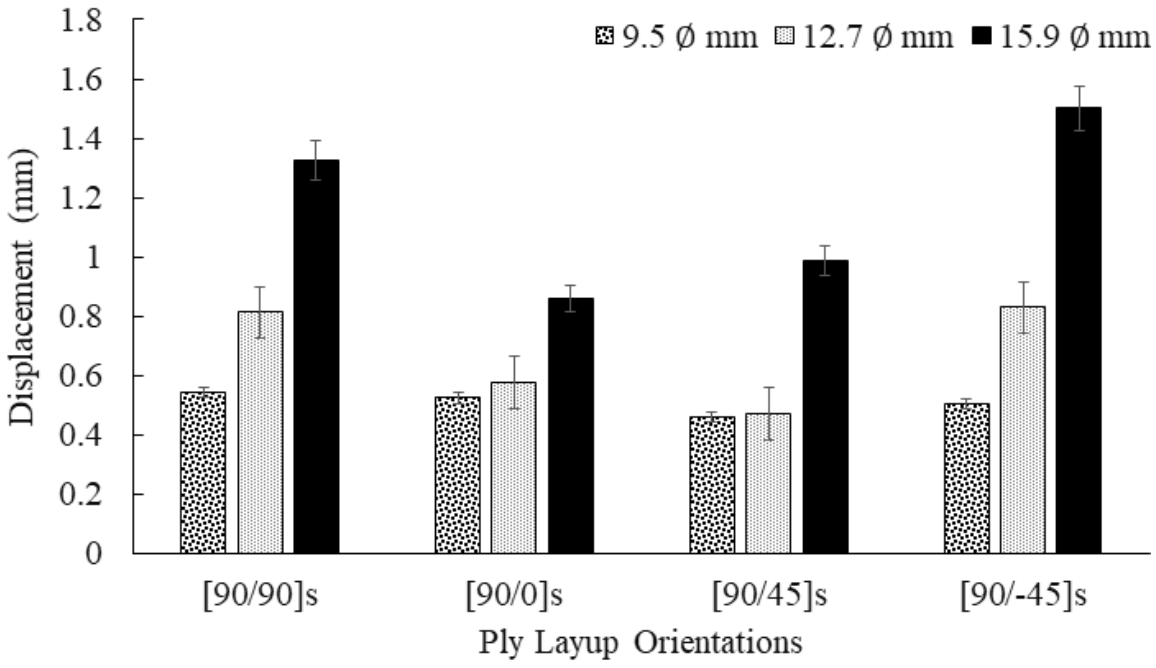

Figure 5.12 The average height of the biggest wrinkle for all layups.

5.2.4. Ex Situ Characterization & Correlation

The X-ray reconstructed post-curing images of the samples are correlated with the last stages of in-situ interface movement measurements obtained during the processing. Figure 5.13 shows a 4-ply $[90/-45]_s$ laminate fabricated with the cylindrical tool of diameter 15.9 mm. The red box on the right DIC contour in Figure 5.13 represents the area of the specimen used for X-ray characterization. The height of the delaminated wrinkle measured through the in-situ DIC analysis and the ex-situ micro-CT is measured to be 1.5 mm in both cases.

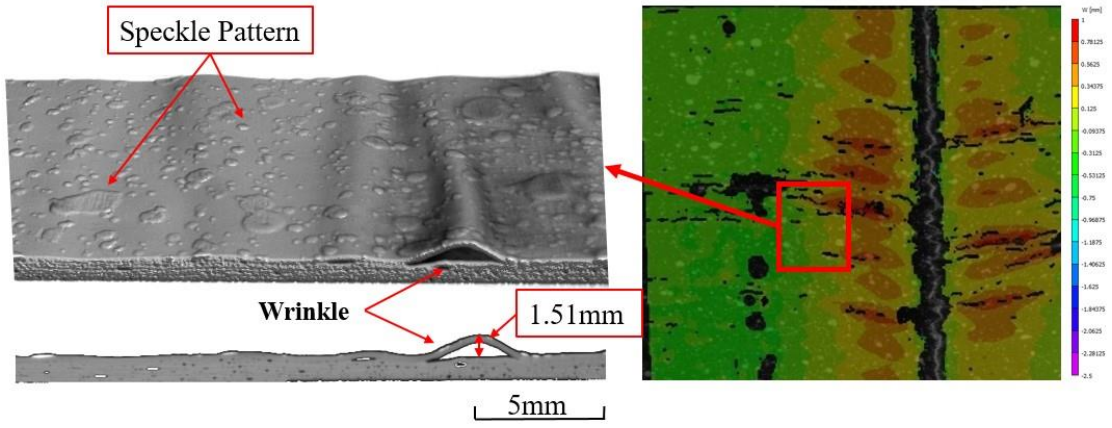

Figure 5.13 X-ray and DIC contour for the same wrinkle of height 1.51 mm observed in a 4-ply $[90/-45]_s$ laminate fabricated using the cylindrical tool of diameter 15.9 mm.

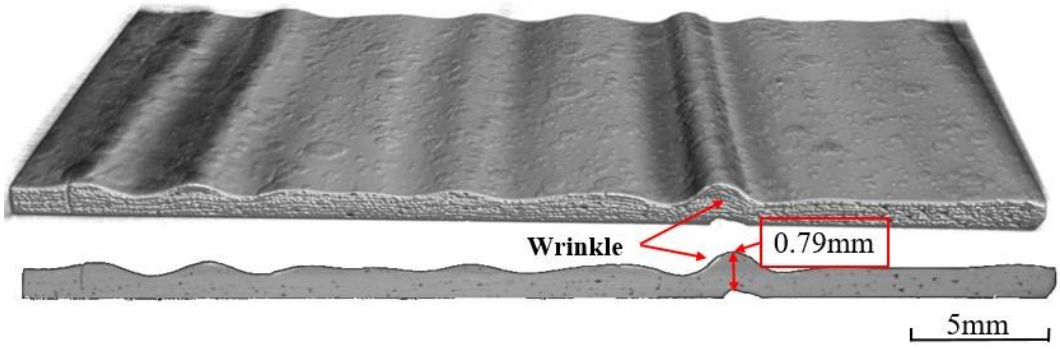

Figure 5.14 Wrinkle of 0.79mm height for a 4-ply $[90/-45]_s$ laminate fabricated using the cylindrical tool of diameter 12.7mm.

A through-thickness wrinkle without any delamination can be seen in Figure 5.14. The X-ray measured the height of the wrinkle to be 0.79 mm for a 4-ply $[90/-45]_s$ laminate fabricated with the cylindrical tool of diameter 12.7 mm. The specimen in Figure 5.14 similar to Figure 5.13 is obtained from the flat region of the cured laminate.

Figure 5.15 and Figure 5.16 show the X-ray image of the specimen from the curved part of the sample. Figure 5.13 shows the two specimens fabricated with the same $[90/-45]_s$ layup over two different molds created with the cylindrical tools of diameter, 15.9 mm (a) & 12.7 mm (b). For 15.9 mm, the delamination under the wrinkle is measured to be 1.32 mm and for the 12.7 mm tool, it is 0.79 mm. Figure 5.16 (a) and (b) show two specimens fabricated with the same mold created with the cylindrical tool of diameter 15.9 mm but for two different layups of $[90/-45]_s$ and $[90/90]_s$ respectively. In this case, the height at the wrinkle is measured to be 1.51 mm for $[90/-45]_s$ and 1.31 mm for $[90/90]_s$. These X-ray results correlate well with the in-situ measurements (1.50 mm and 1.32 mm respectively) plotted in section 3.3 validating the in situ experimental approach.

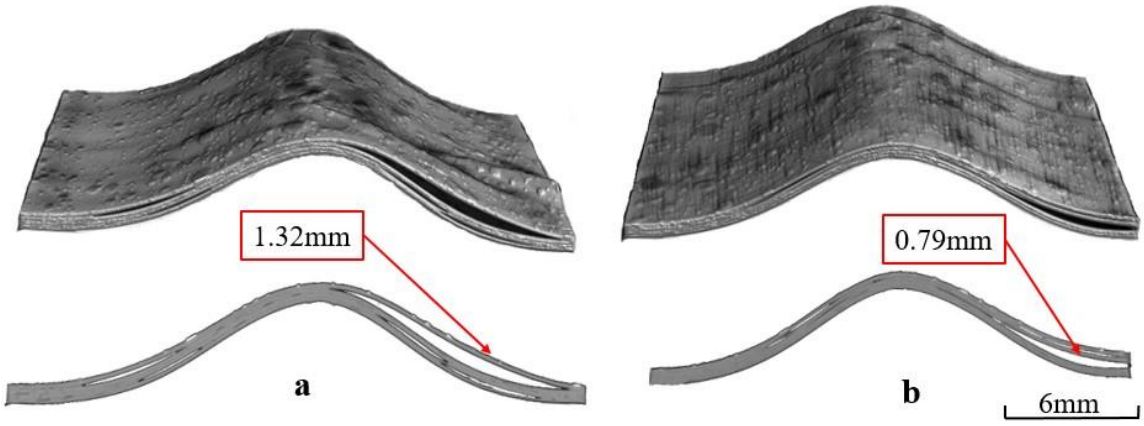

Figure 5.15 Laminate fabricated with $[90/-45]_s$ layup using the cylindrical tools of diameter, (a). 15.9 mm; (b). 12.7 mm.

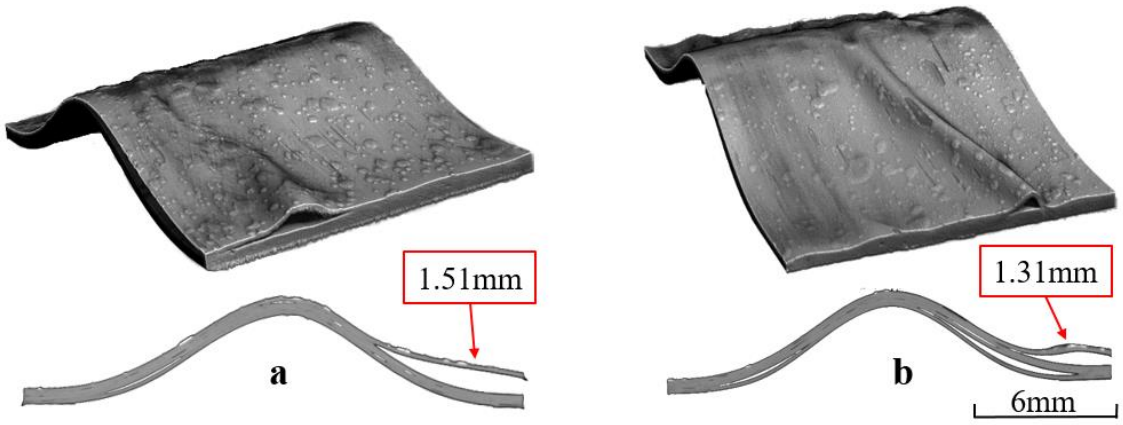

Figure 5.16 Laminate fabricated with the cylindrical tool of diameter15.9 mm for, (a). $[90/-45]_s$ layup (b). $[90/90]_s$ layup.

5.2.5. Discussion

Thickness variations are often observed during the manufacture of composite parts with complex curvatures. Levy and Hubert measured a 40% compaction pressure drop in the curved regions with an L-shaped mold (Levy et al., 2014; Levy & Hubert, 2019). This results in the thickness variations due to differences in reaction stress between the flat and curved surfaces. Researchers often use L-sections with reference to curvature, but the mold used in the current work with a cylindrical rod affixed on a flat plate exaggerates the effect of compaction pressure changes, due to the unsupported region (Fiorina et al., 2017; Geleta et al., 2018; Jung et al., 2015).

While one reason for the thickness variation in the cured part is geometry, there is also a contribution of inter-ply friction. Ply friction varies due to viscosity changes during cure which aids in the movement of plies (Alshahrani & Hojjati, 2017; Lee et al., 2017). According to Levy et al., (2019) inter-ply friction preventing adequate conformations of the plies together, or plies against the mold also lead to varying thickness at the

curvature. They used the conformation number (Λ) to describe whether the compaction is friction or pressure-dominated (Levy et al., 2014). The confirmation number Λ is calculated as the ratio of tension in the first ply (f_1) and the frictional force (f_1^{max}) in the layup. This f_1 is the same as circumferential stress considering the ply layup is thin-walled as shown in Figure 5.17 (a). Here, 'r_m' is the radius of the cylindrical tool in the mold, 't_i' and 't_f' are the average initial and final thickness at the flange region of the sample, and 'c_i' and 'c_f' are the average thickness of the sample at the unsupported region before and after cure. Consider that the unsupported region with the radius of curvature r, section length L_{cs} is subject to a pressure P. Then f_1 can be written as follows:

$$f_1 = \frac{P\rho L_{cs}}{c_i} \tag{5.1}$$

The friction limit f_1^{max} is defined by Levy et al. (Levy & Hubert, 2019) using a Coulomb friction model with the friction coefficient μ and flange length L_f.

$$f_1^{max} = \mu L_f P \tag{5.2}$$

The confirmation number Λ can then be obtained as follows:

$$\Lambda = \frac{f_1}{f_1^{max}} = \frac{P\rho}{\mu L_f P c_i} = \frac{\rho L_{cs}}{\mu L_f c_i} \tag{5.3}$$

Using the geometric measurements from current experiments and a range of friction coefficients varying from 0.17 to 0.36 for different layups and conditions from the literature, we obtain the conformation number as less than one for all cases, indicating that the compaction at the curvature is always friction dominated (Levy & Hubert, 2019; Xiao et al., 2000).

The thickness at the unsupported region in all the samples, before and after processing is measured and used to compute the thickness variation as shown in Equation 5.4 below. The data is averaged for all the samples and is presented in Table 5.1.

$$\delta t(measured) = \frac{c_f - c_i}{c_i} x100 \tag{5.4}$$

Table 5.1 shows the relative thickness variation measured for three mold configurations from initial ply lay-up to the final part after cure. The least thickness variation of 6.87 % (0.11 mm) is observed at the curvature for $[90/45]_s$ layup of mold 1 (9.5 mm), and the highest thickness variation of 31.25 % (0.5 mm) is observed for $[90/-45]_s$ layup for mold 3 (15.9 mm). These measurements along with the DIC data for ply wrinkles are plotted in *Figure 5.18* and it can be observed that the thickness variation and ply wrinkles are closely related. Throughout Table 5.1, it can be noticed that the final thickness at the curvature 'c_f' is higher than 'c_i' for all mold configurations which is due to the compaction pressure difference at the unsupported region. This thickness variation from the flange region to the curvature region progresses to the formation of a waviness defect pattern in the flat part of the sample as shown in Figure 5.14 later progressing to wrinkles. In general larger wrinkles and more average ply movement is observed for configurations with higher.

Laying up over a mold with radius creates ply bending which results in compression loads at the inner plies (Hallander et al., 2013). The resulting thermal stresses are relaxed by inter-ply slippage at resin-rich areas under curvature as there is no support for the plies in this region. The process of stress relaxation and ply-slippage towards the end of the cure can be observed in the experimental results as shown in Figure 5.5. The thickness variations, change in friction, and the thermal stress relaxation all together contributes to

the formation of wrinkles on the top ply of the curved section, eventually leading to the delamination of the internal plies as shown in Figure 5.16.

Table 5.1

Initial and final ply geometry for three mold configurations

Orientation	$\mathbf{r_m}$ (mm)	$\mathbf{c_i}$ (mm)	$\mathbf{c_f}$ (mm)	δt (Measured)
$[90/90]_s$	4.75	1.6	1.8	12.5 %
$[90/0]_s$			1.85	15.625 %
$[90/45]_s$			1.71	6.875 %
$[90/-45]_s$			1.9	18.75 %
$[90/90]_s$	6.35	1.6	1.95	21.875 %
$[90/0]_s$			1.86	16.25 %
$[90/45]_s$			1.71	6.875 %
$[90/-45]_s$			2.01	25.625 %
$[90/90]_s$	7.95	1.6	1.96	22.5 %
$[90/0]_s$			1.87	16.875 %
$[90/45]_s$			1.72	7.5 %
$[90/-45]_s$			2.10	31.25 %

Shear of plies due to unsupported regions (A1, A2 & A3) underneath the plies as shown in Figure 5.17 (b) necessitates higher ply adjustment during the ramp-up phase of cure. This is a primary reason for the higher strain in X-direction compared to Y-direction in the ramp-up phase. Hallander et al (2013) observed that ply orientation also affects the shear of plies, with [45/0/-45] having less shear compared to [45/-45/0] and [45/-45]. In the current paper, the effect of 45 and -45 oriented plies can be observed in Figure 5.10 with maximum strain in X-direction for [90/-45] and least strain in X-direction happening for [90/45] layup. Hallander et al. (2015) found that [90/0] interfaces

will decrease the formation of wrinkles due to the cross-ply nature of the ply layup. In the current work, we have also observed fewer and smaller wrinkles for $[90/0]_s$ layup compared to other layups as seen in Figure 5.11.

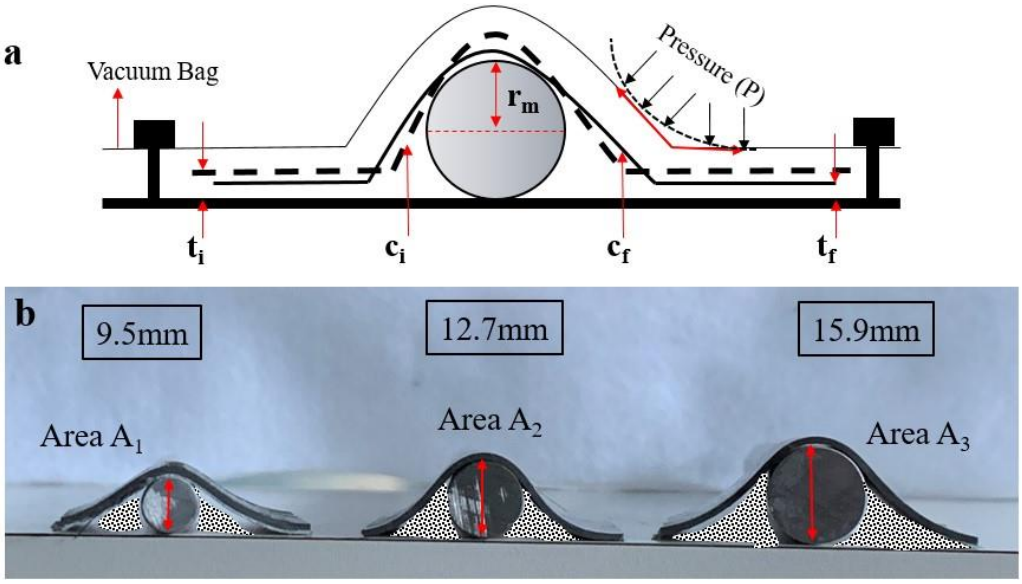

Figure 5.17 (a) Schematic showing ply layup and mold geometry; (b) Unsupported area in the three mold configurations.

Lightfoot et al observed that physically large wrinkles are frequently observed in laminates with 90° plies surrounded by 45° plies (Lightfoot et al., 2013) they believe that an increase in the shear stress due to the mechanical interlocking of 90° and 45° plies leads to the fiber friction and formation of wrinkles. In the current work, the higher strain in X-direction coupled with $[90/-45]_s$ layup orientation leads to large wrinkles. Other factors like the coefficient of thermal expansion mismatch between aluminum mold and carbon fiber prepreg sample will further aid in the formation of wrinkles on the top surface ply and delamination in the interior plies. As previously discussed in Section 4.3, the ply interfaces of a regular woven carbon fiber fabric are modified by growing ZnO

nanorods. These modified plies along with the desized plies are laid upon the cylindrical tool as shown in the schematic Figure 5.17 to study the effect of nanofillers on the ply movement. The same experimental approach as discussed in Section 5.1.3 is used to analyze the in-situ cure strains.

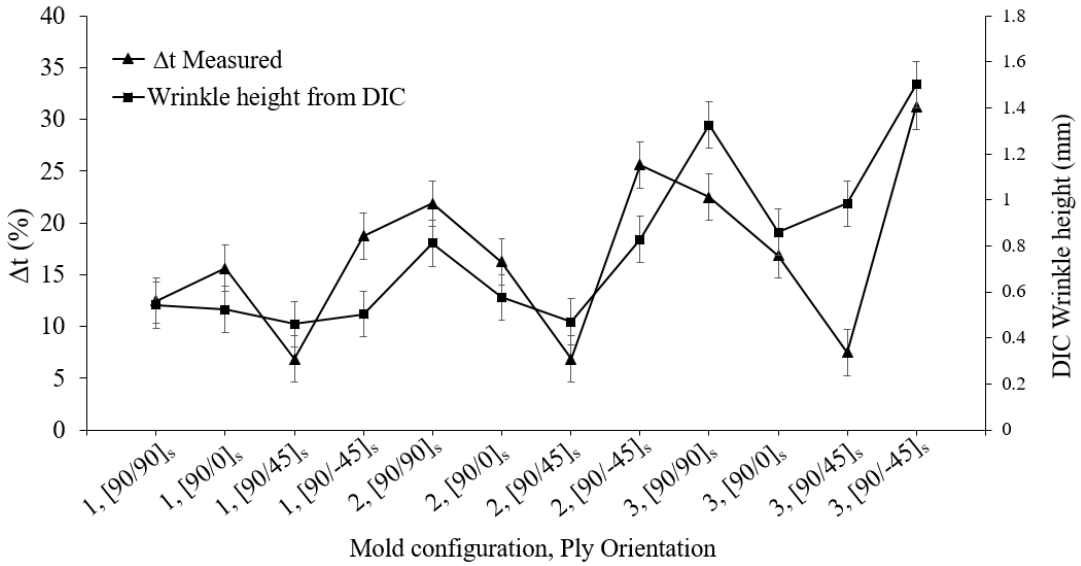

Figure 5.18 Comparison of the relative thickness variation and wrinkle height.

The in-plane strain results in X and Y directions from the DIC are plotted in Figure 5.19 for both desized (DS) and ZnO specimens. In this preliminary result, the highest strain is observed for the desized sample in the X direction followed by the Y direction. A huge reduction in strain can be observed for the ZnO sample in both X and Y directions for the same experimental setup. These results show that the plies modified using ZnO nanorods have the potential to decrease ply movement which in turn reduces the processing induced defects. Further detailed analysis is required to effectively gauge the ability of the nanofillers in reducing the ply movement.

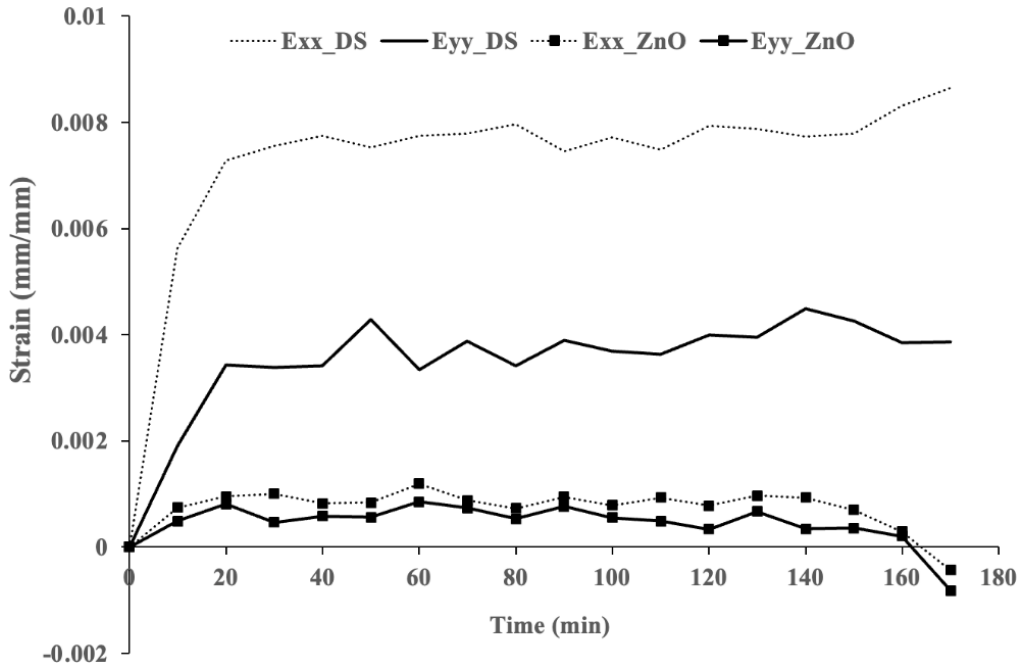

Figure 5.19 Comparison of strain between DS and ZnO samples over the cylindrical tool.

5.3. Summary

In this chapter, the kinematics of ply interfaces during composite manufacturing is investigated by developing a novel in-situ experimental approach. A specially designed autoclave with borosilicate glass viewports is incorporated with a 3D Digital Image Correlation (DIC) camera setup to capture pictures of the speckle pattern applied on top of the composite prepreg laminate while it is being cured. Both in-plane strains and out-of-plane ply movements are quantified through the cure cycle programmed into the autoclave. The processing induced defects in the composite laminate are further characterized by X-ray micro-computed tomography (micro-CT) after complete cure. Ply interfaces are then modified by growing ZnO nanorods on the carbon fiber and the effect of these nanorods on the ply movement is discussed. The main research findings are summarized below:

A. The in-situ DIC-based approach is an effective method to measure ply movement and defect formation during cure. The post-situ X-ray measurement of wrinkle and delamination dimensions correlate well with the last stages of in-situ measurements.

B. The mold configuration with the larger radius of curvature (15.9 mm tool) leads to higher strains in both in-plane directions and higher displacement in the out-of-plane direction. The maximum out-of-plane ply movement is observed for $[90/-45]_s$ layup orientation due to mechanical interlocking of plies.

C. The mold configuration with a smaller radius of curvature (9.5 mm tool) coupled with $[90/0]_s$ layup orientation has the smallest out-of-plane movement due to the cross-ply nature of the ply layup.

D. The friction-dominated mold layup in conjunction with the higher unsupported region at the curvature for mold with a 15.9 mm generated the highest ply movement, resulting in the formation of large wrinkles and delamination.

E. Modified ply interfaces by growing ZnO nanorods show potential to reduce the ply movement during cure.

The experimental approach developed in this chapter can be used to quantify the behavior of the ply interfaces during manufacturing and could help devise approaches to reduce manufacturing defects in composite structures.

6. Thermo Mechanical Modeling of Composite Cure

This chapter focuses on modeling the cure phenomenon inside an autoclave and presents a cure design technique to reduce the processing induced strains/stresses. The results of this model are benchmarked against experimental results. The cure kinetics of the thermoset matrix inside the carbon fiber prepreg is calculated through reaction kinetic equations parameterized by DSC characterization. These matrix properties along with the fiber properties are used in developing a thermomechanical finite element model. A four-ply model is developed with several symmetric and asymmetric layups and the results are compared against experimental data. Several cure cycles using abrupt cooling operation are studied to design a low residual stress processing method. The thermomechanical model accurately predicted the evolution of processing induced strains during cure and deformations post-cure. This model can also be applied to other thermoset matrix materials to predict and reduce processing induced strains/stresses.

6.1. Thermal characterization

6.1.1. Materials

Unidirectional carbon fiber prepreg procured from Fibre Glast Corporation contains 12K tow raw material with manufacturer specified tensile modulus of 275.8 GPa (40 msi) and strength of 5.65 GPa (820 ksi). This prepreg is pre-impregnated with an epoxy resin system of the density of 1.2g/cc and has a fabric areal weight of 139 gsm. Resin samples of weight 25 mg to 35 mg were extracted by scraping from the prepreg for cure kinetics. The manufacturer recommended curing temperature of the prepreg is 120 °C (248 °F) with a 1 hr. hold time.

6.1.2. Differential Scanning Calorimetry

The curing thermal data were obtained through Differential scanning calorimetry (DSC) using DSC-3 from Mettler Toledo. The resin is heated from -25ºC to 250ºC with three different heating rates of 5ºC/min, 10ºC/min, and 15ºC/min in an inert nitrogen atmosphere. Resin samples extracted by scraping from the prepreg were placed and sealed in 40 µL aluminum crucibles. These crucibles are placed in DSC-3 with a constant 10 ml/min flow of nitrogen for characterization. An empty crucible is used as a reference for all the tests. The heat flow data is obtained as a function of temperature and time using the area under the peak of the exotherm. This data is processed further to obtain the degree of cure (DOC) of the resin. DSC works on the basic assumption that the rate of the kinetic process ($d\alpha/dt$) is proportional to measured heat flow (ϕ) shown in Equation 6.1 (Roşu et al., 2002).

$$\frac{d\alpha}{dt} = \frac{\phi}{\Delta H} \tag{6.1}$$

Where α is the DOC and ΔH is the enthalpy of the curing reaction.

6.2. Composite Cure Modeling

During the high-temperature curing process, the epoxy matrix is involved in an exothermic reaction. Therefore, the energy equation for the autoclave curing of thin structures with a non-linear internal heat generation term can be expressed as:

$$\rho C_p \frac{\partial \theta}{\partial t} - K_x \frac{\partial^2 \theta}{\partial x^2} - K_y \frac{\partial^2 \theta}{\partial y^2} = \rho_m H_m V_m \frac{\partial \alpha}{\partial t} \tag{6.2}$$

Where θ is the temperature, ρ and C_p are the density and specific heat of the composite, K_x, and K_y are the thermal conductivities. ρ_m, H_m, V_m are the density, heat of reaction, and volume fraction of the epoxy matrix, α is the degree of cure. The density of the composite, ρ and epoxy matric density can be expressed as follows:

$$\rho = (1 - V_m)\rho_m + V_m\rho_f \tag{6.3}$$

$$\rho_m = \alpha\rho_m^c + (1 - \alpha)\rho_m^u \tag{6.4}$$

Where, ρ_f is the density of fiber, ρ_m^c and ρ_m^u are cured and uncured epoxy matrix densities correspondingly. The specific heat capacities of the composite material and the epoxy matrix can be calculated similarly as follows:

$$c = (1 - V_m)c_m + V_m c_f \tag{6.5}$$

$$c_m = \alpha c_m^c + (1 - \alpha)c_m^u \tag{6.6}$$

Where, c_f is the specific heat of fiber, ρ_m^c and ρ_m^u are cured and uncured epoxy matrix-specific heat correspondingly.

The rate of the cure considered to be a kinetic process is often phenomenologically expressed in terms of a temperature-dependent reaction rate $K(\theta)$, and a dependent kinetic model function $f(\alpha)$ as shown in Equation 6.7 (Yousefi et al., 1997).

$$\frac{d\alpha}{dt} = K(\theta)f(\alpha) \tag{6.7}$$

The reaction rate constant $K(\theta) = Ae^{-x}$, in which A is the pre-exponential factor and $x = E_a/R\theta$ is the reduced activation energy. Where, E_a is the activation energy, R is the universal gas constant. Most of the reactions studied through thermal analysis can be described using Equation 6.7 and it is therefore important to find both $K(\theta)$ and $f(\alpha)$ to understand the kinetics behind the cure phenomenon.

The activation energy E_a can be determined by using the iso-conversional method (Vyazovkin, 1997) using the logarithmic form of Equation 6.7 as shown below:

$$\ln\left(\frac{d\alpha}{dt}\right) = \ln\left(Ae^{-\frac{E_a}{RT}}f(\alpha)\right) \tag{6.8}$$

$$\ln\left(\frac{d\alpha}{dt}\right) = \frac{-E_a}{R}\left(\frac{1}{\theta}\right) + \ln\left(Af(\alpha)\right) \tag{6.9}$$

Activation energy can be determined from the slope of the plot $\ln(d\alpha/dt)$ versus $(1/\theta)$ for the same value of α.

The values of the activation are used in identifying the appropriate kinetic model for the resin used in the prepreg. Some of the most frequently cited basic kinetic model functions are the Johnson-Mehl-Avrami model (JMA(n)) (Fanfoni & Tomellini, 1998), 2D and 3D-reaction models (R2 & R3) (Málek, 1992), Ginstling-Broumshtein model (D4) (Ginstling & Brounshtein, 1950), etc. The exponent *n* in the Johnson-Mehl-Avrami model depends on the mechanism of the nucleation-growth process and it remains constant for a given reaction (Arshad & Maaroufi, 2015). To find the kinetic model that best describes the measured set of thermal analysis data, two special functions $y(\alpha)$ and $z(\alpha)$ are defined which can easily be obtained through the experimental data.

$$y(\alpha) = \left(\frac{d\alpha}{dt}\right)e^{x} \tag{6.10}$$

$$z(\alpha) = \pi(x)\left(\frac{d\alpha}{dt}\right)\left(\frac{\theta}{\beta}\right) \tag{6.11}$$

Where β is the heating rate (K/min) and $\pi(x)$ is the expression of the temperature integral which can be approximated using the 4th rational expression of Senum and Yang as in Equation 6.12 (Pérez-Maqueda & Criado, 2000).

$$\pi(x) = \frac{x^3+18x^2+88x+96}{x^4+20x^3+120x^2+240x+120} \tag{6.12}$$

Plotting the function $y(\alpha)$, normalizing within the (0,1) interval gives the shape of the function and as $y(\alpha)$ is proportional to the $f(\alpha)$ function, this plot is also the shape of the function $f(\alpha)$. The shapes and maximums of both these functions are used in

determining the appropriate kinetic model function (Koga & Malek, 1996). Using the value of the activation energy and the kinetic model function, the value of the pre-exponential factor (*A*) is calculated using the following equation:

$$A = -\frac{\beta x_p}{\theta f'(\alpha_p)} e^{x_p} \tag{6.13}$$

Where, $f'(\alpha_p)$ is the differential form of the kinetic model $[df(\alpha)/d\alpha]$, α_p is the conversion corresponding to the maximum on the DSC curve and p is the maximum of the DSC curve. The cure kinetics results are discussed in Section 6.3

6.2.1. Finite Element Modeling

The PDE in Equation 6.2 can be discretized using Finite Element Analysis (FEA) and combined with mechanical analysis to estimate the deformations and residual stresses during curing. In this research, a mechanical model from Ansys Composites PrepPost (ACP) in combination with the transient thermal model from Ansys Composite Cure Simulation (ACCS) was adopted for the FEA model. The required composite material data for the cure simulation is fed in the engineering data unit of the model. Solid 2480 elements were used to model the four-ply composite laminate. Figure 6.1 (a) shows the schematic sketch of the specimen for the curing process in an autoclave along with the applied boundary conditions for the FEA simulation. For this simulation, the four-ply prepreg sample is vacuum bagged and a convection temperature profile is applied for the curing. This temperature is varied based on the cure cycle, so the convective heat transfer boundary condition was considered for the FEA simulation. The dimensions and the layup of the composite correspond to the in-situ experiments in Chapters 3 and 4. Uniform pressure is applied to simulate vacuum in the experiments. The experimentally determined heating rate and the autoclave temperature profiles from Chapters 3 and 4 are

incorporated as an input to the finite element model. The temperature profile consists of three steps, a gradual temperature increase at a constant rate of 4.75^{o}C/min followed by isothermal heating, and post-cooling as shown in Figure 6.1 (b). For simulating the entire curing process, the material state, glass transition temperature, and heat of reaction are obtained from the DMA and DSC of the resin. The cure kinetic equations are used to obtain the results such as Degree of Cure (DOC), activation energy, pre-exponential factor, '*m'*, and '*n'*. The rest of the material properties associated with fiber such as Young's modulus, Poisson's ratio, and shear modulus are provided by the prepreg manufacturer. The in-situ strain data as a function of temperature is used in calculating the coefficient of thermal expansion (CTE) (Schulz et al., 2005). Table *6.1* illustrates all the material properties associated with the prepreg used in the simulations.

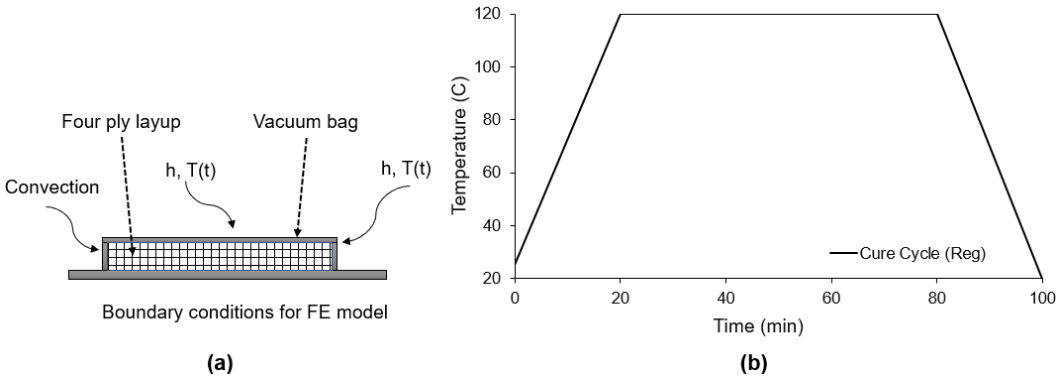

Figure 6.1 Temperature profile incorporated into the finite element model.

A convergence study on the ACCS model was carried out to determine an appropriate mesh density. The laminate with the same material properties was modeled with decreasing size of the elements 20 mm, 10 mm, 5 mm, and 2 mm. The convergence of the results is obtained with the element size of 5 mm which gives 2480 elements and 3360 nodes. The model with an element size of 2 mm with 15504 elements and 20020

nodes had a negligible effect on the deformation of the laminate. Adaptive mesh refinement with five max refinement loops and a refinement depth of three was also used for the analysis.

Table 6.1

Material properties for carbon fiber prepreg used in this research

Material Property	Value	Unit
Density	1200	Kg m^{-3}
Coefficient of Thermal Expansion		
i. X-Direction	1.2E-20	$^oC^{-1}$
ii. Y-Direction	2.4E-06	$^oC^{-1}$
iii. Z-Direction	2.4E-06	$^oC^{-1}$
Youngs Modulus		
i. X-Direction	2.758E+11	Pa
ii. Y-Direction	7.9E+09	Pa
iii. Z-Direction	7.9E+09	Pa
Poisson's Ratio		
i. XY	0.35	
ii. XY	0.45	
iii. XY	0.35	
Shear Modulus		
i. XY	5E+09	Pa
ii. XY	3.27E+09	Pa

6.3. Results & Discussion

6.3.1. Reaction Kinetics

The curing reaction of the epoxy resin in the prepreg was investigated by DSC at three different heating rates as shown in Figure 6.2. The variation of the fractional conversion as a function of temperature for the epoxy resin can be seen in this Figure 6.3.

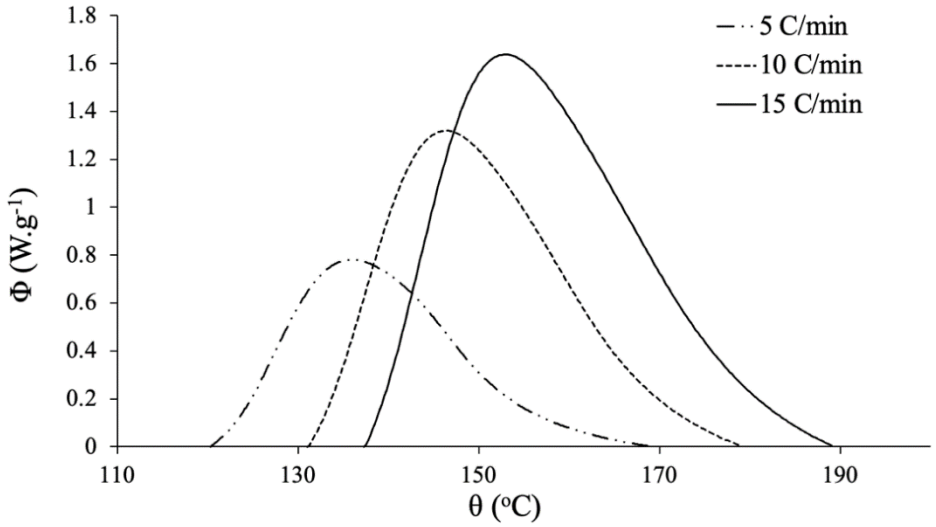

Figure 6.2 Measured heat flow for different heating rates.

The data from the DSC for the respective α is used in Equation 6.10 to plot the Arrhenius equation for the cured resin samples as shown in Figure 6.4. The slope of these straight lines gives the value of activation energy (E_a). This activation energy is used in the calculation of both $y(\alpha)$ and $z(\alpha)$ functions using Equations 6.12 and 6.13 respectively.

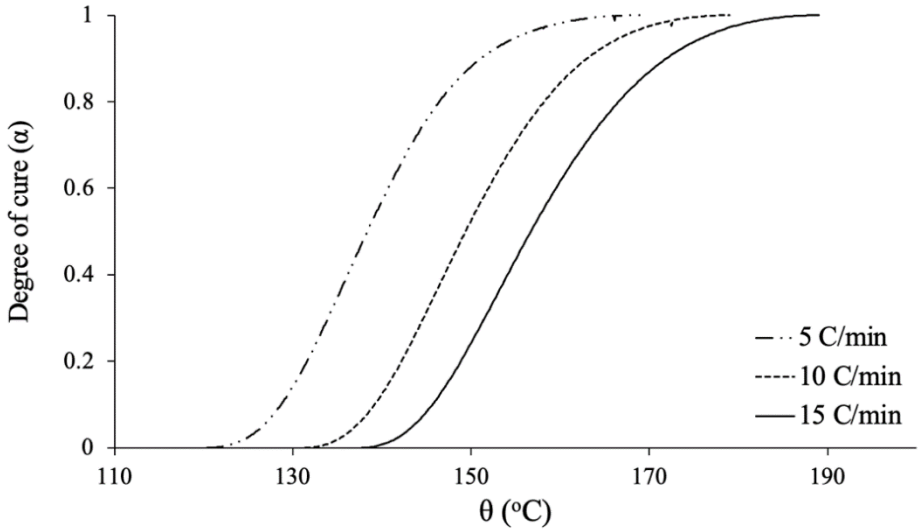

Figure 6.3 Degree of cure for different heating rates.

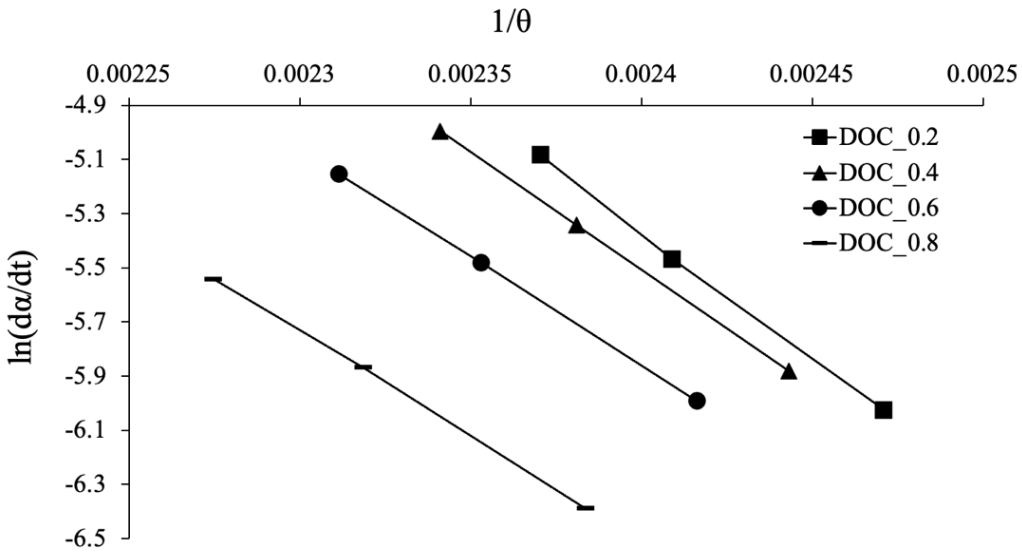

Figure 6.4 $ln(d\alpha/dt)$ vs. $(1/\theta)$ for $\alpha = 0.2, 0.4, 0.6$ & 0.8.

Figure 6.5 shows the normalized plot of the function $y(\alpha)$. Similar to Figure 6.5, the normalized variation of function $z(\alpha)$ plot with the degree of cure can be seen in Figure 6.6. Table *6.2* lists the values of the maxima of both the functions $y(\alpha)$ and $z(\alpha)$ at α_M and α_p^{∞} respectively and the α_p is taken as the maximum of the DSC peak.

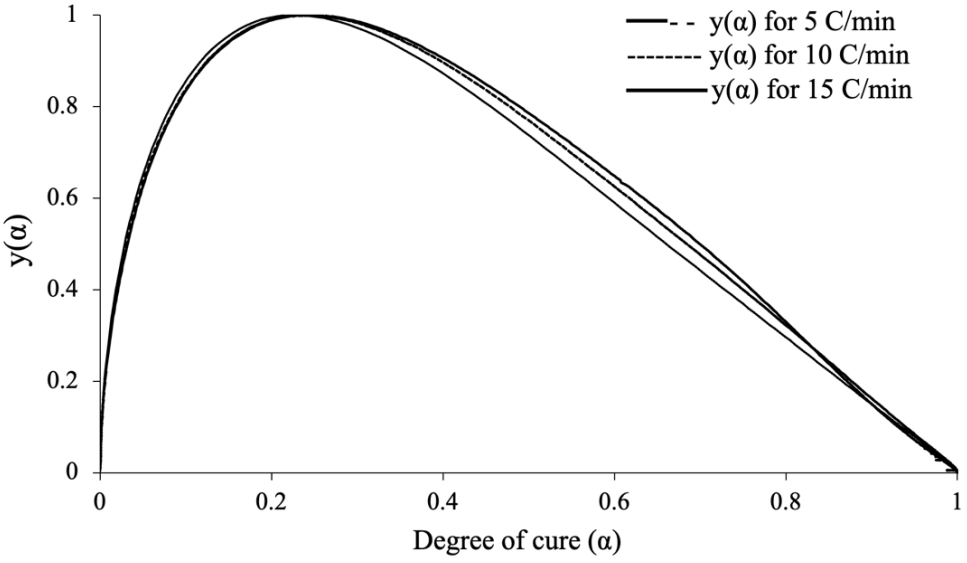

Figure 6.5 Function $y(\alpha)$ vs. degree of cure (DOC).

Table 6.2

Peak values of the function and respective temperature

Heating Rate (β)	α_M	α_p^∞	α_p	θ
5	0.2457	0.4096	0.3609	409.06
10	0.2327	0.3937	0.3723	419.32
15	0.2147	0.3779	0.3583	425.9

From Table *6.2* the trend indicates that the curing process of the resin in the prepreg can be described using the two-parameter autocatalytic kinetic model Sestak-Berggren (SB) as shown in Equation 6.16 (Montserrat & Málek, 1993).

$$f(\alpha) = \alpha^m(1-\alpha)^n \tag{6.16}$$

Where *m* and *n* are the kinetic exponents where kinetic parameter ratio *p* is $p = m/n$. The value of *p* is calculated using the maxima of function $y(\alpha)$ as $p = \alpha_M/(1-\alpha_M)$. The value of the kinetic parameter *n* for various heating rates is obtained by the slope of the linear dependence $\ln\left[\left(\frac{d\alpha}{dt}\right)e^x\right]$ versus $\ln[\alpha^p(1-\alpha)]$ (Yinnon & Uhlmann, 1983). The values of *p, n,* and *m* for all three heating rates can be seen in Table 6.3.

Table 6.3

Kinetic exponents calculated for various heating

Heating Rate (β)	α_M	*p*	x_p	*n*	Mean *n*	*m*	Mean *m*
5	0.2457	0.32573	20.6749	1.0697	1.1526	0.37544	0.3558
10	0.2327	0.30327	20.1695	1.308		0.3976	
15	0.2147	0.2734	19.8577	1.08		0.2953	

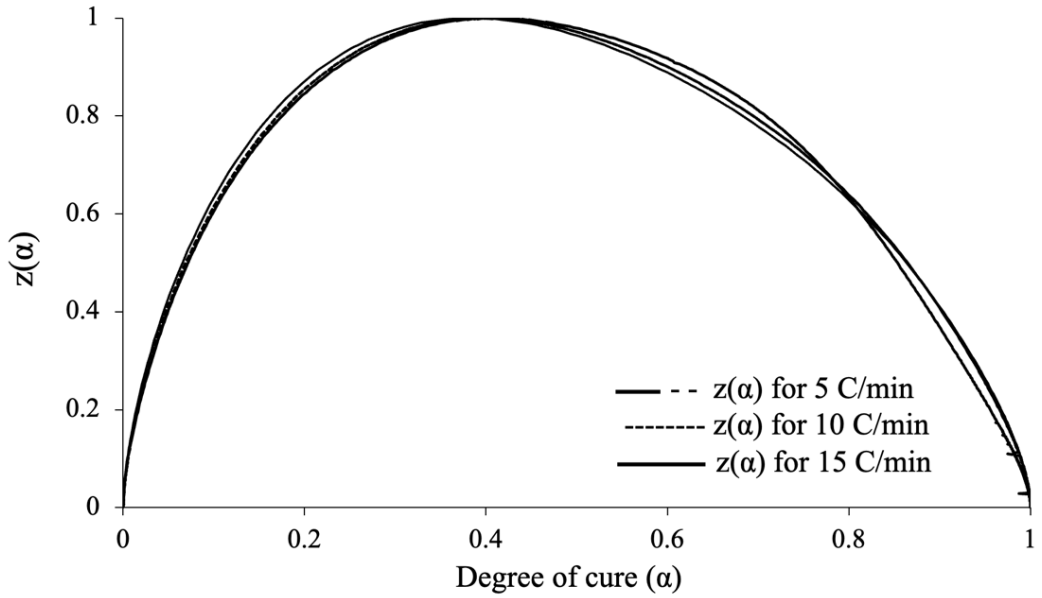

Figure 6.6 Variation of the function $z(\alpha)$ with the degree of cure.

6.3.2. Cure Simulation Results

These kinetic parameters and thermal boundary conditions are imported as the material data into the ACP/ACCS FE model for cure modeling. The strain on the top ply is extracted and compared with the experimental data for both symmetric and asymmetric laminates. Figure 6.7 shows the strain evolution during cure of both simulation and experiment for $[0/90]_s$ laminate.

The strain predicted by the model matches well with the experimental data throughout the cure for this symmetric layup as can be seen in the figures below. This model is also used to predict the strains in asymmetric laminates along with the symmetric layups. The strain evolution for [30/-30/60/-60] laminate can be seen in Figure 6.8 and similar to the symmetric laminate, the predicted strain by the model matches well with the experimental data. These results prove that the model is in good agreement with the experiment.

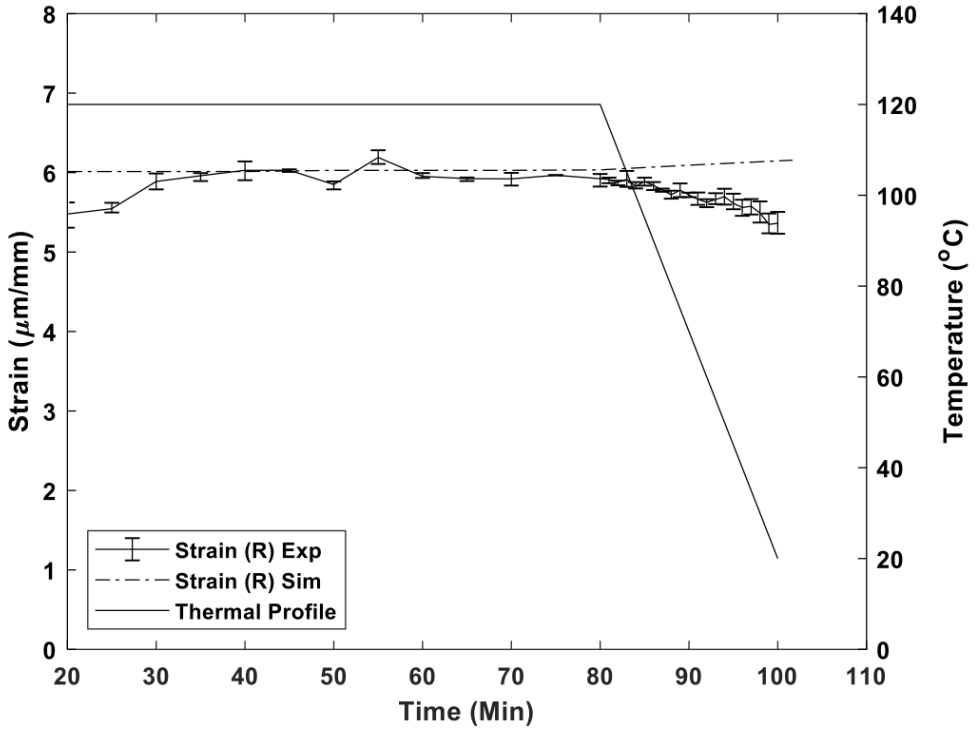

Figure 6.7 In-situ experimental vs simulation strain for symmetric $[0/90]_s$ laminate.

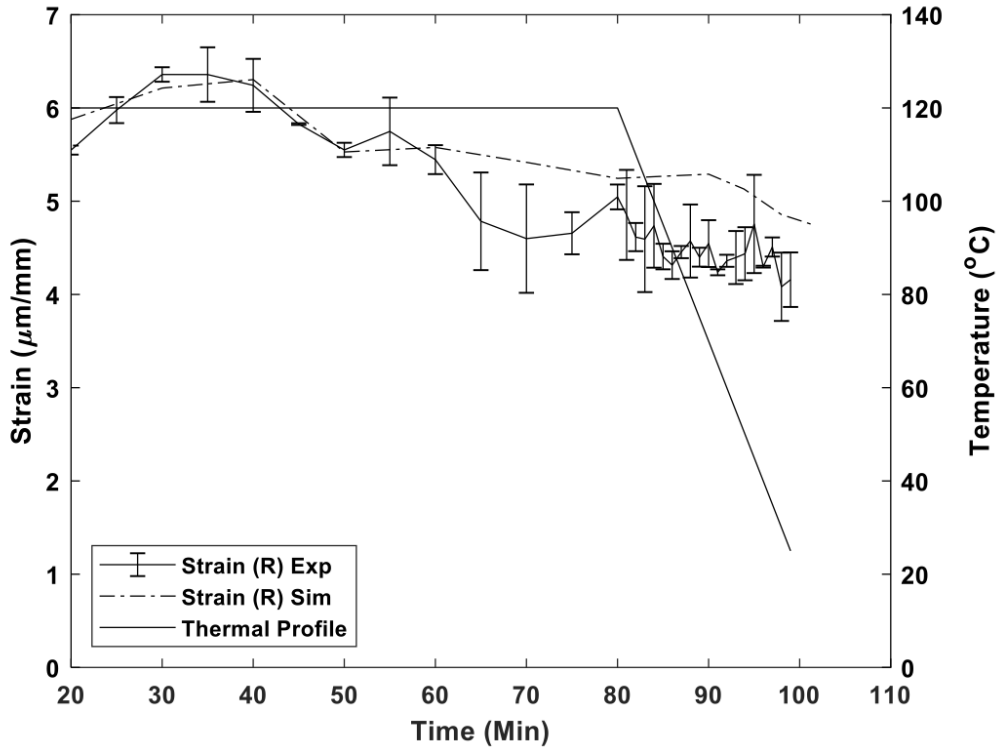

Figure 6.8 In situ experimental vs simulation strain for [30/-30/60/-60] laminate.

6.3.3. Cure Profile Design

After successfully setting up the cure simulation model, the next step is to optimize the cure profile to reduce the cure-induced strains. From Chapter 4, section 4.2.3, we know that abruptly interrupting the cure reduces the bonding temperatures of the fiber and matrix, and this low-temperature bonding results in lower cure-induced residual stresses. The cure interruption point is the primary process design variable that plays a key role in optimizing the cure profile and reducing the residual stresses. For the matrix considered in this simulation, the gel point is at 120^{o}C, and choosing the interruption point before the gel point is ineffective as the resin cross-linking will not start before the gel point. Similarly, interrupting the cure post vitrification will not be effective either as the matrix is almost completely cured after this point. So, three different points are programmed in the simulation to interrupt the cure as shown in Figure 6.9.

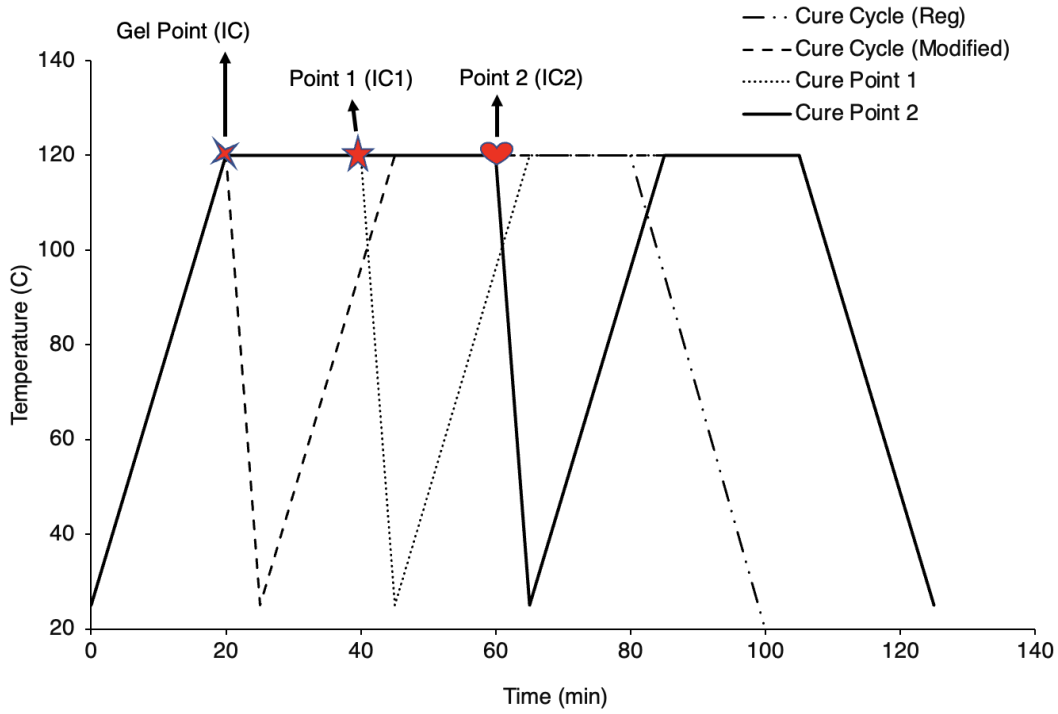

Figure 6.9 Modified cure profiles with three new cure interruption points.

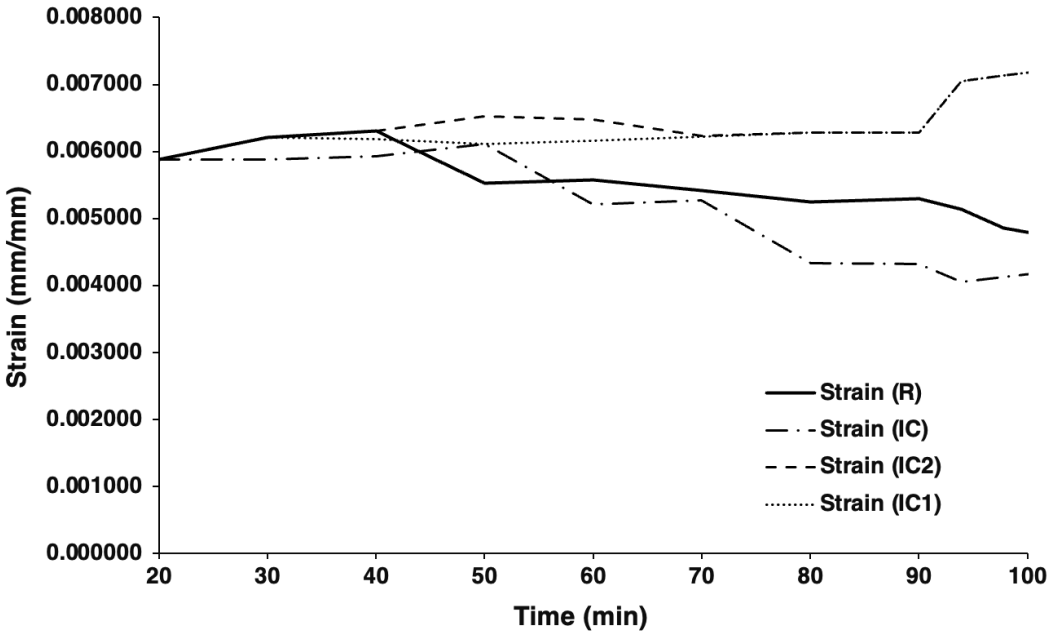

Figure 6.10 Strain evolution for regular and the three interrupted cure profiles.

The first interruption point is the gel point of the resin at 20 min which is the preferred interruption point according to the experiments. The second and third points are chosen to be at 40 min and 60 min into the cure as cure point 1 and cure point 2. These three cure profiles are programmed into the model for [30/-30/60/-60] layup. The strain evolution for the regular cure profile and three modified cure profiles are extracted from the simulation and plotted as shown in Figure 6.10. It can be observed that the strain at the end of the cure for the cure profile interrupted at gel point is lower than the regular cure profile. On the other hand, the strain at the end of the cure for IC1 and IC2 is higher than the regular strain. These results support the discussion in Chapter 4 Section 4.2.5 that interrupting the cure at gel point is effective in reducing the processing induced strains thereby reducing the residual stresses. Essentially, interrupting the cure at the gel point and abruptly cooling the sample decreases the resin diffusion. On the other hand,

the chemical reaction continues due to the exothermal reaction heat during the cure interruption. Also, experiments show that an abrupt-cooling operation after gelation could efficiently dissipate the strain generated by the laminate thermal contraction due to the resin's viscoelastic behavior (H. S. Kim et al., 2013). It is reported that this reduction in strain decreases the bonding temperatures between adjacent plies thereby reducing the residual stresses.

6.3.4. Results Comparison

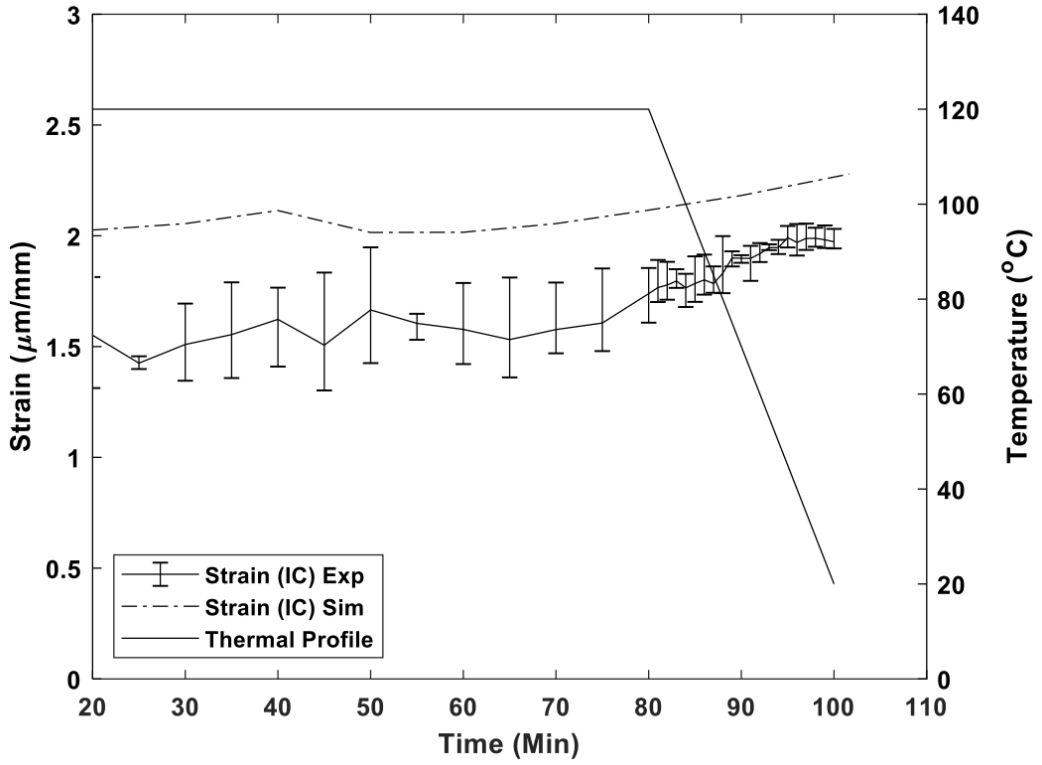

Figure 6.11 Strain evolution comparison for interrupted cure profile for $[0/90]_s$ layup.

The optimized cure profile with gel point as the cure interruption point is used to analyze the strain evolution for all symmetric and asymmetric layups considered in this study. The predicted strain evolution of symmetric $[0/90]_s$ layup is compared against the

experimental data in Figure 6.11. The model predicted the trend accurately. There is a higher difference between the simulation and experiments in this case. The cure-induced strains are relatively low for symmetric layups, which can explain this difference. Similarly, the simulation predicted data for balanced [30/-30/60/-60] layup is compared in Figure 6.12. It can be observed that the prediction for this layup is even closer than the symmetric layup.

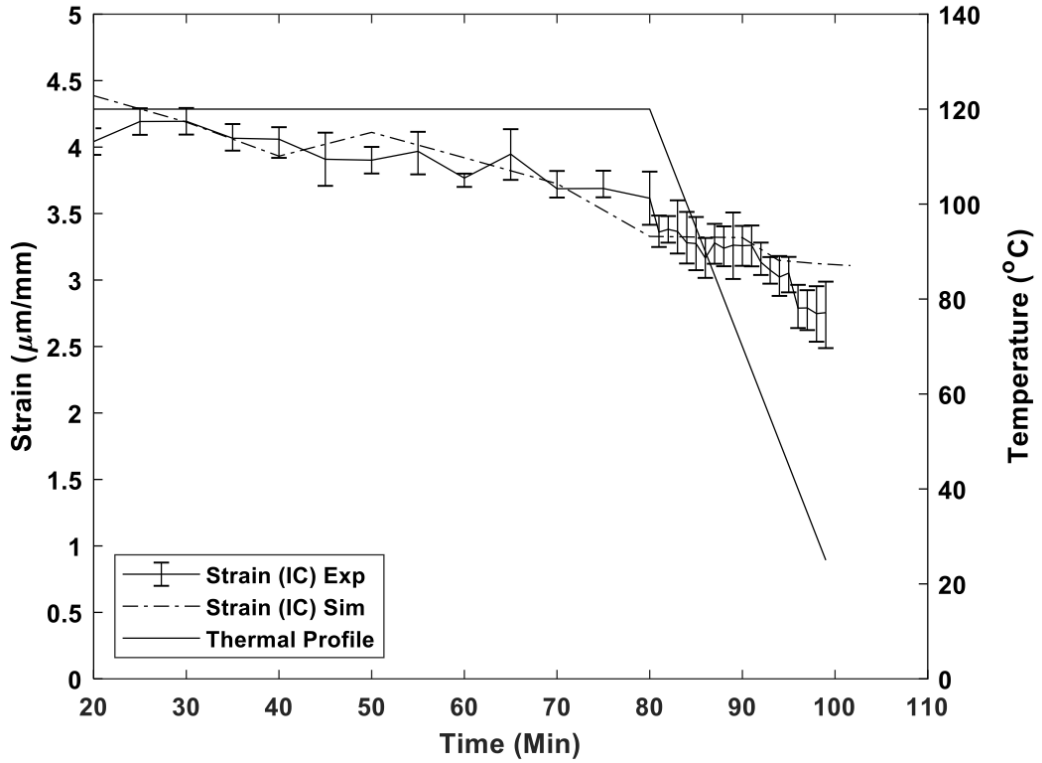

Figure 6.12 Strain evolution comparison for interrupted cure profile for [30/-30/60/-60].

The FE model is also used to analyze the strain evolution for $[0/45]_s$, [45/-45/45/-45], and [0/30/45/90] laminates and compared with the experimental data. For better visualization of the results, the difference in strain (Δ) between regular cure and optimized cure for experimental data is compared against the difference in strain (Δ) of

FE model for these three laminates in Figure 6.13 to Figure 6.15. The solid line in these figures represents the average experimental delta and the broken line represents the delta of the FE model.

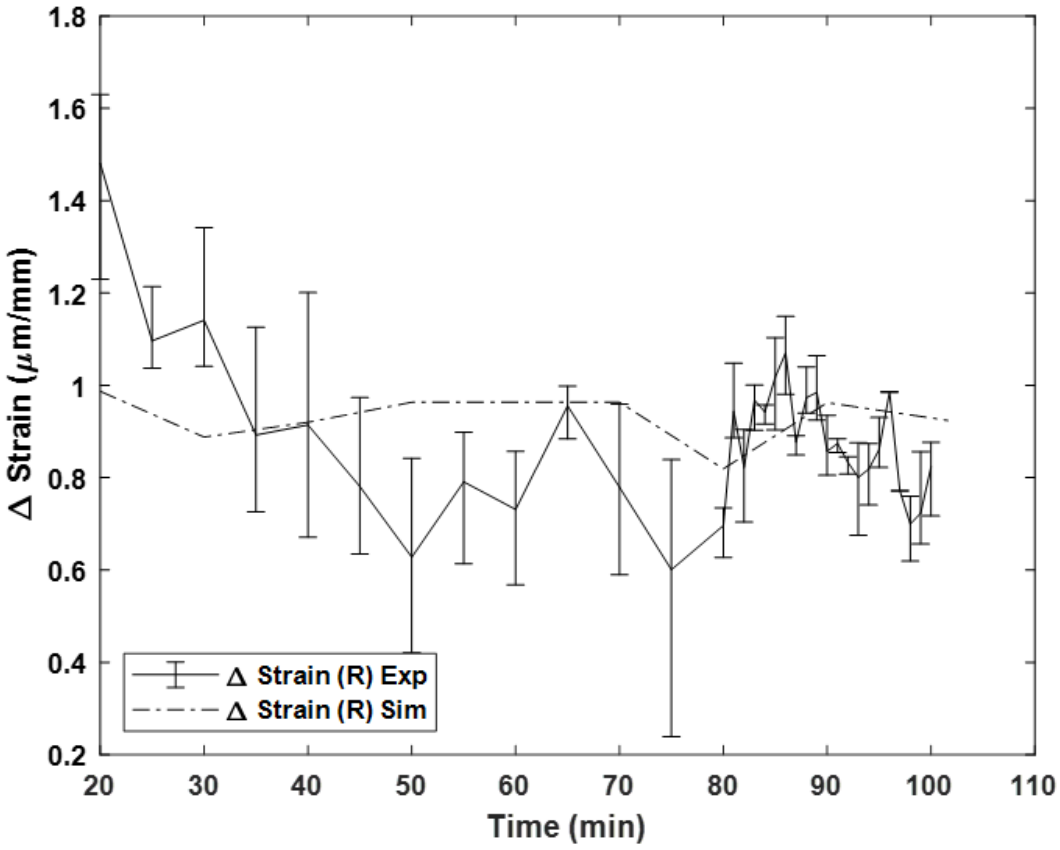

Figure 6.13 Strain difference between a regular and optimized cure for $[0/45]_s$ layup.

These results show that the FE model that is developed using ACP and ACCS is effective in predicting the strain during cure for both regular and optimized cures. From section 4.2 experimental data, it is apparent that interrupting the cure profile at the gel point of the resin is effective in reducing the residual stresses. The results from this FE model support choosing gel point as the point to interrupt the cure and abruptly cool to reduce the bonding temperature.

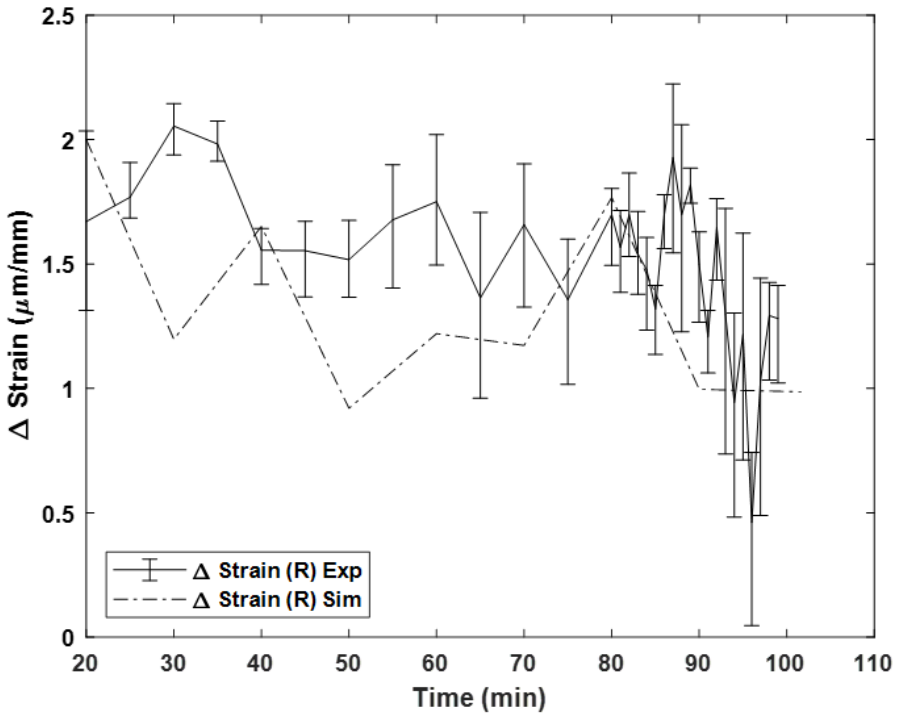

Figure 6.14 Strain difference comparison for [45/-45/45/-45] layup.

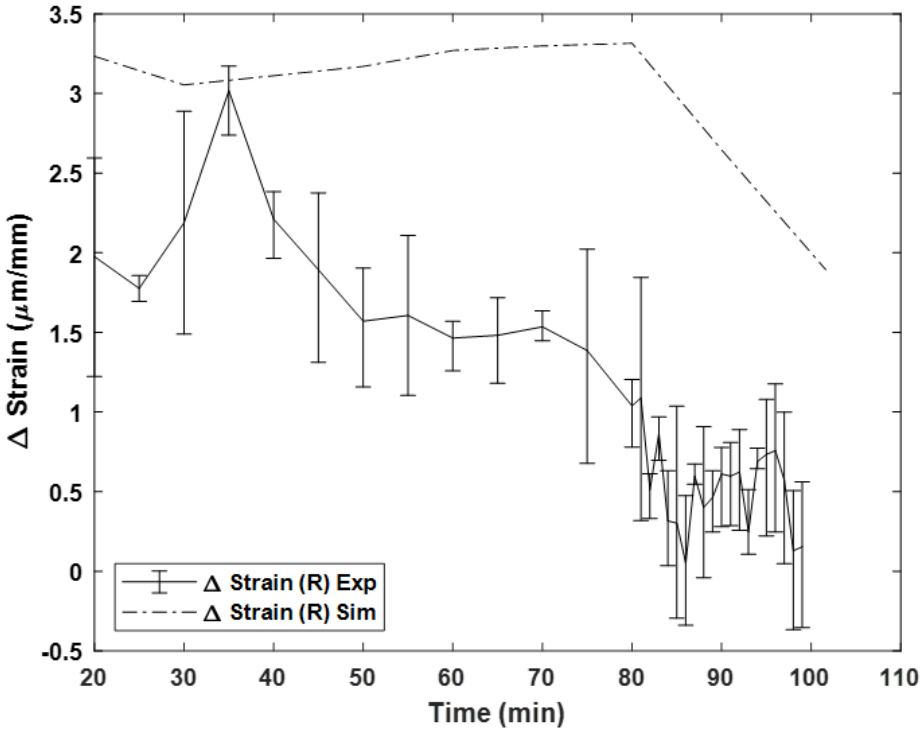

Figure 6.15 Strain difference between regular and optimized cure for [0/30/45/90] layup.

The FE model using ACCS also predicts the final deformed shape of the laminate. Figure 6.16 shows the experimental deformed [30/-30/60/-60] laminate compared against the FE model. From this figure, it can be observed that the model along with strain evolution, also predicts the deformed shape of the laminate after cure. These results show the potential of this approach to design cure cycles for any matrix material to reduce the cure-induced residual stresses. This reduction in stresses decreases manufacturing defects and increases the ultimate strength of the cured parts.

The modeling approach described in this chapter can be used in an optimization framework to evaluate the optimal cure cycles for achieving several different objectives such as minimizing distortion, reducing residual stresses, or decreasing cure time, etc. The process can be further fine-tuned and validated through in situ experimentation described in Chapters 3 and 4 and can be adapted for new materials like hybrid fibers and thin ply prepregs.

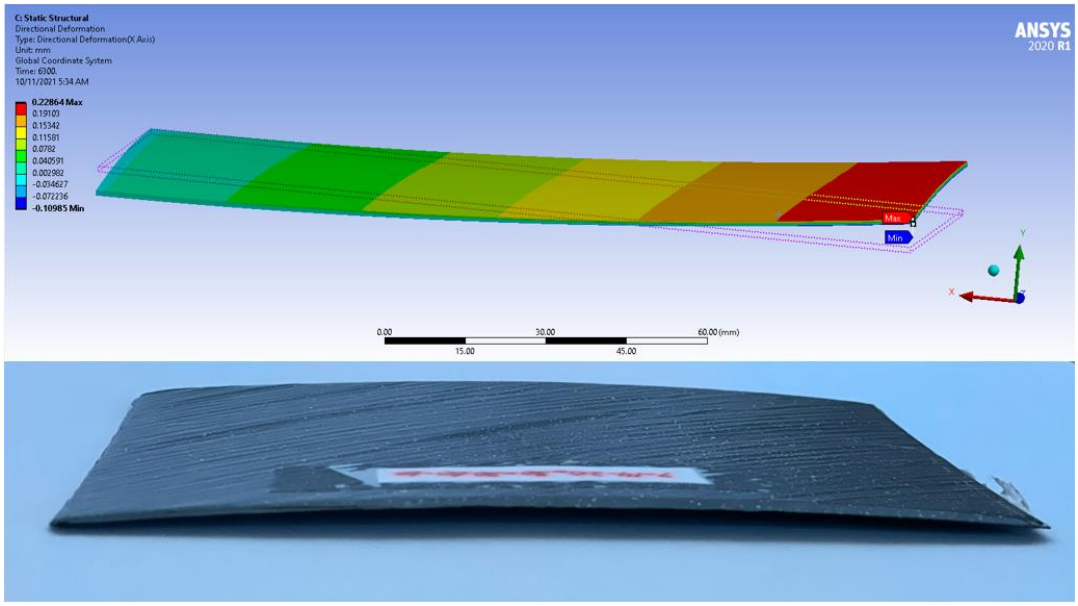

Figure 6.16 After cure deformed shape comparison of [30/-30/60/-60] laminate.

6.4. Summary

In this chapter, a thermomechanical cure model was developed using ACP and ACCS to model the composite cure process, and the results of the model are compared with the experimental data from Chapters 3 and 4. The formulation was developed for calculating reaction kinetics and other material properties to input into the FE model. From the preliminary results, the model accurately predicted the cure-induced strains and final deformed shapes. The main research findings are summarized below.

i. The resin reaction kinetics and related material properties were evaluated using DSC data

ii. In-situ cure strains are characterized through the mechanical model using ACP and transient thermal model using ACCS with predefined boundary conditions accurately simulating the cure phenomena inside an autoclave

iii. The cure profile of the simulation is modified using multiple abrupt cooling points and from the preliminary results, gel point is identified to be the optimum point to interrupt the cure.

iv. Comparing the difference in strain between the experimental and simulation data, the model developed in this chapter displayed the potential to predict the strain evolution and the final deformed shape of the laminate.

The modeling approaches developed in this chapter can be applied to any matrix material and can be used for process design to reduce cure-induced strains and resulting stresses.

7. Conclusions and Future Work

7.1. Conclusions

A novel in-situ experimental approach is developed to measure the dimensional changes in the laminates during cure and combined with temperature-dependent moduli obtained from Dynamic Mechanical Analysis (DMA) to calculate the continuous evolution of residual stresses during composite processing. This experimental approach is effective in calculating the residual stresses throughout the cure for both symmetric and asymmetric layups. The pattern of residual stresses developed after curing in all the layup configurations correlates with knowledge from literature. The combination of strain evolution and increase in modulus during cool down lead to a rapid increase in the residual stresses after vitrification. Warpage is developed in all three asymmetrical layups after processing. Higher residual stresses resulted in higher average warpage with the balanced unsymmetric [30/-30/60/-60] layup exhibiting an average warp of 1.46 mm.

Residual stresses are detrimental to composite structures as they induce processing defects like debonding, delamination, and matrix cracking which significantly decrease their load-bearing capability. These residual stresses during manufacturing are reduced using two different approaches. A cure cycle modification approach through cure interruption and interfacial modification approach by growing ZnO nanorods. A modified cure approach based on interrupting the cure after gelation is effective in reducing the residual stresses for both symmetric and asymmetric layups. The decrease in bonding temperatures due to the abrupt cooling operation resulted in lower residual stresses after vitrification. The decrease in residual stresses after cure increased both the first-ply failure load and ultimate strength of all the layups studied in this research. Approach

using ZnO nanorods to modify the ply interface show promising results in reducing cure-induced strains which often correlate with a reduction in residual stresses.

Processing induced defects in a carbon fiber prepreg composite are evaluated by devising another novel in-situ experimental approach. Carbon fiber prepreg laminates are cured in a specially designed autoclave with viewports with plies laid up on a mold with cylindrical tooling set up to maximize the ply movement. The processing induced defects in the composite are further characterized by X-ray micro-computed tomography (micro-CT). Modified ply interfaces by growing ZnO nanorods show potential to reduce the ply movement during cure. The experimental approach developed here can be used to quantify the behavior of the ply interfaces during manufacturing and could help devise approaches to reduce manufacturing defects in composite structures.

A thermomechanical cure model was developed using ACP and ACCS to model the composite cure while processing and the results of the model are compared against the experimental data. The formulation was developed for calculating reaction kinetics and other material properties to input into the FE model. From the preliminary results, the model accurately predicted the cure-induced strains and final deformed shapes when compared with the experimental data. The modeling approaches developed in this chapter can be applied to any matrix material and has the potential to optimize any cure profile to reduce cure-induced strains and resulting stresses.

7.2. Future Work

Residual stresses play a vital role in manufacturing composites. If not accounted for, these stresses are the primary source of defect initiation and propagation. While the experimental framework developed in this research demonstrates how to continuously

evaluate processing induced residual stresses during cure, it is vital to understand the origin of these stresses and reduce them to achieve defect-free manufacturing. Some additional directions of research to achieve further understanding are listed below.

7.2.1. Atomistic Modeling of Composite Interfaces and Curing Process

Computational modeling of the polymerization process at the atomistic level is essential for the fundamental understanding of the mechanisms responsible for cure induced strains during processing. Although the strain evolution is explained using large-scale modeling, developing an atomistic cure model using Molecular Dynamics (MD) simulations will help bridge the current gap in atomistic level understanding. While MD was used to study the matrix polymerization process in literature before, it has not been used to study the differential curing at ply interfaces, which is a key for defect formation.

7.2.2. Experimentally Validated Models for Optimization of Cure Profile

Preliminary results from the thermomechanical modeling using reaction kinetics and Ansys Composite Cure Modeling (ACCS) showed immense potential in effectively modeling the cure phenomenon inside an autoclave. This tool in combination with heat transfer models can be used to model complex aerospace components and for optimization the cure profile. This cure model can be developed to dynamically adjust the cure cycle while curing based on the real-time residual stress evolution data can be developed. An optimization framework can be developed with various objectives including (a) minimizing residual stresses and defects, and (a) minimizing production costs. The experimental procedures developed in the work provide an effective validation for the models.

The global FE model can be combined with the huge amount of DIC data collected for various experimental setups during this research to be used as an input to train a supervised Artificial Intelligence / Machine Learning (AI/ML) algorithm. The experimental data can guide the system by tagging the required output to help the machine learning system learn the characteristics or parameters of the optimized cure profile. Further, techniques such as linear or logistic regressions and decision tree classification can be implemented into the ML algorithm.

7.2.3. Nanoscale Interfacial Design

The kinematics of composite ply interfaces critically affects both the manufacturing processes and deformation mechanisms and is often responsible for the formation of processing induced defects such as wrinkles. Modifying ply interfaces is an effective way to restrict ply movement and reduce these processing induced defects. Although the preliminary results by growing ZnO nanorods on the ply surfaces in this research look promising in reducing processing induced strains, the mechanism through which this is happening is yet to be understood. A detailed study designing several nanoscale interfaces using different nanomaterials and corresponding computational modeling at continuum and atomistic scales will be effective in understanding the mechanisms for engineering interfacial kinematics during processing.

REFERENCES

Abdelal, G. F., Robotham, A., & Cantwell, W. (2013). Autoclave cure simulation of composite structures applying implicit and explicit FE techniques. *International Journal of Mechanics and Materials in Design*, *9*(1), 55–63.

Abdurohman, K., Satrio, T., & Muzayadah, N. L. (2018). A comparison process between hand lay-up, vacuum infusion and vacuum bagging method toward e-glass EW 185/lycal composites. *Journal of Physics: Conference Series*, *1130*(1), 12018.

Agbo, C. O. A., Okorie, B. A., & Obikwelu, D. O. N. (2017). Control of stress relaxation and residual thermal stress during cure of random fibre mat-reinforced polyester composites. *Journal of Composite Materials*, *51*(22), 3127–3136. https://doi.org/10.1177/0021998316684655

Agius, S. L., Joosten, M., Trippit, B., Wang, C. H., & Hilditch, T. (2016). Rapidly cured epoxy/anhydride composites: Effect of residual stress on laminate shear strength. *Composites Part A: Applied Science and Manufacturing*, *90*, 125–136. https://doi.org/10.1016/j.compositesa.2016.06.013

Alshahrani, H., & Hojjati, M. (2017). Bending behavior of multilayered textile composite prepregs: Experiment and finite element modeling. *Materials and Design*, *124*, 211–224. https://doi.org/10.1016/j.matdes.2017.03.077

Arshad, M. A., & Maaroufi, A. (2015). Relationship between Johnson–Mehl–Avrami and Šesták–Berggren models in the kinetics of crystallization in amorphous materials. *Journal of Non-Crystalline Solids*, *413*, 53–58.

ASC Process Systems. Retrieved November 14, 2021, from http://www.aschome.com/index.php/en/products/autoclaves/whats-an-econoclave

Ayyagari, S., & Al-Haik, M. (2019). Enhancing the viscoelastic performance of carbon fiber composites by incorporating CNTs and ZnO nanofillers. *Applied Sciences*, *9*(11), 2281.

Ballinger, C. (1990). Structural FRP composites. *Civil Engineering—ASCE*, *60*(7), 63–65.

Bartlett, J. L., Croom, B. P., Burdick, J., Henkel, D., & Li, X. (2018). Revealing mechanisms of residual stress development in additive manufacturing via digital image correlation. *Additive Manufacturing*, *22*, 1–12. https://doi.org/10.1016/j.addma.2018.04.025

Bartlett, J. L., & Li, X. (2019). An overview of residual stresses in metal powder bed fusion. *Additive Manufacturing*, *27*, 131–149. https://doi.org/10.1016/j.addma.2019.02.020

Bedayat, H., Forghani, A., Hickmott, C., Palmieri, F., Grimsley, B., Coxon, B., Fernlund, G., & Poursartip, A. (2018). Numerical and Experimental Study of Local Resin Pressure for the Manufacturing of Composite Structures and their Effect on Porosity. *SAMPE 2018 Technical Conference and Exhibition, Long Beach, CA*.

Benedikt, B., Rupnowski, P., Kumosa, L., Sutter, J. K., Predecki, P. K., & Kumosa, M. (2002). Determination of interlaminar residual thermal stresses in a woven 8HS graphite/PMR-15 composite using X-ray diffraction measurements. *Mechanics of Advanced Materials and Structures*, *9*(4), 375–394. https://doi.org/10.1080/15376490290097026

Blagojevic, J., Mijatović, B., Kočović, D., Stojanovic, B., Ivanović, L., & Gajević, S. (2020). A review to cast polymer composite materials for interior environments. *Applied Engineering Letters*.

Boey, F. Y. C., & Lye, S. W. (1990). Effects of vacuum and pressure in an autoclave curing process for a thermosetting fibre-reinforced composite. *Journal of Materials Processing Technology*, *23*(2), 121–131.

Boey, F. Y. C., & Lye, S. W. (1992). Void reduction in autoclave processing of thermoset composites: Part 1: High pressure effects on void reduction. *Composites*, *23*(4), 261–265.

Bohne, T., Frerich, T., Jendrny, J., Jürgens, J.-P., & Ploshikhin, V. (2018). Simulation and validation of air flow and heat transfer in an autoclave process for definition of thermal boundary conditions during curing of composite parts. *Journal of Composite Materials*, *52*(12), 1677–1687.

Bowles, D. E., & Tompkins, S. S. (1989). Prediction of coefficients of thermal expansion for unidirectional composites. *Journal of Composite Materials*, *23*(4), 370–388.

Chan, H. S., Leng, Y., & Gao, F. (2002). Processing of PC/LCP in situ composites by closed-loop injection molding. *Composites Science and Technology*, *62*(6), 757–765.

Chandra, N., Li, H., Shet, C., & Ghonem, H. (2002). Some issues in the application of cohesive zone models for metal–ceramic interfaces. *International Journal of Solids and Structures*, *39*(10), 2827–2855.

Chapman, T. J., Gillespie, J. W., Pipes, R. B., Manson, J. A. E., & Seferis, J. C. (1990). Prediction of Process-Induced Residual Stresses in Thermoplastic Composites. *Journal of Composite Materials*, *24*(6), 616–643. https://doi.org/10.1177/002199839002400603

Chava, S., & Namilae, S. (2020). In-Situ Investigation of the Kinematics of Ply interfaces during Composite Manufacturing. *Journal of Manufacturing Science and Engineering*, 1–28 143(2), 021006. https://doi.org/10.1115/1.4047740

Chava, S., & Namilae, S. (2021a). Continuous evolution of processing induced residual stresses in composites: An in-situ approach. *Composites Part A: Applied Science and Manufacturing*, *145*, 106368. https://doi.org/10.1016/j.compositesa.2021.106368

Chava, S., & Namilae, S. (2021b). In Situ Investigation of the Kinematics of Ply Interfaces during Composite Manufacturing. *Journal of Manufacturing Science and Engineering, Transactions of the ASME*, *143*(2). https://doi.org/10.1115/1.4047740

Cheng, W., & Finnie, I. (2007). Residual Stress Measurement and the Slitting Method. In *Residual Stress Measurement and the Slitting Method*. Springer Science & Business Media. https://doi.org/10.1007/978-0-387-39030-7

Chiang, M. Y. M., McKenna, G. B., & Yuan, J. (1994). A viscoelastic micor-mechanical analysis for dimensional stability of a composite layer. *Polymer Engineering & Science*, *34*(24), 1815–1822. https://doi.org/10.1002/pen.760342406

Chung, D. (2012). *Carbon fiber composites*. Elsevier.

Correlated Solutions DIC System Specifications. (n.d.). Retrieved January 14, 2021, from https://www.correlatedsolutions.com/vic-3d/

Cowley, K. D., & Beaumont, P. W. R. (1997). The measurement and prediction of residual stresses in carbon-fibre/polymer composites. *Composites Science and Technology*, *57*(11), 1445–1455. https://doi.org/10.1016/S0266-3538(97)00048-1

Crasto, A. S., & Kim, R. Y. (1993). On the Determination of Residual Stresses in Fiber-Reinforced Thermoset Composites. *Journal of Reinforced Plastics and Composites*, *12*(5), 545–558. https://doi.org/10.1177/073168449301200505

Croom, B. P., Bumgardner, C., & Li, X. (2016). Unveiling residual stresses in air plasma spray coatings by digital image correlation. *Extreme Mechanics Letters*, *7*, 126–135. https://doi.org/10.1016/j.eml.2016.02.013

Das, S., Choudhury, P., Halder, S., & Sriram, P. (2013). Stress and free edge delamination analyses of delaminated composite structure using ANSYS. *Procedia Engineering*, *64*, 1364–1373. https://doi.org/10.1016/j.proeng.2013.09.218

Deng, S., Hou, M., & Ye, L. (2007). Temperature-dependent elastic moduli of epoxies measured by DMA and their correlations to mechanical testing data. *Polymer Testing*, *26*(6), 803–813. https://doi.org/10.1016/j.polymertesting.2007.05.003

Ding, A., Li, S., Sun, J., Wang, J., & Zu, L. (2016). A thermo-viscoelastic model of process-induced residual stresses in composite structures with considering thermal dependence. *Composite Structures*, *136*, 34–43. https://doi.org/10.1016/j.compstruct.2015.09.014

Dodwell, T. J., Butler, R., & Hunt, G. W. (2014). Out-of-plane ply wrinkling defects during consolidation over an external radius. *Composites Science and Technology*, *105*, 151–159. https://doi.org/10.1016/j.compscitech.2014.10.007

Duquennoy, M., Ouaftouh, M., & Ourak, M. (1999). Ultrasonic evaluation of stresses in orthotropic materials using Rayleigh waves. *NDT and E International*, *32*(4), 189–199. https://doi.org/10.1016/S0963-8695(98)00046-2

Elhajjar, R. F., & Shams, S. S. (2014). Compression testing of continuous fiber reinforced polymer composites with out-of-plane fiber waviness and circular notches. *Polymer Testing*, *35*, 45–55. https://doi.org/10.1016/j.polymertesting.2014.02.004

Erland, S., Dodwell, T. J., & Butler, R. (2014). Inter and intra-ply shearing of uncured carbon fibre laminates. *ECCM16-16TH European Conference on Composite Materials, June*, 22–26.

Fanfoni, M., & Tomellini, M. (1998). The johnson-mehl-avrami-kohnogorov model: a brief review. *Il Nuovo Cimento D*, *20*(7), 1171–1182.

Fernlund, G., & Poursartip, A. (1999). The effect of tooling material, cure cycle, and tool surface finish on spring-in of autoclave processed curved composite parts. *Proceedings of ICCM*, *12*, 5–9.

Fiorina, M., Seman, A., Castanie, B., Ali, K. M., Schwob, C., & Mezeix, L. (2017). Spring-in prediction for carbon/epoxy aerospace composite structure. *Composite Structures*, *168*, 739–745. https://doi.org/10.1016/j.compstruct.2017.02.074

Fish, J., LeMonds, J., & Shek, K. L. (1999). Modeling of wrinkling in compression molding of composites. *Journal of Engineering Mechanics*, *125*(8), 951–955.

Freemantle, R., Giannis, S., & Ják, V. M. a T. Ě. (2014). Phased Array Data Manipulation for Damage Tolerance Assessment of Composites using Finite Element Analysis. In *11th European Conference on Non-Destructive Testing (ECNDT)*.

Fuchs, E. R. H., Field, F. R., Roth, R., & Kirchain, R. E. (2008). Strategic materials selection in the automobile body: Economic opportunities for polymer composite design. *Composites Science and Technology*, *68*(9), 1989–2002. https://doi.org/10.1016/j.compscitech.2008.01.015

G. Melin, L., & E. Asp, L. (1999). Effects of strain rate on transverse tension properties of a carbon/epoxy composite: Studied by moiré photography. In *Composites Part A: Applied Science and Manufacturing*, 30(3), 305-316. https://doi.org/10.1016/S1359-835X(98)00123-7

Gallage, C., & Jayalath, C. (2019). Use of particle image velocimetry (PIV) technique to measure strains in geogrids. In *Proceedings of the 7th International Symposium on*

Deformation Characteristics of Geomaterials (IS-Glasgow 2019)(E3S Web of Conferences, Volume 92) (pp. 1-6). EDP Sciences. https://doi.org/10.1051/e3sconf/20199212007

Gay, D. (2014). *Composite Materials: Design and Applications*. CRC press.

Geleta, T. N., Woo, K., & Lee, B. (2018). Delamination Behavior of L-Shaped Laminated Composites. *International Journal of Aeronautical and Space Sciences*, *19*(2), 363–374. https://doi.org/10.1007/s42405-018-0038-y

Ghasemi, A. R., Mohammadi, M. M., & Mohandes, M. (2015). The role of carbon nanofibers on thermo-mechanical properties of polymer matrix composites and their effect on reduction of residual stresses. *Composites Part B: Engineering*, *77*, 519–527.

Ginstling, A. M., & Brounshtein, B. I. (1950). Concerning the diffusion kinetics of reactions in spherical particles. *J. Appl. Chem. USSR*, *23*(12), 1327–1338.

Goda, I., L'Hostis, G., & Guerlain, P. (2019). In-situ non-contact 3D optical deformation measurement of large capacity composite tank based on close-range photogrammetry. *Optics and Lasers in Engineering*, *119*, 37–55. https://doi.org/10.1016/j.optlaseng.2019.02.006

Greszczuk, L. (1969). Theoretical studies of the mechanics of the fiber-matrix interface in composites. In *Interfaces in composites*. (West Conshohocken, PA: ASTM International, 1969), 42-58. https://doi.org/10.1520/STP44699S

Hallander, P., Akermo, M., Mattei, C., Petersson, M., & Nyman, T. (2013). An experimental study of mechanisms behind wrinkle development during forming of composite laminates. *Composites Part A: Applied Science and Manufacturing*, *50*, 54–64. https://doi.org/10.1016/j.compositesa.2013.03.013

Hallander, P., Sjölander, J., & Åkermo, M. (2015). Forming induced wrinkling of composite laminates with mixed ply material properties; an experimental study. *Composites Part A: Applied Science and Manufacturing*, *78*, 234–245. https://doi.org/10.1016/j.compositesa.2015.08.025

Hannusch, S., Stockmann, M., & Ihlemann, J. (2016). Experimental Method for Residual Stress Analysis with Fibre Bragg Grating Sensors. *Materials Today: Proceedings*, *3*(4), 979–982. https://doi.org/10.1016/j.matpr.2016.03.032

Hardis, R., Jessop, J. L. P., Peters, F. E., & Kessler, M. R. (2013). Cure kinetics characterization and monitoring of an epoxy resin using DSC, Raman spectroscopy, and DEA. *Composites Part A: Applied Science and Manufacturing*, *49*, 100–108. https://doi.org/10.1016/j.compositesa.2013.01.021

Hassan, M. H., Othman, A. R., & Kamaruddin, S. (2017). A review on the manufacturing defects of complex-shaped laminate in aircraft composite structures. In *International*

Journal of Advanced Manufacturing Technology (Vol. 91, Issues 9–12, pp. 4081–4094). Springer London. https://doi.org/10.1007/s00170-017-0096-5

Heslehurst, R. B. (2014). *Defects and Damage in Composite Materials and Structures*. CRC press.

Hsueh, C.-H. (1990). Interfacial debonding and fiber pull-out stresses of fiber-reinforced composites. *Materials Science and Engineering: A*, *123*(1), 1–11.

Hubert, P., Fernlund, G., & Poursartip, A. (2012). Autoclave processing for composites. In *Manufacturing techniques for polymer matrix composites (PMCs)* (pp. 414–434). Elsevier.

Hubert, P., & Poursartip, A. (2001). A method for the direct measurement of the fibre bed compaction curve of composite prepregs. *Composites Part A: Applied Science and Manufacturing*, *32*(2), 179–187.

Ifju, P. G., Niu, X., Kilday, B. C., Liu, S. C., & Ettinger, S. M. (2000). Residual strain measurement in composites using the cure-referencing method. *Experimental Mechanics*, *40*(1), 22–30. https://doi.org/10.1007/BF02327544

Ifju, P., Myers, D., & Schulz, W. (2006). Residual stress and thermal expansion of graphite epoxy laminates subjected to cryogenic temperatures. *Composites Science and Technology*, *66*(14), 2449–2455.

İpek, G., Arman, Y., & Çelik, A. (2018). The effect of delamination size and location to buckling behavior of composite materials. *Composites Part B: Engineering*, *155*, 69–76. https://doi.org/10.1016/j.compositesb.2018.08.009

Irving, P., & Soutis, C. (2019). Polymer composites in the aerospace industry. In *Polymer Composites in the Aerospace Industry*. Woodhead Publishing. https://doi.org/10.1016/C2017-0-03502-4

Jain, L. K., & Mai, Y. W. (1996). On residual stress induced distortions during fabrication of composite shells. *Journal of Reinforced Plastics and Composites*, *15*(8), 793–805. https://doi.org/10.1177/073168449601500803

Jannotti, P., Subhash, G., Zheng, J., & Halls, V. (2017). Measurement of microscale residual stresses in multi-phase ceramic composites using Raman spectroscopy. *Acta Materialia*, *129*, 482–491. https://doi.org/10.1016/j.actamat.2017.03.015

Johnston, A., Hubert, P., Vaziri, R., & Poursartip, A. (1998). An investigation of autoclave convective heat transfer. *Design and Manufacturing of Composites*, 106–113.

Jones, R. M. (1998). *Mechanics of Composite Materials*. CRC press.

Jung, H., Yu, S., Bae, N. S., Cho, S. M., Kim, R. H., Cho, S. H., Hwang, I., Jeong, B., Ryu, J. S., Hwang, J., Hong, S. M., Koo, C. M., & Park, C. (2015). High Through-Plane Thermal Conduction of Graphene Nanoflake Filled Polymer Composites Melt-Processed in an L-Shape Kinked Tube. *ACS Applied Materials and Interfaces*, *7*(28), 15256–15262. https://doi.org/10.1021/acsami.5b02681

Kam, T. Y., & Sher, H. F. (1995). Nonlinear and First-Ply Failure Analyses of Laminated Composite Cross-Ply Plates. *Journal of Composite Materials*, *29*(4), 463–482. https://doi.org/10.1177/002199839502900403

Kim, H. S., & Lee, D. G. (2006). Avoidance of fabricational thermal residual stresses in co-cure bonded metal-composite hybrid structures. *Journal of Adhesion Science and Technology*, *20*(9), 959–979. https://doi.org/10.1163/156856106777657805

Kim, H. S., Park, S. W., & Lee, D. G. (2006). Smart cure cycle with cooling and reheating for co-cure bonded steel/carbon epoxy composite hybrid structures for reducing thermal residual stress. *Composites Part A: Applied Science and Manufacturing*, *37*(10), 1708–1721. https://doi.org/10.1016/j.compositesa.2005.09.015

Kim, H. S., Yoo, S. H., & Chang, S. H. (2013). In situ monitoring of the strain evolution and curing reaction of composite laminates to reduce the thermal residual stress using FBG sensor and dielectrometry. *Composites Part B: Engineering*, *44*(1), 446–452. https://doi.org/10.1016/j.compositesb.2012.04.021

Kim, J. S., & Lee, D. G. (1997). Development of an autoclave cure cycle with cooling and reheating steps for thick thermoset composite laminates. *Journal of Composite Materials*, *31*(22), 2264–2282.

Kim, K. S., & Hahn, H. T. (1989). Residual stress development during processing of graphite/epoxy composites. *Composites Science and Technology*, *36*(2), 121–132. https://doi.org/10.1016/0266-3538(89)90083-3

Kim, R. Y., & Hahn, H. T. (1979). Effect of Curing Stresses on the First Ply-failure in Composite Laminates. *Journal of Composite Materials*, *13*(1), 2–16. https://doi.org/10.1177/002199837901300101

Kim, S. S., Murayama, H., Kageyama, K., Uzawa, K., & Kanai, M. (2012). Study on the curing process for carbon/epoxy composites to reduce thermal residual stress. *Composites Part A: Applied Science and Manufacturing*, *43*(8), 1197–1202. https://doi.org/10.1016/j.compositesa.2012.02.023

Klingbeil, N. W., Beuth, J. L., Chin, R. K., & Amon, C. H. (2002). Residual stress-induced warping in direct metal solid freeform fabrication. *International Journal of Mechanical Sciences*, *44*(1), 57–77. https://doi.org/10.1016/S0020-7403(01)00084-4

Kluge, J. N. E., Lundström, T. S., Westerberg, L.-G., & Nyman, T. (2016). Modelling heat transfer inside an autoclave: effect of radiation. *Journal of Reinforced Plastics and Composites*, *35*(14), 1126–1142.

Koga, N., & Malek, J. (1996). Accommodation of the actual solid-state process in the kinetic model function. Part 2. Applicability of the empirical kinetic model function to diffusion-controlled reactions. *Thermochimica Acta*, *282*, 69–80.

Koyama, M., Hatta, H., & Fukuda, H. (2005). Effect of temperature and layer thickness on these strengths of carbon bonding for carbon/carbon composites. *Carbon*, *43*(1), 171–177.

Kravchenko, O. G., Kravchenko, S. G., Casares, A., & Pipes, R. B. (2015). Digital image correlation measurement of resin chemical and thermal shrinkage after gelation. *Journal of Materials Science*, *50*(15), 5244–5252. https://doi.org/10.1007/s10853-015-9072-3

Kumbhare, N., Moheimani, R., & Dalir, H. (2021). Analysis of Composite Structures in Curing Process for Shape Deformations and Shear Stress: Basis for Advanced Optimization. *Journal of Composites Science*, *5*(2), 63.

Lee, J. M., Kim, B. M., Lee, C. J., & Ko, D. C. (2017). A characterisation of tool-ply friction behaviors in thermoplastic composite. *Procedia Engineering*, *207*, 90–94. https://doi.org/10.1016/j.proeng.2017.10.743

Levy, A., & Hubert, P. (2019). Vacuum-bagged composite laminate forming processes: Predicting thickness deviation in complex shapes. In *Composites Part A: Applied Science and Manufacturing* (Vol. 126). Elsevier. https://doi.org/10.1016/j.compositesa.2019.105568

Levy, A., Stadlin, J., & Hubert, P. (2014). Corner consolidation in vacuum bag only processing of out-of-autoclave composite prepregs laminates. *International SAMPE Technical Conference*.

Li, F., Leng, J., Liu, Y., Remillat, C., & Scarpa, F. (2020). Temperature dependence of elastic constants in unidirectional carbon fiber reinforced shape memory polymer composites. *Mechanics of Materials*, *148*, 103518. https://doi.org/10.1016/j.mechmat.2020.103518

Lightfoot, J. S., Wisnom, M. R., & Potter, K. (2013). A new mechanism for the formation of ply wrinkles due to shear between plies. *Composites Part A: Applied Science and Manufacturing*, *49*, 139–147. https://doi.org/10.1016/j.compositesa.2013.03.002

LIU, S.C. (1999). *Residual stress characterization for laminated composites* (p. 169). University of Florida.

Liu, C., & Shi, Y. (2018). An improved analytical solution for process-induced residual stresses and deformations in flat composite laminates considering thermo-viscoelastic effects. Materials, 11(12), 2506.

Liu, Z., Xiao, J., Bai, S., & Zhang, W. (2012). Study on phenomenological curing model of epoxy resin for prediction of degree of cure. *Journal of Thermal Analysis and Calorimetry*, *109*(3), 1555–1561. https://doi.org/10.1007/s10973-011-2070-z

Málek, J. (1992). The kinetic analysis of non-isothermal data. *Thermochimica Acta*, *200*, 257–269.

Melin, L. G., & Asp, L. E. (1999). Effects of strain rate on transverse tension properties of a carbon/epoxy composite: studied by moiré photography. Composites Part A: Applied Science and Manufacturing, 30(3), 305-316.

Meng, Y., Yan, L., Huang, W., & Zhang, T. (2019). Detailed parametric investigation and optimization of a composite wing with high aspect ratio. *International Journal of Aerospace Engineering*, vol. 2019, Article ID 3684015, 27 pages, 2019. https://doi.org/10.1155/2019/3684015.

Mizukami, K., Mizutani, Y., Todoroki, A., & Suzuki, Y. (2016). Detection of in-plane and out-of-plane fiber waviness in unidirectional carbon fiber reinforced composites using eddy current testing. *Composites Part B: Engineering*, *86*, 84–94. https://doi.org/10.1016/j.compositesb.2015.09.041

Montserrat, S. (1992). Vitrification and further structural relaxation in the isothermal curing of an epoxy resin. *Journal of Applied Polymer Science*, *44*(3), 545–554. https://doi.org/10.1002/app.1992.070440319

Montserrat, S., & Málek, J. (1993). A kinetic analysis of the curing reaction of an epoxy resin. *Thermochimica Acta*, *228*, 47–60.

Motagi, S., Chava, S., & Namilae, S. (2019). In-situ measurement of resin shrinkage in epoxy composite. *International SAMPE Technical Conference*, NC, May 2019.

Motagi, S., & Namilae, S. (2021). In-situ Investigation of Resin Shrinkage in the Composite Manufacturing Environment. *Applied Composite Materials*, 28(3), 651-657. https://doi.org/10.1007/s10443-021-09887-x

Nairn, J. A. (2000). Matrix Microcracking in Composites. *Comprehensive Composite Materials*, *2*, 403–432. https://doi.org/10.1016/b0-08-042993-9/00069-3

Nairn, J. A., & Zoller, P. (1985). Matrix solidification and the resulting residual thermal stresses in composites. *Journal of Materials Science*, *20*(1), 355–367. https://doi.org/10.1007/BF00555929

Nanni, A. (1993). FRP reinforcement for prestressed and non-prestressed concrete structures. In *Fiber-Reinforced-Plastic (FRP) Reinforcement for Concrete Structures* (pp. 3–12). Elsevier.

Nelson, J. W., Riddle, T. W., & Cairns, D. S. (2017). Characterization and Mechanical Testing of Manufacturing Defects Common to Composite Wind Turbine Blades. *Wind Energy Science Discussions*, *2*(2), 1–17. https://doi.org/10.5194/wes-2017-13

Nikbakht, M., Yousefi, J., Hosseini-Toudeshky, H., & Minak, G. (2017). Delamination evaluation of composite laminates with different interface fiber orientations using acoustic emission features and micro visualization. *Composites Part B: Engineering*, *113*, 185–196.

Nikishkov, G., Nikishkov, Y., & Makeev, A. (2013). Finite element mesh generation for composites with ply waviness based on X-ray computed tomography. *Advances in Engineering Software*, *58*, 35–44. https://doi.org/10.1016/j.advengsoft.2013.01.002

Nimmer, R. P. (1990). Fiber-matrix interface effects in the presence of thermally induced residual stresses. *Journal of Composites, Technology and Research*, *12*(2), 65–75. https://doi.org/10.1520/ctr10181j

Niu, X., Zhang, H., Pei, Z., Shi, N., Sun, C., & Gong, J. (2019). Measurement of interfacial residual stress in SiC fiber reinforced Ni-Cr-Al alloy composites by Raman spectroscopy. *Journal of Materials Science & Technology*, *35*(1), 88–93.

Nunez, C. M., Ramsey, G. H., Kong, E. J., Bahner, M. A., Wright, R. S., Clayton, C. A., & Baskir, J. N. (1999). Evaluation of pollution prevention options to reduce styrene emissions from fiber-reinforced plastic open molding processes. *Journal of the Air & Waste Management Association*, *49*(3), 256–267.

Ozyildiz, M., Muyan, C., & Coker, D. (2018). Strength analysis of a composite turbine blade using puck failure criteria. *Journal of Physics: Conference Series*, *1037*(4), 042027.

Pagliaro, P., & Zuccarello, B. (2007). Residual stress analysis of orthotropic materials by the through-hole drilling method. *Experimental Mechanics*, *47*(2), 217–236. https://doi.org/10.1007/s11340-006-9019-3

Palmese, G. R., & McCullough, R. L. (1994). Kinetic and thermodynamic considerations regarding interphase formation in thermosetting composite systems. *The Journal of Adhesion*, *44*(1–2), 29–49.

Pandey, R. K., & Sun, C. T. (1999). Mechanisms of wrinkle formation during the processing of composite laminates. In *Composites Science and Technology*, 59(3). https://doi.org/10.1016/S0266-3538(98)00080-3

Park, H. J., Son, C., & Park, S. H. (2014). Fabrication of micro-scale wrinkles on a curved surface using weak-polymerization and surface shrinkage. *International*

Journal of Precision Engineering and Manufacturing, *15*(11), 2469–2471. https://doi.org/10.1007/s12541-014-0616-2

Parlevliet, P. P., Bersee, H. E. N., & Beukers, A. (2006). Residual stresses in thermoplastic composites—A study of the literature—Part I: Formation of residual stresses. *Composites Part A: Applied Science and Manufacturing*, *37*(11), 1847–1857.

Patil, A., Moheimani, R., Shakhfeh, T., & Dalir, H. (2019). Analysis of Spring-in for Composite Plates Using ANSYS Composite Cure Simulation. *American Society for Composites.* https://doi.org/10.12783/asc34/31307

Patil, A. S., Moheimani, R., & Dalir, H. (2019). Thermomechanical analysis of composite plates curing process using ANSYS composite cure simulation. *Thermal Science and Engineering Progress*, *14*, 100419.

Pawlak, A., Zinck, P., Galeski, A., & Gerard, J. F. (2001). Photoelastic studies of residual stresses around fillers embedded in an epoxy matrix. *Macromolecular Symposia*, *169*(1), 197–210. https://doi.org/10.1002/1521-3900(200105)169:1<197::AID-MASY197>3.0.CO;2-2

Pendhari, S. S., Kant, T., & Desai, Y. M. (2008). Application of polymer composites in civil construction: A general review. *Composite Structures*, *84*(2), 114–124. https://doi.org/10.1016/j.compstruct.2007.06.007

Pérez-Maqueda, L. A., & Criado, J. M. (2000). The accuracy of Senum and Yang's approximations to the Arrhenius integral. *Journal of Thermal Analysis and Calorimetry*, *60*(3), 909–915.

Péron, M., Jacquemin, F., Casari, P., Orange, G., Bailleul, J.-L., & Boyard, N. (2017). Thermo-mechanical characterization of a thermoplastic composite and prediction of the residual stresses and lamina curvature during cooling. *AIP Conference Proceedings*, *1896*(1), 030015. https://doi.org/10.1063/1.5008002

PETHRICK, R. A. (2000). Bond Inspection in Composite Structures. In *Comprehensive Composite Materials* (pp. 359–392). https://doi.org/10.1016/b0-08-042993-9/00080-2

Petrescu, R. V. V., Aversa, R., Akash, B., Corchado, J., Berto, F., Apicella, A., & Petrescu, F. I. T. (2017). When Boeing is Dreaming – a Review. *Journal of Aircraft and Spacecraft Technology*, *1*(3), 149–161. https://doi.org/10.3844/jastsp.2017.149.161

Peyser, P., & Bascom, W. D. (1977). Kinetics of epoxy resin polymerization using differential scanning calorimetry. *Journal of Applied Polymer Science*, *21*(9), 2359–2373.

Pham, H. Q., & Marks, M. J. (2000). Epoxy resins. *Ullmann's Encyclopedia of Industrial Chemistry*, (Ed.). https://doi.org/10.1002/14356007.a09_547.pub2

Pintschovius, L. (1989). Determination of residual stresses by neutron diffraction. *Memoires et Etudes Scientifiques de La Revue de Metallurgie*, *86*(11), 723–728. https://doi.org/10.1016/s0026-0657(96)93572-9

Plueddemann, E. P. (2016). *Interfaces in Polymer Matrix Composites: Composite Materials, Vol. 6* (Vol. 6). Elsevier.

Prepreg Unidirectional Carbon Fiber Fabric. (n.d.). Retrieved March 5, 2020, from https://www.fibreglast.com/category/PrePreg_Fabrics

Prodromou, A. G., & Chen, J. (1997). On the relationship between shear angle and wrinkling of textile composite preforms. *Composites Part A: Applied Science and Manufacturing*, *28*(5), 491–503.

Prussak, R., Stefaniak, D., Kappel, E., Hühne, C., & Sinapius, M. (2019). Smart cure cycles for fiber metal laminates using embedded fiber Bragg grating sensors. *Composite Structures*, *213*, 252–260. https://doi.org/10.1016/j.compstruct.2019.01.079

Pühringer, J. F., Maier, C., & Zitzenbacher, G. *Determination of the mechanical properties at elevated temperature for a PP homopolymer applying tensile tests and DMA measurements*.

Reifsnider, K. L., Schulte, K., & Duke, J. C. (1983). Long-term fatigue behavior of composite materials. In *Long-term behavior of composites*, ed. T. O'Brien (West Conshohocken, PA: ASTM International, 136-159. https://doi.org/10.1520/STP31820S.

Rezaei, F., Yunus, R., Ibrahim, N. A., & Mahdi, E. S. (2008). Development of short-carbon-fiber-reinforced polypropylene composite for car bonnet. *Polymer - Plastics Technology and Engineering*, *47*(4), 351–357. https://doi.org/10.1080/03602550801897323

Roller, M. B. (1975). Characterization of the time-temperature-viscosity behavior of curing B-staged epoxy resin. *Polymer Engineering & Science*, *15*(6), 406–414.

Roşu, D., Caşcaval, C. N., Mustată, F., & Ciobanu, C. (2002). Cure kinetics of epoxy resins studied by non-isothermal DSC data. *Thermochimica Acta*, *383*(1–2), 119–127.

Sanchez, I. C. (2013). *Physics of Polymer Surfaces and Interfaces*. Butterworth-Heinemann.

Schajer, G. S. (2016). Residual Stresses: Measurement by Destructive Testing. *Reference Module in Materials Science and Materials Engineering*. https://doi.org/10.1016/b978-0-12-803581-8.03039-3

Schreier, H., Orteu, J. J., & Sutton, M. A. (2009). Image correlation for shape, motion and deformation measurements: Basic concepts, theory and applications. In *Image Correlation for Shape, Motion and Deformation Measurements: Basic Concepts,Theory and Applications*. Springer Science & Business Media. https://doi.org/10.1007/978-0-387-78747-3

Shabalin, L. P., Puzyretskii, E. A., Sidorov, I. N., & Girfanov, A. M. (2021). A Method for Calculating Process-Induced Stresses to Prevent Warping of Products of Composite Materials. *Journal of Machinery Manufacture and Reliability*, *50*(2), 133–142.

Shah, P. H., Halls, V. A., Zheng, J. Q., & Batra, R. C. (2018). Optimal cure cycle parameters for minimizing residual stresses in fiber-reinforced polymer composite laminates. *Journal of Composite Materials*, *52*(6), 773–792. https://doi.org/10.1177/0021998317714317

Smith, R. (2009). Composite defects and their detection. *Materials Science and Engineering*, *3*(1), 103–143.

Smith, R. A., Nelson, L. J., Mienczakowski, M. J., & Wilcox, P. D. (2016). Ultrasonic tracking of ply drops in composite laminates. *AIP Conference Proceedings*, *1706*. https://doi.org/10.1063/1.4940505

Soohyun, N., Dongyoung, L., Ilbeom, C., & Dai Gil, L. (2015). Smart cure cycle for reducing the thermal residual stress of a co-cured E-glass/carbon/epoxy composite structure for a vanadium redox flow battery. *Composite Structures*, *120*, 107–116.

Speriatu, L., Schulz, W., & Ifju, P. (2005). Test methods for determining temperature dependent material properties and residual stress modeling for laminated composites. *20th Technical Conference of the American Society for Composites 2005*, *2*, 1479–1495.

Sreekantamurthy, T., Hudson, T. B., Hou, T.-H., & Grimsley, B. W. (2016). Composite cure process modeling and simulations using COMPRO® and validation of residual strains using fiber optics sensors. *American Society for Composites: Thirty-First Technical Conference, Williamsburg, VA*.

Stacey, A., Webster, P. J., & Ziebeck, K. R. A. (1985). Measurement of residual stresses by neutron diffraction. *The Journal of Strain Analysis for Engineering Design*, *20*(2), 93–100. https://doi.org/10.1243/03093247V202093

Stretchlon 800 Bagging Film in stock | Fibre Glast. (n.d.). Retrieved March 5, 2020, from https://www.fibreglast.com/product/Stretchlon_800_Bagging_Film_1688/Vacuum_Bagging_Films_Peel_Ply_Tapes

Strong, A. B. (2008). *Fundamentals of Composites Manufacturing: Materials, Methods and Applications*. Society of Manufacturing Engineers.

Sunderland, P., Yu, W., & Månson, J. (2001). A thermoviscoelastic analysis of process-induced internal stresses in thermoplastic matrix composites. *Polymer Composites*, *22*(5), 579–592.

Sutcliffe, M. P. F., Lemanski, S. L., & Scott, A. E. (2012). Measurement of fibre waviness in industrial composite components. *Composites Science and Technology*, *72*(16), 2016–2023. https://doi.org/10.1016/j.compscitech.2012.09.001

Sutton, A. P. (1995). Interfaces in crystalline materials. *Monographs on the Physice and Chemistry of Materials*, 414–423.

Takeda, T. (2018). Micromechanics model for three-dimensional effective elastic properties of composite laminates with ply wrinkles. *Composite Structures*, *189*, 419–427. https://doi.org/10.1016/j.compstruct.2017.10.086

Tallinen, T., Ojajärvi, J., Åström, J. A., & Timonen, J. (2010). Scaling behavior in non-hookean compression of thin-walled structures. *Physical Review Letters*, *105*(6), 66102.

Tan, S. C., & Nuismer, R. J. (1989). A Theory for Progressive Matrix Cracking in Composite Laminates. *Journal of Composite Materials*, *23*(10), 1029–1047. https://doi.org/10.1177/002199838902301006

Tavakol, B., Roozbehjavan, P., Ahmed, A., Das, R., Joven, R., Koushyar, H., Rodriguez, A., & Minaie, B. (2013). Prediction of residual stresses and distortion in carbon fiber-epoxy composite parts due to curing process using finite element analysis. *Journal of Applied Polymer Science*, *128*(2), 941–950. https://doi.org/10.1002/app.38075

Thai, T. Q., Hansen, R. S., Smith, A. J., Lambros, J., & Berke, R. B. (2019). Importance of exposure time on DIC measurement uncertainty at extreme temperatures. *Experimental Techniques*, *43*(3), 261–271.

Toldy, A., Szolnoki, B., & Marosi, G. (2011). Flame retardancy of fibre-reinforced epoxy resin composites for aerospace applications. *Polymer Degradation and Stability*, *96*(3), 371–376. https://doi.org/10.1016/j.polymdegradstab.2010.03.021

Twigg, G., Poursartip, A., & Fernlund, G. (2004a). Tool–part interaction in composites processing. Part I: experimental investigation and analytical model. *Composites Part A: Applied Science and Manufacturing*, *35*(1), 121–133.

Twigg, G., Poursartip, A., & Fernlund, G. (2004b). Tool–part interaction in composites processing. Part II: numerical modelling. *Composites Part A: Applied Science and Manufacturing*, *35*(1), 135–141.

Umarfarooq, M. A., Gouda, P. S. S., Banapurmath, N. R., & Edacherian, A. (2019). Impact of process induced residual stresses on interlaminar fracture toughness in carbon epoxy composites. *Composites Part A: Applied Science and Manufacturing*, *127*, 105652.

Venkatesan, K., Ramanathan, K., Vijayanandh, R., Selvaraj, S., Kumar, G. R., & Kumar, M. S. (2020). Comparative structural analysis of advanced multi-layer composite materials. *Materials Today: Proceedings*, *27*, 2673–2687.

Vyazovkin, S. (1997). Advanced isoconversional method. *Journal of Thermal Analysis and Calorimetry*, *49*(3), 1493–1499.

Weber, T. A., Arent, J.-C., Steffens, L., Balvers, J. M., & Duhovic, M. (2017). Thermal optimization of composite autoclave molds using the shift factor approach for boundary condition estimation. *Journal of Composite Materials*, *51*(12), 1753–1767.

Weitsman, Y. (1979). Residual Thermal Stresses Due To Cool-Down of Epoxy-Resin Composites. *Journal of Applied Mechanics, Transactions ASME*, *46*(3), 563–567. https://doi.org/10.1115/1.3424606

White, S. R., & Hahn, H. T. (1993). Cure Cycle Optimization for the Reduction of Processing-Induced Residual Stresses in Composite Materials. *Journal of Composite Materials*, *27*(14), 1352–1378. https://doi.org/10.1177/002199839302701402

Willmott, G. R., & Radford, D. D. (2005). Taylor impact of glass rods. *Journal of Applied Physics*, *97*(9), 93522. https://doi.org/10.1063/1.1889249

Windhorst, T., & Blount, G. (1997). Carbon-carbon composites: a summary of recent developments and applications. *Materials & Design*, *18*(1), 11–15.

Wisnom, M. R., Gigliotti, M., Ersoy, N., Campbell, M., & Potter, K. D. (2006). Mechanisms generating residual stresses and distortion during manufacture of polymer-matrix composite structures. *Composites Part A: Applied Science and Manufacturing*, *37*(4), 522–529. https://doi.org/10.1016/j.compositesa.2005.05.019

Witik, R. A., Payet, J., Michaud, V., Ludwig, C., & Månson, J.-A. E. (2011). Assessing the life cycle costs and environmental performance of lightweight materials in automobile applications. *Composites Part A: Applied Science and Manufacturing*, *42*(11), 1694–1709.

Xiao, Y., Wang, W. X., Takao, Y., & Ishikawa, T. (2000). Effective friction coefficient of a laminate composite, and analysis of pin-loaded plates. *Journal of Composite Materials*, *34*(1), 69–87. https://doi.org/10.1106/V82B-A1BB-9PWR-MXTC

Yinnon, H., & Uhlmann, D. R. (1983). Applications of thermoanalytical techniques to the study of crystallization kinetics in glass-forming liquids, part I: theory. *Journal of Non-Crystalline Solids*, *54*(3), 253–275.

Yousefi, A., Lafleur, P. G., & Gauvin, R. (1997). Kinetic studies of thermoset cure reactions: a review. *Polymer Composites*, *18*(2), 157–168.

Zhu, B., Yu, T. X., & Tao, X. M. (2007). An experimental study of in-plane large shear deformation of woven fabric composite. *Composites Science and Technology*, *67*(2), 252–261.

Zhu, J., Wang, J., Ni, A., Guo, W., Li, X., & Wu, Y. (2018). A multi-parameter model for stiffness prediction of composite laminates with out-of-plane ply waviness. *Composite Structures*, *185*, 327–337. https://doi.org/10.1016/j.compstruct.2017.11.020

Zhu, J., Wu, W., Ouyang, J., Wang, J., & Ni, A. (2016). Influence of out-of-plane waviness on elastic properties of composite laminates. *Fuhe Cailiao Xuebao/Acta Materiae Compositae Sinica*, *33*(9), 1981–1988. https://doi.org/10.13801/j.cnki.fhclxb.20160102.001

PUBLICATIONS

Chava, S., & Namilae, S. (2021). Continuous evolution of processing induced residual stresses in composites: An in-situ approach. Composites Part A: Applied Science and Manufacturing, 145, 106368.

Chava, S., & Namilae, S. (2021). In situ investigation of the kinematics of ply interfaces during composite manufacturing. Journal of Manufacturing Science and Engineering, 143(2), 021006.

Chava, S., & Namilae, S. (2021). In-Situ Monitoring of the Manufacturing Process and Residual Stress Evolution in Thin-Ply Composites. In American Institute of Aeronautics and Astronautics (AIAA) SciTech 2021 Forum (p. 1776).

Chava, S., & Namilae, S. (2020). Evolution of Composite Defects During Manufacturing: Wrinkles & Delamination. Society for the Advancement of Material and Process Engineering (SAMPE) 2020 – North America, May 2020.

Chava, S., & Namilae, S. (2019). In-situ Characterization of Composite Ply-Movement and Manufacturing Defects. Society for the Advancement of Material and Process Engineering (SAMPE) 2019-Charlotte, NC, May 2019.

Chava, S., Namilae, S. & Al-Haik, M. (2021). Residual Stress Reduction during Composite Manufacturing through Cure Modification: In Situ Analysis. Journal of Composite Materials (Accepted).

Chava, S., Namilae, S., and Al-Haik, M. (2021). "In-Situ Experimental Evaluation of Residual Stresses in Composites during Autoclave Manufacturing" The Minerals, Metals & Materials (TMS) 2021 Annual Meeting & Exhibition, March 2021.

Jani, M., Chava, S., & Namilae, S. (2022). In-Situ Monitoring of Additive Manufacturing Using Digital Image Correlation. In American Institute of Aeronautics and Astronautics (AIAA) SciTech 2022 (In Review)

Motagi, S., Chava, S., & Namilae, S. (2019). In-Situ Measurement of Resin Shrinkage in Epoxy Composite. Society for the Advancement of Material and Process Engineering (SAMPE) 2019-Charlotte, NC, May 2019.

APPENDIX A – MATLAB Code for Residual Ply Stresses

```
%% CHAVA %%
% Modified CLT program to calculate Residual Ply Stresses
clear all close all clc
warning off
format short e

% Material Property Initialization
data = xlsread('Data090.xlsx'); % Importing temperature
dependent properties
ti = data(:,1); % Time
Te = data(:,2); % Temperature
EE1 = data(:,3); % E1 at T
EE2 = data(:,4); % E2 at T
ee = data(:,5:13); % Strains ex, ey & exy at T
ude = data(:,14:16); % Unidirectional Strain
v12 = .35; % Poisson's Ratio
G12 = 5e+9; % In-plane sheer modulus
plys = input('Enter the Number of plys you have: ');
jj=0;

for i = 1:plys
disp(' ');
disp(sprintf('Enter the fiber orientation of the #%d
ply',i))
theta(i) = input('');
end

for j=1:length(Te)
E1 = EE1(j); % Youngs Modulus in 0 deg (fiber direction)
E2 = EE2(j); % Youngs Modulus in 90 deg (transverse
direction)
for i = 1:plys
% All Q & S calculations are stored in a 3D array for
further use (QANDS.m)
[Q1,S,Qbar(:,:,i),Sbar(:,:,i),T(:,:,i)]=QandS(E1,E2,G12,v12
,theta(i));
for nsample = 1:3

%****************
% Experimental Liberated Strains
%****************

jj=jj+1;
e0 = ee(j,3*nsample-2:3*nsample);
```

```
strain(jj,:) = (T(:,:,i)*[e0]')'; % Strain after
multiplying with Transformation Matrix
residualstrain(jj,:) = strain(jj,:)-ude(j,:); % Residual
Strain from Liberated Strain
plystresses=Q1*residualstrain(jj,:)';
sigmax(nsample)=plystresses(1)*1/10^6;
sigmay(nsample) = plystresses(2)*1/10^6;
end
Mx(i,j) = mean(sigmax);
Lx(i,j) = min(sigmax)-Mx(i,j);
Ux(i,j) = max(sigmax)-Mx(i,j);
My(i,j) = mean(sigmay);
Ly(i,j) = min(sigmay)-My(i,j);
Uy(i,j) = max(sigmay)-My(i,j);
sx(i,j)=min(sx1);
end
end

%****************
% Plotting Cure Residual Stresses for Symmetric Layup
%****************

figure(1);
subplot(2,2,1)
ax1=subplot(2,2,1)
errorbar(ti,Mx(1,:),Lx(1,:),Ux(1,:),'k');
xlim([20 120]);
xticks(20:20:120);
ax1.XDir = 'reverse';
set(gca,'fontweight','bold')
title('Ply 0^o');
ylabel('\sigma_L (MPa)','FontWeight','Bold');
hold on
subplot(2,2,2)
ax2=subplot(2,2,2)
errorbar(ti,Mx(2,:),Lx(2,:),Ux(2,:),'k');
xlim([20 120]);
xticks(20:20:120);
ax2.XDir = 'reverse';
ylim([-30 400]);
set(gca,'fontweight','bold')
title('Ply 90^o');
hold on
set(gca,'ycolor','k')
subplot(2,2,3)
ax3=subplot(2,2,3)
errorbar(ti,My(1,:),Ly(1,:),Uy(1,:),'k');
```

```
xlim([20 120]);
xticks(20:20:120);
ax3.XDir = 'reverse';
ylim([0 40]);
set(gca,'fontweight','bold')
title('Ply 0^o');
ylabel('\sigma_T (MPa)','FontWeight','Bold');
hold on
subplot(2,2,4)
ax4=subplot(2,2,4)
errorbar(ti,My(2,:),Ly(2,:),Uy(2,:),'k');
xlim([20 120]);
xticks(20:20:120);
ax4.XDir = 'reverse';
set(gca,'fontweight','bold')
title('Ply 90^o');
set(gca,'ycolor','k')
han=axes(figure(1),'visible','off');
han.Title.Visible='on';
han.XLabel.Visible='on';
han.YLabel.Visible='on';
xlabel(han,'Time (min)','FontWeight','Bold');
xlabel(han,'Temperature (^oC)','FontWeight','Bold');
set(0, 'DefaultFigureColor', 'white');

%****************
% Plotting Cure Residual Stresses for Asymmetric Layup
%****************

figure(1);
subplot(2,4,1)
errorbar(ti,Mx(1,:),Lx(1,:),Ux(1,:),'k');
ylim([0 400]);
set(gca,'fontweight','bold')
title('Ply 0^o');
ylabel('\sigma_L (MPa)','FontWeight','Bold');
hold on
subplot(2,4,2)
errorbar(ti,Mx(2,:),Lx(2,:),Ux(2,:),'k');
ylim([0 400]);
set(gca,'fontweight','bold')
title('Ply 30^o');
hold on
subplot(2,4,3)
errorbar(ti,Mx(3,:),Lx(3,:),Ux(3,:),'k');
ylim([0 400]);
set(gca,'fontweight','bold')
```

```
title('Ply 45^o');
hold on
subplot(2,4,4)
errorbar(ti,Mx(4,:),Lx(4,:),Ux(4,:),'k');
ylim([-30 400]);
set(gca,'fontweight','bold')
title('Ply 90^o');
set(gca,'ycolor','k')
subplot(2,4,5)
errorbar(ti,My(1,:),Ly(1,:),Uy(1,:),'k');
set(gca,'fontweight','bold')
title('Ply 0^o');
ylabel('\sigma_T (MPa)','FontWeight','Bold');
hold on
subplot(2,4,6)
errorbar(ti,My(2,:),Ly(2,:),Uy(2,:),'k');
ylim([0 40]);
set(gca,'fontweight','bold')
title('Ply 30^o');
hold on
subplot(2,4,7)
errorbar(ti,My(3,:),Ly(3,:),Uy(3,:),'k');
set(gca,'fontweight','bold')
title('Ply 45^o');
hold on
subplot(2,4,8)
errorbar(ti,My(4,:),Ly(4,:),Uy(4,:),'k');
ylim([0 40]);
set(gca,'fontweight','bold')
title('Ply 90^o');
set(gca,'ycolor','k')
han=axes(figure(1),'visible','off');
han.Title.Visible='on';
han.XLabel.Visible='on';
han.YLabel.Visible='on';
xlabel(han,'Time (min)','FontWeight','Bold');
% ylabel(han,'\sigma_T (MPa)','FontWeight','Bold');
set(0, 'DefaultFigureColor', 'white');
```

APPENDIX B – MATLAB Code for Residual Laminate Stresses

```
%% CHAVA %%
% CLT program for calculating laminate stresses
clear all close all clc
warning off
format short e

% Material Property Initialization
data = xlsread('Data00.xlsx'); % Importing temperature
dependent properties
ti = data(:,1); % Time
Te = data(:,2); % Temperature
EE1 = data(:,3); % E1 at T
EE2 = data(:,4); % E2 at T
ee = data(:,5:13); % Strains ex, ey & exy at T
ude = data(:,14:16); % Unidirectional Strain
v12 = .35; % Poisson's Ratio
G12 = 5e+9; % In-plane sheer modulus
t = 0.00025;
plys = input('Enter the Number of plys you have: ');
jj=0;

for i = 1:plys
disp(' ');
disp(sprintf('Enter the fiber orientation of the #%d
ply',i))
theta(i) = input('');
end

for j=1:length(Te);
E1 = EE1(j); % Youngs Modulus in 0 deg (fiber direction)
E2 = EE2(j); % Youngs Modulus in 90 deg (transverse
direction)
[ABD]=abdnew1(E1,E2,G12,v12,theta,t,plys);

for nsample = 1:3
%****************
% Experimental Strains
%****************
jj=jj+1;
e = ee(j,3*nsample-2:3*nsample);
strain(jj,:) = e;
NM_Combined = ABD*[strain(jj,:) 0 0 0]';
Nx(nsample) = NM_Combined(1)*1/10^3;
Ny(nsample) = NM_Combined(2)*1/10^3;
Nxy(nsample) = NM_Combined(3)*1/10^3;
```

```
end
Mx(j) = mean(Nx);
Lx(j) = min(Nx)-Mx(j);
Ux(j) = max(Nx)-Mx(j);
My(j) = mean(Ny);
Ly(j) = min(Ny)-My(j);
Uy(j) = max(Ny)-My(j);
Mxy(j) = mean(Nxy);
Lxy(j) = min(Nxy)-Mxy(j);
Uxy(j) = max(Nxy)-Mxy(j);
end

%****************
% Plotting Cure Residual Stresses
%****************

figure(1);
subplot(2,3,1)
errorbar(ti,Mx(1,:),Lx(1,:),Ux(1,:),'k');
xlim([20 100]);
ylim([0 300]);
yticks(0:100:300);
set(gca,'fontweight','bold')
title('[0/0]_s');
hold on
han=axes(figure(1),'visible','off');
han.Title.Visible='on';
han.XLabel.Visible='on';
han.YLabel.Visible='on';
xlabel(han,'Time (min)','FontWeight','Bold');
ylabel(han, 'N_x_x (KN/m)','FontWeight','Bold');
set(0, 'DefaultFigureColor', 'white');

figure(2);
subplot(2,3,1)
errorbar(ti,My(1,:),Ly(1,:),Uy(1,:),'k');
xlim([20 100]);
ylim([0 200]);
yticks(0:50:200);
set(gca,'fontweight','bold')
title('[0/0]_s');
hold on
set(gca,'ycolor','k')
han=axes(figure(2),'visible','off');
han.Title.Visible='on';
han.XLabel.Visible='on';
han.YLabel.Visible='on';
```

```
xlabel(han,'Time (min)','FontWeight','Bold');
ylabel(han, 'N_y_y (KN/m)','FontWeight','Bold');
set(0, 'DefaultFigureColor', 'white');

figure(3);
subplot(2,3,1)
errorbar(ti,Mxy(1,:),Lxy(1,:),Uxy(1,:),'k');
xlim([20 100]);
ylim([0 80]);
yticks(0:20:80);
set(gca,'fontweight','bold')
title('[0/0]_s');
han=axes(figure(3),'visible','off');
han.Title.Visible='on';
han.XLabel.Visible='on';
han.YLabel.Visible='on';
xlabel(han,'Time (min)','FontWeight','Bold');
ylabel(han, 'N_x_y (KN/m)','FontWeight','Bold');
set(0, 'DefaultFigureColor', 'white');
```

APPENDIX C – MATLAB Code for Residual Laminate Moments

```
%% CHAVA %%
% CLT program for calculating laminate moments
clear all close all clc
warning off
format short e

% Material Property Initialization
data = xlsread('Data0304590.xlsx'); % Importing temperature
dependent
properties
ti = data(:,1); % Time
Te = data(:,2); % Temperature
EE1 = data(:,3); % E1 at T
EE2 = data(:,4); % E2 at T
ee = data(:,5:13); % Strains ex, ey & exy at T
% ude = data(:,14:16); % Unidirectional Strain
v12 = .35; % Poisson's Ratio
G12 = 5e+9; % In-plane sheer modulus
t = 0.00025;
plys = input('Enter the Number of plys you have: ');
jj=0;

for i = 1:plys
disp(' ');
disp(sprintf('Enter the fiber orientation of the #%d
ply',i))
theta(i) = input('');
end

for j=1:length(Te);
E1 = EE1(j); % Youngs Modulus in 0 deg (fiber direction)
E2 = EE2(j); % Youngs Modulus in 90 deg (transverse
direction)
[ABD]=abdnew1(E1,E2,G12,v12,theta,t,plys);
for nsample = 1:3

%****************
% Experimental Strains
%****************

jj=jj+1;
e = ee(j,3*nsample-2:3*nsample);
strain(jj,:) = e;
NM_Combined = ABD*[strain(jj,:) 0 0 0]';
Nx(nsample) = NM_Combined(4);
```

```
Ny(nsample) = NM_Combined(5);
Nxy(nsample) = NM_Combined(6);
end
Mx(j) = mean(Nx);
Lx(j) = min(Nx)-Mx(j);
Ux(j) = max(Nx)-Mx(j);
My(j) = mean(Ny);
Ly(j) = min(Ny)-My(j);
Uy(j) = max(Ny)-My(j);
Mxy(j) = mean(Nxy);
Lxy(j) = min(Nxy)-Mxy(j);
Uxy(j) = max(Nxy)-Mxy(j);
end

%****************
% Plotting Cure Residual Stresses
%****************

figure(1);
subplot(2,3,1)
errorbar(ti,Mx(1,:),Lx(1,:),Ux(1,:),'k');
xlim([20 100]);
ylim([0 25]);
yticks(0:5:25);
set(gca,'fontweight','bold')
title('[0/0]_s');
hold on
han=axes(figure(1),'visible','off');
han.Title.Visible='on';
han.XLabel.Visible='on';
han.YLabel.Visible='on';
xlabel(han,'Time (min)','FontWeight','Bold');
ylabel(han, 'M_x_x (N-m/m)','FontWeight','Bold');
set(0, 'DefaultFigureColor', 'white');

figure(2);
subplot(2,3,1)
errorbar(ti,My(1,:),Ly(1,:),Uy(1,:),'k');
xlim([20 100]);
ylim([-20 10]);
yticks(-20:10:10);
set(gca,'fontweight','bold')
title('[0/0]_s');
hold on
set(gca,'ycolor','k')
han=axes(figure(2),'visible','off');
han.Title.Visible='on';
```

```
han.XLabel.Visible='on';
han.YLabel.Visible='on';
xlabel(han,'Time (min)','FontWeight','Bold');
ylabel(han, 'M_y_y (N-m/m)','FontWeight','Bold');
set(0, 'DefaultFigureColor', 'white');

figure(3);
subplot(2,3,1)
errorbar(ti,Mxy(1,:),Lxy(1,:),Uxy(1,:),'k');
xlim([20 100]);
ylim([-5 20]);
yticks(-5:5:20);
set(gca,'fontweight','bold')
title('[0/0]_s');
han=axes(figure(3),'visible','off');
han.Title.Visible='on';
han.XLabel.Visible='on';
han.YLabel.Visible='on';
xlabel(han,'Time (min)','FontWeight','Bold');
ylabel(han, 'M_x_y (N-m/m)','FontWeight','Bold');
set(0, 'DefaultFigureColor', 'white');
```